Uncertainty Quantification and Sensitivity Analysis of Solid Fuel Combustion

Unsicherheitsquantifizierung und Sensitivitätsanalyse der Verbrennung fester Brennstoffe

Von der Fakultät für Maschinenwesen der Rheinisch-Westfälischen Technischen Hochschule Aachen zur Erlangung des akademischen Grades eines Doktors der Ingenieurwissenschaften genehmigte Dissertation

vorgelegt von

Ahmed Ramadan Abdelfatah Hassan

Berichter/in: Univ.-Prof. Dr.-Ing. Reinhold Kneer

Diriger des Recherches Taraneh Sayadi, PhD

Tag der mündlichen Prüfung: 18. September 2023

Diese Dissertation ist auf den Internetseiten der Universitätsbibliothek online verfügbar.

Zusammenfassung

Die Simulation der instationären Verbrennung von Festbrennstoffpartikeln besteht aus dem Zusammenspiel mehrerer komplexer Phänomene wie zum Beispiel Chemie und Turbulenz. Um solche Wechselwirkungen zu erfassen, werden Modelle mit unterschiedlicher Genauigkeit verwendet. Daher ist es wichtig, ihre Unsicherheiten zu quantifizieren und die Sensitivitäten der verschiedenen Größen in Bezug auf diese Modellparameter zu analysieren. Als Ausgangspunkt für diese Studie wird der stationäre Verbrennungsprozess eines einzelnen Feststoffpartikels betrachtet. Aufgrund der großen Anzahl von Parametern, die in solchen Simulationen vorkommen, ist ein reiner Vorwärtsansatz für die Sensitivitätsanalyse nicht durchführbar. Daher wird die Verwendung von adjungierten Algorithmen vorgeschlagen, um die zugrunde liegenden Sensitivitäten und Unsicherheiten zu identifizieren und zu quantifizieren. Es werden sowohl diskrete als auch kontinuierliche adjungierte Algorithmen betrachtet und mit konventionellen Ansätzen, wie z.B. Finite-Differenzen, verglichen. Sensitivitäten, die Luft- und Oxyatmosphären beschreiben, werden in Bezug auf die relevanten Verbrennungsparameter für zwei verschiedene Zusammensetzungen berechnet. Um die Auswirkungen von Instabilitäten und Nichtlinearitäten auf die extrahierten Sensitivitäten zu berücksichtigen, wird ein halbdiskreter adjungierter Ansatz auf die instationäre Verbrennung von Holzpartikeln angewandt. Zur Untersuchung des Gasphasenverbrennungsmodells und zur Einbindung verschiedener Phänomene, wie die Entgasung, wurden die Unsicherheiten von Gasphasenkinetikmodellen in einem nulldimensionalen isobaren Reaktor untersucht. Die Active Subspace-Methode, ergänzt durch die adjungierte Technik (AASM), erwies sich als ein effizientes Werkzeug für diesen Zweck. Die Vorhersagen von AASM wurden mit einer kostengünstigeren Methode, der linearen Approximation mit dem adjungierten Modell (LAAM), berechnet. Schließlich wurde die Entwicklung der Sensitivitäten für eine einzelne instationäre achsensymmetrische Partikelkonfiguration berechnet, einschließlich verschiedener Phänomene wie Entgasung, Verbrennung von Holzkohle und einem detaillierten Methan-Mechanismus für Gasphasenreaktionen. AASM wurde auch zur Quantifizierung der Unsicherheiten des Modells genutzt.

Abstract

Simulations of unsteady solid fuel particle combustion consist of the interaction of multiple complex phenomena, such as chemistry, turbulence, etc. In order to capture such interactions, models with variable fidelity are used. It is therefore essential to quantify the uncertainty and analyze the sensitivities of different quantities of interest with respect to these model parameters. The steady combustion process of a single solid particle is considered as a starting point for this study. The large number of parameters present in such simulations makes a purely forward approach to sensitivity analysis infeasible. Therefore, the use of adjoint-based algorithms to identify and quantify the underlying sensitivities and uncertainties is proposed. Both discrete and continuous adjoints are considered and compared to conventional approaches, such as finite differences. Various quantities of interest are considered, and sensitivities with respect to the relevant combustion parameters are reported for two different free-stream compositions, describing air and oxy atmospheres. To address the effect of unsteadiness and nonlinearity on the extracted sensitivities, a semi-discrete adjoint approach is then applied to unsteady char particle combustion. To examine the gas phase combustion model and to incorporate various phenomena such as devolatilization, the uncertainty quantification of gas phase kinetic models was studied in a zero-dimensional isobaric reactor. The active subspace method augmented with the adjoint technique (AASM) was found to be an efficient tool for this purpose. The predictions of AASM were compared to a cheaper method, which is a linear approximation using the adjoint model (LAAM). Finally, the sensitivities' evolution was calculated as a function of time for a single unsteady axisymmetric particle configuration, including different phenomena such as devolatilization, char combustion, and a detailed methane mechanism for gas phase reactions. AASM was also used to quantify the uncertainties present in the model.

Publication List

This thesis is mainly based on the following publications:

- A. Hassan, T. Sayadi, V. Le Chenadec, H. Pitsch and A. Attili, Adjoint-based sensitivity analysis of steady char burn out. Com. Theo. Modeling, Volume 25, Issue 1, 2020, Pages 96- 120.
- A. Hassan, T. Sayadi, M. Schiemann, and V. Scherer, Adjoint-based sensitivity analysis of char combustion surface reaction kinetics, Fuel, Volume 287, 2021, Article number 119503.
- A. Hassan, T. Sayadi, V. Le Chenadec, and A. Attili, Sensitivity analysis of an unsteady char particle combustion, Fuel, Volume 287, 2021, Article number 119738.
- A. Hassan, M. Sabry, V. Le Chenadec, and T. Sayadi, Uncertainty quantification of kinetic models using adjoint-driven active subspace algorithms. Proceedings of the Combustion Institute, Volume 39, Issue 4, 2023,Pages 5209- 5218.
- A. Hassan, L. Schumacher, M. Sabry, V. Le Chenadec and T. Sayadi, Uncertainty quantification and sensitivity analysis of single axisymmetric particle combustion. Combustion and Flame, Volume 262, April 2024, Article number 113365.

Contents

Zusammenfassung iii

Abstract v

Publication List vii

Contents viii

Nomenclature xi

1. Introduction 1

2. Sensitivity analysis of steady char combustion 10
- 2.1. Governing equations . . . 11
  - 2.1.1. Boundary Conditions . . . 13
- 2.2. Two-point boundary value problem and adjoint-based gradient computation . . . 14
  - 2.2.1. Two-point boundary value problem . . . 15
  - 2.2.2. Continuous adjoint formulation . . . 16
  - 2.2.3. Discrete adjoint formulation . . . 17
- 2.3. Validation . . . 17
  - 2.3.1. Primal problem . . . 17
  - 2.3.2. Extracted sensitivities . . . 18
- 2.4. Results . . . 21
- 2.5. Summary and Conclusions . . . 30

3. Adjoint-based sensitivity analysis of char combustion surface reaction kinetics 33
- 3.1. Governing equations . . . 34
- 3.2. Operating conditions and sensitivity analysis . . . 35
- 3.3. Summary and Conclusions . . . 43

4. Sensitivity analysis of an unsteady char particle combustion 44
4.1. Governing equations . . . 45
4.1.1. Boundary conditions . . . 46
4.1.2. Chemical models . . . 48
4.2. Gradient computation . . . 49
4.2.1. Forward sensitivity . . . 50
4.2.2. Discrete adjoint . . . 52
4.3. Discretization and numerical solution . . . 54
4.4. Results and Validation . . . 55
4.4.1. Forward (primal) problem . . . 56
4.4.2. Sensitivities of unsteady char combustion . . . 58
4.5. Summary and Conclusions . . . 64

5. Uncertainty quantification of kinetic models using adjoint-driven active subspace algorithms 66
5.1. Methodology . . . 67
5.1.1. Adjoint Method . . . 68
5.1.2. Active Subspace Method (ASM) . . . 70
5.1.3. Linear Approximation using the Adjoint Method (LAAM) 71
5.2. Results . . . 72
5.2.1. One-dimensional subspace . . . 73
5.2.2. Multi-dimensional subspace . . . 77
5.2.3. Initial conditions effect . . . 79
5.3. Summary and Conclusions . . . 81

6. Uncertainty quantification and sensitivity analysis of single axisymmetric particle combustion 83
6.1. Governing equations . . . 84
6.1.1. Chemical and thermodynamic models . . . 84
6.2. Results . . . 85
6.2.1. Forward (primal) problem . . . 86
6.2.2. Extracted sensitivities . . . 88
6.2.3. Extracted uncertainties . . . 95
6.3. Summary and Conclusions . . . 100

7. Concluding remarks 102

Appendices 107

A. Adjoint derivation for boundary value problem **109**
A.1. Derivation of the adjoint equation and gradient formula for two-point boundary value problem 110
A.1.1. Forward sensitivity of the primal problem 110
A.1.2. Adjoint of the primal problem 110
A.1.3. Forward sensitivity of the adjoint problem 112
A.1.4. Integration bounds 113
A.2. Linearized boundary conditions 114
A.2.1. Forward problem 114
A.2.2. Adjoint problem 115

Nomenclature

Group A

α	Coordinates varialbe
β_c	temperature exponent of char oxidation reaction
β_v	Volatile temperature exponents
$\boldsymbol{\Lambda}$	Eigen values
χ	Space coordinates
$\dot{M}$	Particle burning rate
$\dot{m}_\alpha^0$	Mass flux per unit surface area
$\dot{M}_w$	Mass flux at the surface of the particle
$\dot{m}_c$	Char reaction rate
$\dot{T}$	Temperature gradient
ϵ	Mean error
γ	ratio between surface reactions Damköhler numbers
λ	coefficient of heat conduction
λ_1	Wave length
λ_2	Wave length
λ_g	coefficient of gas mixture heat conduction
λ_s	coefficient of solid particle heat conduction
λ_w	Thermal conductivity at the particle surfacae
$\mathbf{C}$	Covariance matrix
$\mathcal{L}$	Linear operator

$\mathcal{N}$	Natural distribution
$\mathcal{W}_i$	molecular weight of species i
Le	Lewis number
Y_i	mass fraction of species i
μ	Mean value of the PDF
ν_i'	stoichiometric coefficients of the reactant
ν_i''	stoichiometric coefficients of the product
ω	homogeneous reaction rate
ω_i	production/consumption rate of species i
ω_T	chemical source term in energy equation
$\overline{\alpha}$	molecular weight ration between O_2 and CO_2
Φ^a	Vector of algebraic variables
Φ^d	Vector of differential variables
ψ	Oxegen stoichiometric ratio
ρ	density
ρ_0	non-dimensional gas mixture density
σ	PDF variance
τ	Time coordinates
$\mathbf{P}$	Vector of model parameters
$\mathbf{V}_i$	diffusion velocity for species i
$\mathbf{W}$	Eigen vectors
θ	non-dimensional Activation energy for gas phase reaction
$\tilde{R}$	specific gas constant based on an average molecular weight
φ	non dimensional temperature and species variables set

ζ_i	Volatile release constant
a	Particle radius
A_c	pre-exponential factor of char oxidation reaction
A_j^0	Mean value of pre-exponential factor
A_s	Pre-exponential factor of surface reaction
A_v	Volatile pre-exponential factor
b_j	Temperature exponent of reaction j
C_α	Unit surface area
C_c	particle heat capacity
C_p	specific heat for gas mixture at constant P
C_v	The average heat capacity of gas mixture at constant volume
D	diffusion coefficient for species mixture
D_i	diffusion coefficient for species i
Da^g	Gas phase Damköhler number
Da_i^s	Damköhler number of heterogeneous reaction i
E	Activation energy for gas phase reaction
E_a^s	Activation energy of surface reaction
E_j	Activation energy of reaction j
E_v	Volatile activation energy
g	Local objective function in space or time
G^s	Objective function in integral form
h_i^0	Enthalpy of formation of species i
h_v	Heat release of volatiles
$h_{c,i}$	Enthalpy of surface reaction i

k_v	Volatile release rate
k	homogeneous reaction rate
M	Number of samples
M_p	particle mass
N_r	number of reactions
P^*	Non-dimensional pressure
P^s	species partial pressure
p_0	non-dimensional gas mixture pressure
Q	Heat of the homogenous reaction per unit mass of CO_2
R	universal gas constant
r	Radial coordinates
r_0	Particle initial radius
r_∞	Domain size
S	Non-dimensional sensitivity
T	gas phase temperature
t	Time
T^∞	Free stream temperature
T_f	flame temperature
T_p	Particle temperature
T_p^0	Initial particle temperature
t_r	Reaction characteristics time
T_S	Shifted gas phase temperature profile
T_s	Non-dimensional particle surface temperature
t_s	Ignition shifting time

T_s^g	Gas temperature at the particle surface
u	Flow velocity
UF_j	Uncertainty factor of reaction j
X_i	Molecular weights ratio for char direct oxidation reaction
Y_i^∞	Free stream mas fraction of species i
Z_i	Molecular weights ratio for char indirect oxidation reaction
$T^{\infty *}$	Free stream non-dimensional temperature
$T^{\infty *}$	Particle temperature
$\mathbf{v}$	mass-averaged velocity
AASM	Adjoint Active Subspace Method
AD	Algorithmic (or Automatic) Differentiation
ANN	Artificial Neural Networks
ASM	Active Subspace Method
CBK	Coal burnout kinetic model
CFD	Computational Fluid Dynamics
CSD	Complex Step Differentiation
DAE	Differential Algebraic Equation
DME	dimethyl ether
HDMR	High Dimensional Model Representation
IDT	Ignition Delay Time
IEA	International Energy Agency
LAAM	Linear Adjoint Approximation Method
LFS	Laminar Flame Speed
MC	Monte Carlo

ODE	Ordinary Differential Equation
P	Pressure
PCE	Polynomial Chaos Expansion
PDF	Probability Density Function
QoI	Quantity of Interest
RANS	Reynolds-averaged Navier–Stokes
SCOT	Stereoscopic Camera for Optical Thermography
UQ	Uncertainty Quantification

1

Introduction

Climate change resulting from global warming has been a major topic of concern over the past decade, posing a significant threat to life on earth. High levels of carbon dioxide (CO_2) emissions contribute significantly to this issue, particularly those resulting from the use of fossil fuels in daily activities such as transportation and power generation. Solid fuels like coal and biomass are particularly problematic, as they are still widely used in power plants to generate energy. Furthermore, energy demands are increasing on a regular basis, as shown in Figure 1.1. The International Energy Agency (IEA) predicts that energy demands will reach $17.723 Mt_{oe}$ in 2040, with an increase of $3.409 Mt_{oe}$ compared to 2018. Despite efforts to reduce carbon emissions, coal still has a significant share in energy sources, although introducing biomass as better replacement. However, this will lead to an increase in carbon dioxide (CO_2) emissions, which could make it difficult to achieve global targets for reducing CO_2 emissions. As a result, it is crucial to prioritize the use of carbon capture and storage (CCS) technology in order to reduce the amount of CO_2 released into the atmosphere. The application of oxy-fuel combustion techniques is one such approach, in which the atmosphere is changed to a mixture of O_2 and CO_2 instead of ambient air during the combustion process, allowing for more efficient isolation of CO_2 from the furnace flue. To achieve optimal combustion conditions, pure oxygen must be mixed with recycled CO_2 to raise the temperature of the mixture. To study this phenomenon on an experimental scale, Figure 1.2 shows an example of a burner with optical

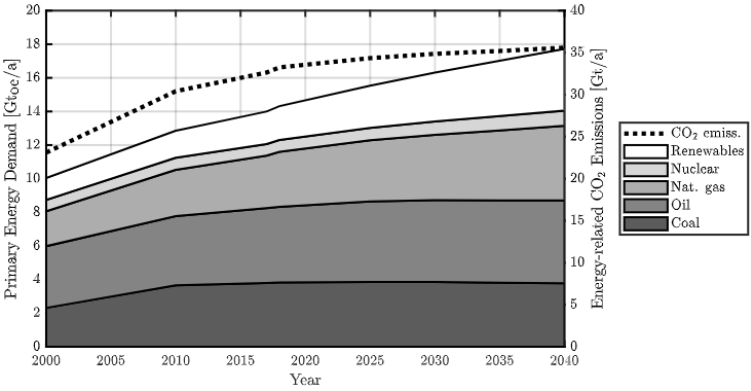


Figure 1.1.: International Energy Agency predictions for global primary energy demand and energy-related CO_2 emissions in the "stated policies" scenario [1].

access. This burner configuration provides a wide range of data that is used to model the combustion process. However, the operating point of solid fuel furnaces with this new oxygen-CO_2 mixture differs from that of traditional air-based furnaces, which are normally diluted with N_2, due to the different thermal, diffusion, and reactive properties of the two mixtures.

Recent advances in computational fluid dynamics (CFD), have made it a strong tool for predicting such flows and which together with the experiments can help design and optimise the overall combustion process. As far as solid fuel particles (coal/biomass) are concerned, combustion starts with the devolatilisation process, where partially oxidised smaller hydrocarbons and tars are released from the fuel particles leaving a char residue behind. Typically, devolatilisation occurs on a much faster time scale than the char burnout. As a result, it is common practice to analyse char combustion and devolatization processes individually, which for coal particles with relatively small volatile matter is an acceptable assumption. Nevertheless, for accurate predictions, devolatilisation, char combustion, heat transfer, and gas combustion, are commonly modeled in the simulations. Figure 1.3 shows a simulation of a jet of reactive particles performed by Farmand *et al* [3]. This is a common configuration for studying solid fuel combustion, especially to analyze the effect of particle interaction in different atmospheres and Reynolds numbers on combustion processes. This configuration only considers point particles without char combustion. To investigate sophisticated models, particle resolved simulations with different levels of fidelity are used, such as those in [4, 5].

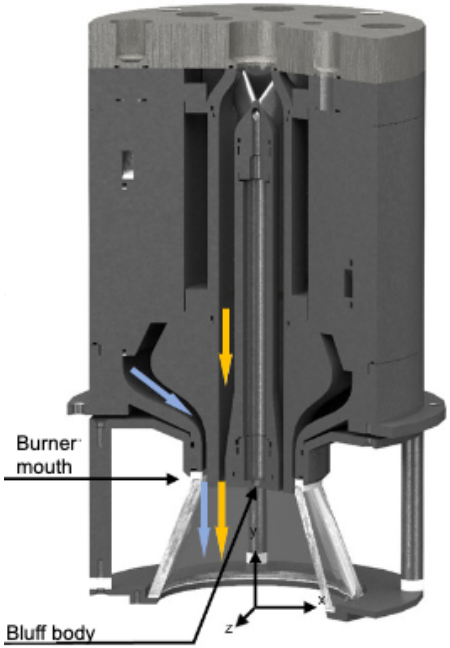


Figure 1.2.: A burner with an optically accessible quarl is being used for research on oxy-fuel combustion at Technische Universität Darmstadt [2].

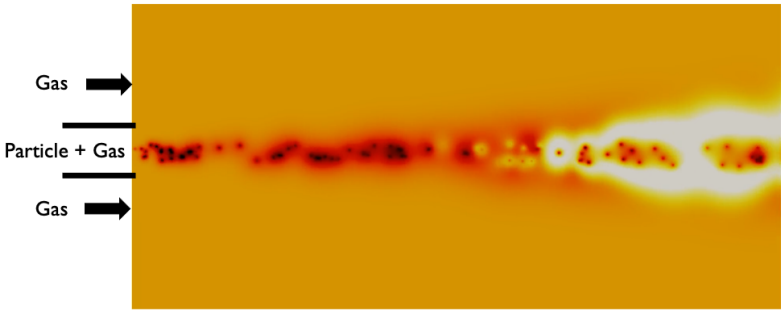


Figure 1.3.: Simulation of reactive laminar jet of particles [3].

Regardless of their fidelity, all existing models rely on many parameters in order to approximate the physical solution. These parameters are normally determined by experiments or small-scale simulations and contain a certain level of uncertainty. Therefore, it is of great importance to determine the sensitivity of the output (final solution or quantity of interest) to the existing parameters in the model. The extracted sensitivities (uncertainties) can later be used to build models consistent with the experimental data, as is done in a study by Lavarone *et al.* [6], where Bound-to-Bound Data Collaboration is used to derive a reduced char combustion model in both conventional and oxy-conditions. In practice, most of the sensitivity information is extracted in zero-dimensional or one-dimensional settings, focusing solely on the kinetics, and therefore ignoring the effect of the underlying multi-dimensional flow [7–9]. This is usually due to the fact that extracting the Jacobian (gradient) of the full system, including the coupled hydrodynamic and reactive equations, using conventional approaches, becomes very expensive and in many real-scale applications infeasible. Common methods in extracting the gradient information are analytical or use finite differences. As far as the analytical determination of the gradient is concerned, the subtleties associated with the numerical approach, such as the meshing process, discretisation, and the complexity of the governing equations, make extracting the analytical gradient expression far from straightforward. In the case of finite differences, on the other hand, the numerous parameters involved in modelling make this approach prohibitively expensive for large problems and also overwhelmed by numerical noise.

Adjoint-based methodologies allow the determination of the gradient at a cost comparable to a single function evaluation, regardless of the number of parameters, and are, therefore, a suitable alternative [10]. Traditionally, adjoint equations are derived from the continuous equations by applying a variational principle to the unconstrained optimization problem and setting the first variations with respect to all independent variables to zero. This results in governing equations for the direct (primal) and for the adjoint (dual) variables, together with appropriate boundary and initial conditions as well as optimality conditions, which subsequently have to be discretized and solved [11–13]. This provides gradient or sensitivity information about an optimisation problem.

The use of adjoint methods for design and optimisation has been an active area of research, which started with the pioneering work of Pironneau [14], with applications in fluid mechanics, and later in aeronautical shape optimisation by Jameson and co-workers [15–17]. Ever since these ground-breaking studies,

adjoint-based methods have been widely used in fluid mechanics, especially in the field of acoustics and thermo-acoustics [18, 19]. These areas provide a suitable application for adjoint-based methods, which are inherently linear, since they too are dominated by linear dynamics. Recently, nonlinear problems have also been tackled, within the context of optimal control of separation on a realistic high-lift airfoil or wing, enhancement of mixing efficiency, and minimal turbulence seeds, to name a few [20–22]. In the case of reactive flows, adjoint-based methods have also been employed for adaptive mesh refinement in steady-state Reynolds Averaged Navier–Stokes (RANS) simulations [23]. As far as detailed simulations are concerned, Braman *et al.* [24] have investigated the applicability of the adjoint-based techniques in one- and two-dimensional laminar flow configurations, where the hydrodynamics are decoupled from the species transport equations. In a recent work, Lemke *et al.* [25] have also explored the applicability of such techniques, in the zero-dimensional case of a homogeneous constant volume reactor, to study the sensitivity of the ignition delay time with respect to the parameters appearing in the combustion model. Adjoint-based methods have also been applied in the linear limit in various studies [26–28], using simplified combustion models.

Although these recent efforts show great promise in integrating adjoint-based methodologies in combustion technology for the purpose of sensitivity analysis and control, there still remain many open questions, regarding non-conventional boundary conditions (such as in the presence of evaporation or surface reactions), on the extraction and performance of the adjoint equations. Therefore, the two main objectives of chapter 2 are (i) to extract a general formulation for the adjoint problem, applied to fully coupled detailed simulations of steady char particle burnout, in the nonlinear limit, for the purpose of sensitivity analysis with respect to the existing model variables, using a flexible approach, which is easily extendable to higher dimensions; and (ii) to compare continuous and discrete adjoint formulations in order to investigate the most advantageous strategy for gradient extraction, as far as reactive flows with non-trivial boundary conditions, are concerned. These goals are pursued with a model proposed by Matalon [29], allowing the extraction of the exact solution for the primal and adjoint problems, and facilitating the assessment of continuous versus discrete adjoints. This chapter 2, therefore, is to be considered as the first step of developing an adjoint-based framework, that will be extended to cases with unsteady dynamics, including detailed kinetic mechanism, and a subject of the rest of this study in chapters 3,4,5, and 6.

The sensitivity analysis of various QoI carried out in chapter 2 emphasized the critical role of particle temperature as the most dominant parameter affecting most of the predictions. Furthermore, previous studies have demonstrated the importance of extracting particle temperature and size data, in order to extract the desired kinetic models, outperforming more common approaches relying on bulk measurements. In chapter 3, therefore, I rely on a surface model, extracted using particle temperature, in order to capture surface reactions of char particle combustion [30]. In this approach, particle temperature and size data are gathered, and combined with other experimental information, to produce the best fit parameter of the chosen char combustion model. Since heat and mass transfer is described reasonably well with established models, the kinetics parameters of the surface reaction mechanism are those fitted through gathered experimental data. Adjoint-based methods are then employed to extract the sensitivity of the described surface reaction model, with respect to various quantities of interest, to provide a detailed assessment of the existing sensitivities in the model parameters.

Although chapters 2 and 3 demonstrate flexible methods to extract sensitivities using adjoint approaches for non-conventional boundary conditions that exist due to surface reactions in char combustion, following concerns still need to be addressed:

- The influence of variable particle temperature instead of constant surface temperature on the extracted sensitivities.
- The effect of nonlinearities and unsteadiness (common place in realistic reactive configurations) on the extracted sensitivities.

The goal of chapter 4 is to answer these concerns by simulating an unsteady char particle combustion with variable particle temperature (resulting in a Robin-type boundary condition for the particle temperature), assuming thermal equilibrium between the particle and the adjacent gas layer. As the dimensionality and complexity of the governing equations increase, the fully continuous adjoint strategy (i.e deriving the adjoint equations in continuous form then discretizing the resulting equations in time/space) becomes infeasible. Alternatively, the spatially discretized equations (e.g. resulting from the application of the method of lines) can be used and processed by automatic (or algorithmic) differentiation (AD) software to produce the associated adjoint code [31] (i.e. discretize and then differentiate approach). In chapter 4 the applicability of such algorithms is examined in extracting sensitivities with respect to the model/physical parameters of unsteady char combustion. To address the impact of unsteadiness on the extracted sensitivities,

time-dependent evolution of sensitivities are also analysed. Additionally, the evolution of sensitivities is compared across different free streams to emphasize the influence of oxy-fuel conditions on the gradients.

Char combustion has been used as a starting point to develop various methods for simulating solid fuel combustion and to demonstrate effective ways of extracting sensitivities for non-trivial boundary conditions. However, the simplified model of gas phase chemistry used in chapters 2, 3, and 6 has limited the capability of including more complex phenomena such as devolatization process, which is crucial in reactive solid fuel simulations. Additionally, as demonstrated in 2, gas phase combustion has a significant impact on the extracted sensitivities. Therefore, studying gas phase kinetic models, as done in chapter 5, is a top priority.

In addition to sensitivities, the uncertainties of the model parameters in the predictions of the quantities of interest also needs to be assessed. As far as uncertainties are concerned, Monte Carlo methods have traditionally been applied to assess the existing model uncertainties. However, their slow convergence and high computational cost have given rise to alternative approaches that reduce the cost by considering a smaller set of the parameter space. Some of these approaches include probabilistic methods such as Polynomial Chaos Expansion (PCE) [32] and related methods [33, 34] applicable to high-dimensional parameter spaces, and Gaussian process approximation method (Kriging) [35]. In most of these approaches, a response surface is formed from function evaluations (computationally intensive unsteady simulations) at sparsely and carefully selected points to approximate the dependence between the model parameters (input) and the quantity of interest (output). In the combustion community, the large number of parameters has motivated the development of various techniques to further speed up the construction of the response surfaces, some based on sensitivity analysis [36], High Dimensional Model Representations (HDMR) [37] and Artificial Neural Networks (ANN) [38]. A comprehensive review of response surface methods in the context of combustion simulations can be found elsewhere [39]. While effective in their own rights, most of these methods suffer from the curse of dimensionality and are not applicable as the number of parameters increases beyond a certain threshold, which is the case when considering detailed kinetic models of interest to this study. Some remedies include resorting to sensitivity analysis in order to lower the dimension of the parameter space. These methods can be divided into local and global alternatives. In local estimation methods, the parameter space is reduced based on the local estimations of the gradient; these methods therefore suffer from shortcomings such as sensitivity

to noise. Global methods provide more robust sensitivity estimates, at a significant additional cost however [40, 41]. Alternatively, in the case of PCE, collocation techniques with sparse quadrature or adaptive regression strategies [42, 43] have been used to reduce the high-dimensional parameter space when constructing the response surface. These methods mainly rank the coordinates of the inputs. However, some models may vary most prominently along directions of the input space that are not aligned with the coordinate system. Therefore, in this study, I adopt a different strategy, namely the Active Subspace Method (ASM) [40], where gradient information is used to detect and exploit the directions of the strongest variability of a given function to construct an approximation on a low-dimensional subspace of the function's inputs. ASM has successfully been applied to analyze the chemical kinetic uncertainty for liftoff height in a turbulent combustion application [44]. In a later work, Ji *et al.* [45] develop a method to simultaneously approximate the marginal PDFs of multiple quantities of interest, in particular, Ignition Delay Time (IDT) in an isobaric reactor and Laminar Flame Speed (LFS), based in both cases on the identification of a single active direction. In a recent work, Su *et al.* [46] have also employed an active subspace method together with sensitivity analysis to identify extreme low-dimensional active subspaces of the input parameter space of a dimethyl ether (DME) mechanism. Using ASM, a certain number of gradient evaluations at distinct sample points in the input parameter space are required to obtain good estimates of the dominant directions. These gradients are usually estimated by either finite differences or local linear fitting, and the cost of their evaluation increases linearly with the number of parameters. Here, I leverage the adjoint method [47] to compute gradient information at a cost comparable to a single function evaluation. Furthermore, the adjoint method is also used to provide a linear approximation of uncertainties in the active direction (LAAM). To the best knowledge of the authors, LAAM has never been applied to analyse uncer- tainties of chemical reaction networks, and in this respect this work shows one of its first applications. I show that LAAM is an accurate way of defining uncertainties for this problem with a much lower cost, making this method a practical tool for extracting uncertainties, especially useful for large mechanisms. Cases are also considered where a single dominant direction can not be identified and a strategy is provided in order to include multiple active directions in the analysis. Finally, the limitations of the LAAM approach are presented and discussed.

The preceding chapters delved into various methods for extracting sensitivities and quantifying uncertainties, specifically in solid fuel combustion, with a

focus on char burnout and gas phase kinetics. Rather than scrutinizing each phenomenon in isolation, as in Chapters 2,4, and 5; Chapter 6 takes a more comprehensive approach by identifying sensitivities and quantifying uncertainties of different model parameters in solid fuel combustion simulations for unsteady configurations that couple hydrodynamics with detailed chemistry and thermodynamic models, including devolatization and char combustion. This approach facilitates a more comprehensive understanding of the bigger picture.

To extract sensitivities for a large number of model parameters, previous chapters utilized the adjoint method for unsteady configurations, as outlined in Chapter 4. The local gradients obtained through this approach can also aid in defining the uncertainties of different model parameters, as demonstrated in Chapter 5. The active subspace method is a powerful tool for determining the dominant direction in the objective function space, thereby overcoming the curse of dimensionality prevalent in most reactive flow simulations. While this method is primarily used in the context of zero-dimensional configurations, as demonstrated by previous researchers, the exceptional results obtained in Chapter 5 motivated its application to more complex configurations, such as unsteady axisymmetric particle combustion. The extracted sensitivities and uncertainties were then compared for air and oxy-fuel conditions to elucidate the effect of the atmosphere on the model uncertainties.

This study is organized as follows: Chapters 2, 3, and 4 will concentrate on char burnout simulation and the sensitivity of relevant quantities of interest (QoI) with respect to different model parameters. Chapter 5 will focus on the uncertainty quantification and sensitivity analysis of the gas phase kinetics, which is a prime concern for the devolatilization process. Finally, Chapter 6 will combine both char combustion and devolatilization processes in an unsteady single-particle combustion configuration to extract the sensitivities and uncertainty quantification of various QoI in a more realistic configuration. This will allow analysis of the mutual interaction between all different phenomena (thermodynamics, gas phase kinetics, devolatilization, etc.).

2

Sensitivity analysis of steady char combustion

In this chapter, I begin by simulating the steady char combustion process of a single particle. The aim is to evaluate the performance and applicability of various sensitivity analysis methods, including discrete and continuous adjoints, and compare them to conventional approaches like finite differences and forward sensitivity analysis. I compare the accuracy of the sensitivities obtained using these different methods with analytical gradients in the frozen limit (i.e., no gas phase combustion). Once I identify the most accurate method, I consider various quantities of interest in the nonlinear limit and report sensitivities with respect to the relevant combustion parameters for two different free stream compositions, representing air and oxy-atmospheres. This chapter serves as a benchmark for sensitivity extraction using the adjoint technique in the subsequent chapters, where I will explore uncertainty quantification and global sensitivity analysis for an unsteady configuration.

2.1. Governing equations

Assuming a coal particle immersed in air, combustion is described by the following heterogeneous reactions on the surface of the particle (referred to as *direct* and *indirect* oxidation, respectively),

$$C\,[s] + \frac{1}{2}O_2 \rightarrow CO, \tag{2.1}$$

$$C\,[s] + CO_2 \rightarrow 2CO. \tag{2.2}$$

The following one-step mechanism is then considered for the oxidation of carbon monoxide in the gas phase,

$$\mathrm{CO} + \frac{1}{2}\mathrm{O}_2 \rightarrow \mathrm{CO}_2. \tag{2.3}$$

The evolution of the gaseous composition is described by the species mass fraction equations,

$$\nabla \cdot \left[\rho Y_i \left(\mathbf{v} + \mathbf{V}_i\right)\right] = \omega_i, \tag{2.4}$$

where $i = 1, \cdots, 4$, refer to fuel (CO), oxidizer (O_2), product (CO_2), and inert gas (N_2), respectively. ρ denotes the mixture density, $\mathbf{v}$ the mass-averaged velocity, and $\mathbf{V}_i$ the diffusion velocity for species i. The term on the right hand side of the above equation is, $\omega_i = \mathcal{W}_i(\nu_i'' - \nu_i')\omega$, where ν_i'' and ν_i' are the stoichiometric coefficients of the product and reactants in the homogeneous reaction, respectively, while $\mathcal{W}_i$ denotes the molecular weight of species i. The

homogeneous reaction rate obeys an Arrhenius law [48],

$$\begin{aligned}\omega &= k\,[CO]\,[O_2]^{\frac{1}{2}}\,[H_2O]^{\frac{1}{2}}\exp\left(-\frac{E}{RT}\right),\\ &= \frac{kY_{H_2O}^{\frac{1}{2}}}{\mathcal{W}_{CO}\mathcal{W}_{O_2}^{\frac{1}{2}}\mathcal{W}_{H_2O}^{\frac{1}{2}}}\rho^2 Y_{CO}Y_{O_2}{}^{\frac{1}{2}}\exp\left(-\frac{E}{RT}\right),\end{aligned} \tag{2.5}$$

where, $K = 1.23 \times 10^8 sec$, $E = 125400\ J/mole_C$, $Y_{H_2O} = 10^{-3}$, and W_i denotes the molecular weight of the ith species. Using Fick's law, the diffusion velocity for species i can be closed as,

$$Y_i\mathbf{V}_i = -D\nabla Y_i, \tag{2.6}$$

where the diffusion coefficient is assumed identical for all species. Substituting the previous equation in Eq. 2.4 leads to the following transport equation for the species,

$$\nabla\cdot(\rho\mathbf{v}Y_i - \rho D\nabla Y_i) = \omega_i. \tag{2.7}$$

Similarly, assuming identical and constant specific heats, C_p, for all species, the energy equation yields the following equation for the temperature in the gas phase,

$$\nabla\cdot(\rho C_p\mathbf{v}T - \lambda\nabla T) = -\sum_{i=1}^{4} h_i^0\omega_i, \tag{2.8}$$

where h_i^0 is the enthalpy of formation of species i, and λ is the coefficient of heat conduction. The low Mach number approximation is used. Finally, the continuity equation holds,

$$\nabla\cdot(\rho\mathbf{v}) = 0. \tag{2.9}$$

For the purpose of this study, ρD is assumed constant and the Lewis number, $Le = \lambda/\rho DC_p$ is set to unity. The variables are made dimensionless by introducing the following characteristic values, as proposed by Matalon [29]: (i) The particle radius a for length, (ii) Q/C_p for temperature, where Q is the heat of the homogenous reaction per unit mass of CO_2, namely,

$$Q = -\frac{\sum_{i=1}^{4} h_i^0\mathcal{W}_i\left(\nu_i'' - \nu_i'\right)}{\mathcal{W}_{CO_2}\left(\nu_{CO_2}'' - \nu_{CO_2}'\right)}, \tag{2.10}$$

(iii) $\rho_0 = p_0C_p/Q\tilde{R}$, where $\tilde{R}$ is the specific gas constant based on an average molecular weight, p_0 is the uniform pressure, and (iv) λ/ρ_0C_pa, for velocity.

This non-dimensionalisation yields the following expression for the Damköhler number of the homogeneous reaction:

$$Da^g = \frac{k\left(\nu''_{CO_2} - \nu'_{CO_2}\right) C_p^3}{\lambda Q^2 \tilde{R}^2} \frac{\mathcal{W}_{CO_2}}{\mathcal{W}_{CO}\mathcal{W}_{O_2}^{12}\mathcal{W}_{H_2O}^{\frac{1}{2}}} a^2 p_0^2 Y_{H_2O}^{\frac{1}{2}}. \tag{2.11}$$

In non-dimensional form, the equation of state (ideal gas) reads $\rho T = 1$, and the (dimensionalized) governing equations are

$$\begin{aligned} \forall i \in [\![1,4]\!], \mathcal{L}\left(Y_i\right) &= \Omega\overline{\alpha}_i, \\ \mathcal{L}\left(T\right) &= \Omega\overline{\alpha}_5, \end{aligned} \tag{2.12}$$

where, $\left(\overline{\alpha}_i\right)_{i\in[\![1,5]\!]} = (\overline{\alpha}-1, -\overline{\alpha}, 1, 0, 1)$, and $\overline{\alpha} = \mathcal{W}_{O_2}/2\mathcal{W}_{CO_2}$, with the transport operator defined as

$$\mathcal{L}\left(\varphi\right) = \nabla\cdot\left(\rho\mathbf{v}\varphi - \nabla\varphi\right), \tag{2.13}$$

where, $\varphi = \{Y_i, T^*\}$, and

$$\Omega = Da^g \frac{Y_{CO} Y_{O_2}{}^{\frac{1}{2}}}{T^2} \exp\left(-\frac{\theta}{T}\right). \tag{2.14}$$

If axisymmetry is assumed, the governing equations reduce to a set of coupled second order ordinary differential equations (ODE). In the case of a single spherical particle in particular, the continuity equation (in spherical coordinates) yields

$$r^2 \rho v_r = \dot{M} = \text{constant}, \tag{2.15}$$

where r is the radial coordinate, v_r the radial velocity component, and $\dot{M}$ denotes the "burning rate". The linear operator $\mathcal{L}$ then reduces to:

$$\mathcal{L}_{spherical}\left(\varphi\right) = \frac{\dot{M}}{r^2}\frac{d\varphi}{dr} - \frac{1}{r^2}\frac{d}{dr}\left(r^2\frac{d\varphi}{dr}\right). \tag{2.16}$$

2.1.1. Boundary Conditions

Away from the particle, composition (Y_{CO}^∞, $Y_{O_2}^\infty$, $Y_{CO_2}^\infty$ and $Y_{N_2}^\infty$) and temperature (T^∞) are set. The particle is assumed isothermal ($T = T_s$ for $r < 1$), and the temperature profile is also assumed continuous, which yields the following boundary condition:

$$T\left(r=1\right) = T_s. \tag{2.17}$$

The remaining conditions at the particle surface are extracted from the conservation statements for each species i, which match the differences between the net fluxes of each species to the rates of consumption/production per unit area due to the heterogeneous reaction rates. Due to large solid to gas density ratio, the quasi-steady assumption holds, resulting in the following simplified mass balance for the i^{th} species

$$\rho \mathbf{v} \cdot \mathbf{n} Y_i Y_i^s - \rho D \left. \nabla Y_i \right|^s \cdot \mathbf{n} = \omega_i', \tag{2.18}$$

where $\mathbf{n}$ denotes the outward-pointing normal to the particle surface, and ω_i' their respective reaction rate per unit area, due to the heterogeneous reactions. The boundary conditions are non-dimensionalized similarly to the governing equations variables. The non-dimensionalized boundary conditions in axisymmetric form are then given as,

$$\dot{M} Y_i^s - \left. \frac{dY_i}{dr} \right|^s = \omega_i'. \tag{2.19}$$

Assuming both heterogeneous reactions are first order [29], the following two heterogeneous Damköhler numbers are defined,

$$\forall i \in [\![1,2]\!], Da_i^s = \frac{C_p^2}{\lambda Q \overline{R}} a p_0 \frac{k_i\left(T^s\right)}{T^s}, \tag{2.20}$$

for the direct ($i = 1$) and indirect ($i = 2$) oxidation reactions. This yields the conditions:

$$\dot{M} Y_i^s - \left. \frac{dY_i}{dr} \right|^s = Da_1^s \beta_i Y_{O_2}^s + Da_2^s \gamma_i Y_{CO_2}^s, \tag{2.21}$$

where $(\beta_i)_{i \in [\![1,4]\!]} = \left(\left(1-\overline{\alpha}\right)/\overline{\alpha}, -1, 0, 0\right)$ and $(\gamma_i)_{i \in [\![1,4]\!]} = \left(2\left(1-\overline{\alpha}\right), 0, -1, 0\right)$.

2.2. Two-point boundary value problem and adjoint-based gradient computation

In this section, the equations governing the char particle combustion, previously described in detail, are presented in the form of a more general two-point boundary value problem, and the corresponding continuous and discrete adjoint formulations are then presented.

2.2.1. Two-point boundary value problem

The problem delineated above forms a two-point boundary value problem, the sensitivities of which are to be computed using the adjoint method. To derive the adjoint equations, the methodology proposed by Serban & Petzold [49] is used. Let the governing equations be recast in first order form: $\Phi(r) \in \mathbb{R}^m$ ($m \in \mathbb{N}$) denotes the dependent variable, which in this case includes species mass fraction and temperature derivatives as follows:

$$\Phi = \left(Y_{CO}, Y_{O_2}, Y_{CO_2}, Y_{N_2}, T, \dot{M}, \frac{dY_{CO}}{dr}, \frac{dY_{O_2}}{dr}, \frac{dY_{CO_2}}{dr}, \frac{dY_{N_2}}{dr}, \frac{dT}{dr} \right).$$

The solution of the problem delineated in the previous section is then obtained by solving a two-point boundary value problem of the form:

$$\frac{d\Phi}{dr} = \mathbf{F}(r, \Phi, \mathbf{p}),$$

to be solved from $r = a = 1$ (the particle surface) to $r = b = \infty$ subjected to the boundary conditions

$$\mathbf{h}(\Phi(a), \Phi(b), \mathbf{p}) = 0.$$

$\mathbf{p}$ denotes the problem parameters, that include the mixture composition away from the particle surface or the Damköhler numbers in the case of interest here.

For the problem to be well-posed, the boundary condition operator $\mathbf{h}$ must provide m independent boundary conditions. This is satisfied as long as the Jacobian,

$$\mathbf{h}_\Phi = \left[\mathbf{h}_{\Phi(a)} | \mathbf{h}_{\Phi(b)} \right] = [\mathbf{A}|\mathbf{B}], \tag{2.22}$$

has full rank ($\mathbf{h}_{\Phi(a)} = \mathbf{A}$ denotes the Jacobian of $\mathbf{h}$ w.r.t. $\Phi(a)$, likewise for $\mathbf{h}_{\Phi(b)} = \mathbf{B}$ and $\Phi(b)$). The matrices $\mathbf{A}$ and $\mathbf{B}$ that result from the problem of interest are included in A.2. In its first-order form, the two-point boundary value problem may be solved numerically using well-documented techniques, such as collocation or shooting methods. The latter was used in this work: it consists in solving the original problem as an initial value problem using readily available ODE integrators. The integration is performed outward from the particle surface but, since initial data such as mixture composition are missing, it is estimated and iteratively updated until the far-field conditions are matched. The iterative solver employed in this work is the Levenberg-Marquardt algorithm, which proved able to handle all the cases presented in the results section.

2.2.2. Continuous adjoint formulation

This section describes the derivation of the continuous adjoint equations, solved in the differentiate-then-discretise approach to adjoint-based gradient computation. The methodology followed here was proposed by Serban & Petzold: it focuses on the gradients of two types of functionals:

- Local (or pointwise) quantities, of the form $g\left(s, \Phi, \mathbf{p}\right)$, where $s \in [a, b]$. This approach will be applied to the computation of the gradient of the burning rate at the particle surface with respect to model parameters ($s = a$).
- Integral quantities, of the form:

$$G^s\left(\mathbf{p}\right) = \int_a^s g\left(r, \Phi, \mathbf{p}\right) dr.$$

  One application is the computation of the gradient of the integrated heat release ($s = b$).

The two problems are related by the Leibniz integral rule:

$$\frac{d}{ds}\frac{dG^s}{d\mathbf{p}} = \left.\frac{dg}{d\mathbf{p}}\right|_s, \tag{2.23}$$

or stated otherwise, the gradient of g matches the sensitivity of the gradient of G^s with respect to s. As a result, both gradients can be computed by the adjoint method as follows:

1. Solution of the primal two-point boundary value problem, by means of shooting or collocation methods, as highlighted above.
2. Solution of the adjoint of the primal problem. This is a linear multi-point boundary value problem, which, in the limits $s \to a$ and $s \to b$ degenerates into a linear two-point boundary value problem.

As shown by Serban & Pezold, these two steps are sufficient to compute

$$\frac{dG^s}{d\mathbf{p}} = \int_a^s \left(g_\Phi \Phi_\mathbf{p} + g_\mathbf{p}\right) dr. \tag{2.24}$$

In the event where the gradient of the local quantity g evaluated at s is of interest, the second step is replaced by:

2. Solution of the forward sensitivity of the adjoint problem with respect to s. This step gives rise to another linear multi-point boundary value problem that too degenerates into a linear two-point boundary value problem in the limits $s \to a$ and $s \to b$.

For the sake of completeness, A.1 delineates the procedure in depth.

2.2.3. Discrete adjoint formulation

Instead of deriving the continuous adjoint equations, an alternative approach, referred to as the discretise-then-differentiate approach, consists in extracting the adjoint equations directly from the discretised primal problem. in this method, algorithmic differentiation is used to linearize and formulate the conjugate transpose equations, ultimately yielding the discrete adjoint formulation. Since the discrete adjoint equations are extracted from the primal problem after the discretisation is performed, the adjoint and the primal grids are identical. This is one of the main differences between the continuous and the discrete approaches.

2.3. Validation

In this section, the primal problem is first presented and validated in the frozen limit against analytical solutions. Once validated, sensitivities are extracted using the approaches to gradient computation discussed previously for a selected configuration. The advantages of each approach are highlighted in order to select the most suitable strategy. The following parameters are taken from the work of Matalon [29]: the homogeneous reaction frequency is set to $k = 1.3 \times 10^{14}$ $[mole/ml.sec]$, the pressure range to $1 \leq p_0 \leq 10$ $[atm]$, and the water mass fraction to $Y_{H_2O} \approx 10^{-3}$. The particle size, a, ranges between 10 $[\mu m]$ and 100 $[\mu m]$. Using these values, the expression for Da^g becomes, $Da^g = 4.2 {Y_{H_2O}}^{\frac{1}{2}} a^2 p_0^2$.

2.3.1. Primal problem

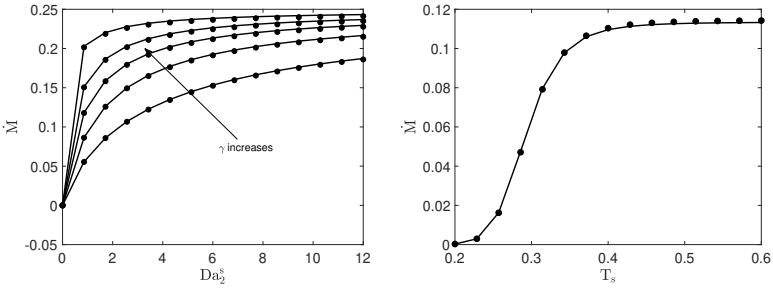
In this section, the solution of the primal problem is compared to the analytical solution in the frozen limit, where $Da^g = 0$. The values of mass fractions and temperature in the far-field are set to $Y_{CO}^{\infty} = 0.05$, $Y_{CO_2}^{\infty} = 0.2$, $Y_{O_2}^{\infty} = 0.3$, $Y_{N_2}^{\infty} = 0.45$, $T^{\infty *} = 0.056$ and $\gamma = Da_2^s / Da_1^s = 0.1$, as suggested by Matalon [29, 50]. The far field temperature is set to $T^{\infty} = 360$ $[K]$, similar to the case studied by Matalon [29]. The dependency of the burning

rate on Da_1^s in the frozen limit ($Da^g = 0$), is shown in figure 2.1(a), for $0.1 \leq \gamma \leq 5$, and is compared to the analytical value. A comparison of approximated value for the burning rate, computed for different domain sizes (not shown here), showed that $L = 120a$ is the smallest length beyond which the solution becomes approximately independent of the domain size. However, figure 2.1(a) shows that increasing the Damköhler number increases the error in the approximated solution. Changing the Damköhler number in a steady-state case alters the balance between diffusion time and chemical reaction time, influencing the slope of the mass fractions profiles and amplifying the effect of the far-field boundary conditions. Increasing the domain size for higher Damköhler numbers reduces the resulting error. However, for the purpose of this study, since the resulting errors are in the acceptable range, the domain size is kept identical for all cases, and henceforth all the computations are performed on domain sizes $L \geq 120a$. As predicted by Matalon [29], for small Da_1^s, the surface reactions are very weak and the burning rate tends towards zero. The value of the burning rate, $\dot{M}$, on the other hand, increases with Da_1^s and moves asymptotically to $\dot{M}^\infty = 0.2432$. Figure 2.1(b) shows the dependence of the burning rate on the particle surface temperature T_s. The predictions of the simulations are compared to the explicit expression derived by Makino [51], where $T^{\infty *} = 0.25$ which corresponds to $T^\infty = 2530\ K$, $Y_{O_2}^\infty = 0.1602$, $Y_{CO_2}^\infty = 0$ and $Y_{N_2}^\infty = 0.7398$. This expression is valid for burning rates sufficiently smaller than unity, an assumption which holds for the set of parameters chosen for this comparison.

2.3.2. Extracted sensitivities

In this section, both the continuous and discrete adjoint methodologies are validated against the extracted sensitivities from the analytical solution of the primal problem, and the most suitable strategy, for applications of interest to this study, is identified. The accuracy of the adjoint methods is also compared to conventional methods such as finite difference and forward sensitivity.

Figure 2.2 compares the error in the estimated sensitivities. The values of mass fractions and temperature in the far stream are identical to the ones previously used. The results are reported for $\gamma = 0.1$. A high value of γ results in higher flame temperatures, leading to larger gradients in the species and temperature fields, and resulting in more clear comparisons. While all methods result in similar values for the extracted sensitivity, the discrete adjoint methodology proves to be the most accurate. Despite the slightly large error in the primal solution for high Damköhler numbers, which decreases the accuracy of the extracted gradients, it is found that the discrete adjoint



(a) Varying surface Damköhler numbers Da_2^s **(b)** Varying surface temperature T_s

Figure 2.1.: Comparison of the burning rate, predicted by the simulations, to the theoretical solution, in the frozen limit. —, analytical solution; •, numerical solution.

is significantly more accurate than the other gradient extraction approaches in this case. Increasing the surface Damköhler number results in a solution closer to the asymptotic limit for the primal problem, which can be seen in figure 2.1(a). In this region, the accuracy of the forward solution also decreases, showing higher errors compared to the exact values. As a result, the increase in the estimated errors of the gradient can be attributed to the errors of the numerical scheme rather than the gradient extraction method. Moreover, the discrete adjoint approach garantees the numerical consistency of the adjoint operator. The continuous adjoint approach however, while garanteeing the consistency at the continuous level, relies on independent integrations of the primal and adjoint problems. As a consequence, inconsistencies may arise which can, as documented in related studies, lead to higher errors in the gradient prediction and in some cases even to the instability of the results [52]. The forward sensitivity and continuous adjoint predictions are very close. This is expected, since in both cases, the analytical expression is extracted by applying linear perturbation to the primal problem in continuous form. It should be noted that the finite difference results vary based on the chosen value of ϵ in $(F(x+\epsilon) - F(x))/\epsilon$. The optimized value of ϵ was selected here by comparing to the results of the other sensitivity extraction methods. This highlights one of the disadvantages of the finite difference strategy.

As previously mentioned, while the grid used in the discrete adjoint is the same as that of the primal problem, the grid of the continuous adjoint solution

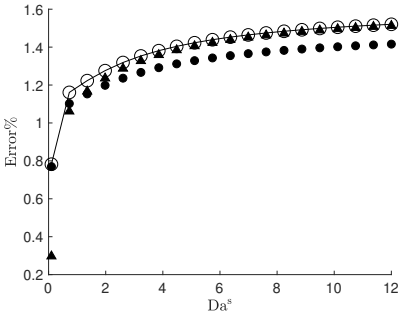


Figure 2.2.: Error comparison of burning rate sensitivity with respect to Da_1^s. •, discrete adjoint; —, continuous adjoint; ▲, finite difference; ∘, forward sensitivity. Error computed with respect to the analytical solution of the adjoint problem.

is different. Figure 2.3 compares the grids of the different gradient extraction strategies including forward sensitivity. For clarity, only one out of eight grid points is displayed. The total numbers of grid points are $N_{grid} = [769, 313, 233]$ for continuous, discrete adjoints, and forward sensitivity, respectively. In all cases, the grid points accumulate at the particle surface, due to the presence of the heterogeneous reactions. While the distance between the grid points increases in both discrete and forward sensitivity methods when moving away from the particle surface, the continuous adjoint shows accumulation of grid points at the far stream boundary, due to the backward integration of the continuous adjoint problem, derived in A.1. The non-linearity of the problem requires the use of a checkpointing algorithm. In the case of the discrete adjoint, since the grid matches that of the primal problem, the solution is available at each checkpoint. However, due to the differences in the grid distributions in the continuous adjoin approach, an interpolant (cubic splines, in this case) is used in between the checkpoints. As a consequence, the interpolation gives rise to significant errors in the gradient computed using the continuous adjoint approach. This error is not only due to the accuracy of the interpolant, but rather to the large discrepancies between the two grids, as shown in figure 2.3, which result in inaccuracies in the construction of the interpolant.

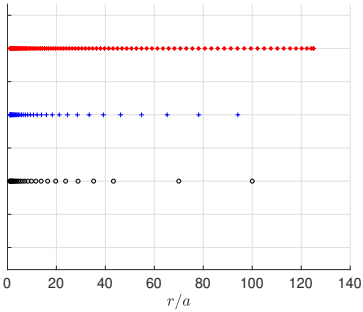


Figure 2.3.: Comparison of the grids used in the different approaches: primal (∘), continuous adjoint (*), and forward sensitivity (+) problems.

2.4. Results

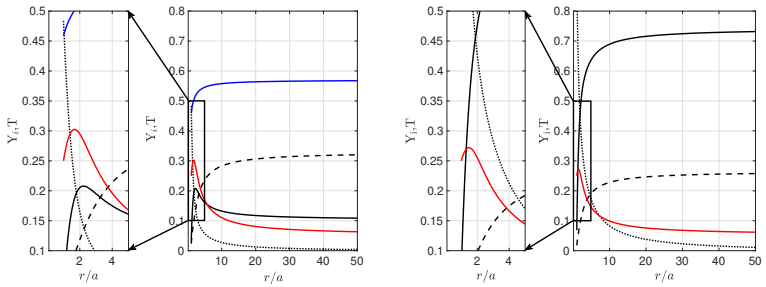
In this section, various quantities of interest (QoI's) are identified, locally or spatially distributed, and their sensitivities with respect to the existing combustion parameters are extracted. In addition, these sensitivities are extracted considering two different environments, as illustrated in Table 2.1, and are compared. Oxy environment is of interest in coal combustion, as one of viable methods to reduce CO_2 emissions [53]. In the oxy environment, air is replaced by pure oxygen (O_2) or a mixture of oxygen with recycled flue gas, generating high CO_2 concentrations, and causing the combustion process to change significantly. The conditions for the two environments in Table 2.1 closely match the conditions imposed in the simulation of Farazi *et al.* [4].

Test case	Diluent	$Y^{\infty}_{O_2}$	Y^{∞}_{CO}	$Y^{\infty}_{CO_2}$	$Y^{\infty}_{N_2}$
Air-atmosphere	N_2	0.326	0.0	0.105	0.569
Oxy-atmosphere	CO_2	0.262	0.0	0.738	0.0

Table 2.1.: Environments considered for sensitivity analysis.

While the asymptotic limits $Da^g = 0$ and ∞ provide analytical solutions that can be used to validate the models/numerical methods, in real configurations, the reactions in the gas phase can not be ignored and the results obtained in the frozen limit are not applicable. In what proceeds, the focus is therefore

set on finite Da^g values. One such case for both air and oxy atmospheres is shown in figure 2.4, with the following parameter values: $a = 130$ $[\mu m]$, $p_0 = 1$ $[atm]$, $Y_{H_2O} = 0.001$, and the corresponding Damköhler numbers, $Da^g = 2500$, $Da_1^s = 6$, and $\gamma = 3$. In this case, a flame is present in the gas phase and its location is highlighted by the profiles of temperature and carbon dioxide mass fraction reaching their maximal value, at $r/a = 1.675$ for air atmosphere, and $r/a = 1.475$ for oxy atmosphere. The location of the maximum temperature, where substantial heat release and oxygen consumption occur, can be qualitatively compared to the two-dimensional direct numerical simulations of Farazi *et al.* [4]. Although the values obtained for maximum temperature, for air atmosphere $T_{max} = 2140$ $[K]$, and for oxy-atmpophere $T_{max} = 1910.5$ $[K]$, compare well to those of the two-dimensional simulations [4], a shift in the flame position is observed. This shift can be attributed to the presence of a free-stream velocity in the simulations of Farazi *et al.* [4], advecting the gas away from the particle surface. Since the system is diffusion dominated, the behaviour of the diluent species, whether it is a reactive species like carbon dioxide in oxy environment, or an inert species like nitrogen in the air environment, is similar, as illustrated in figures 2.4(a) and 2.4(b). On the other hand, for the air atmosphere, carbon dioxide behaves similar to the temperature profile, and can therefore be used to identify ignition in the gas phase.

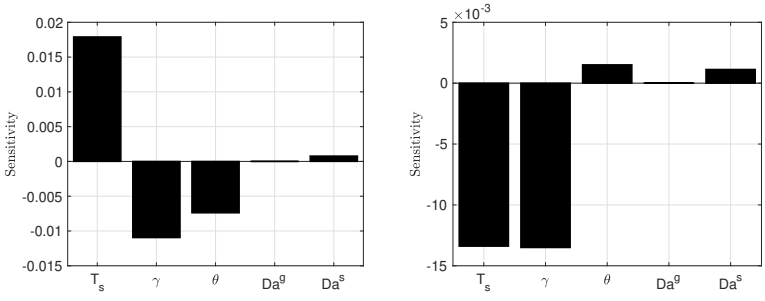


(a) Air atmosphere **(b)** Oxy atmosphere

Figure 2.4.: Evolution of mass fractions and temperature in the presence of a flame in both air and oxy atmospheres for $\mathrm{Da}^g = 2500$, $Da_1^s = 6$, and $\gamma = 3$: - - -, Y_{O_2}; —, Y_{N_2}; —, T; —, Y_{CO_2}; $\cdots$, Y_{CO}.

The burning rate, $\dot{M}$, which in this study represents a local quantity, has obvious physical importance, since it determines the value of Stefan flow

velocity imposed on the particle surface due to char combustion, and is an indication of the non-linear interaction between flow and chemistry. This value has also mathematical significance, since it corresponds to the eigenvalue of the dynamical system. Therefore, the sensitivities of $\dot{M}$ with respect to various model parameters are extracted for both atmospheres, and the results are shown in figure 2.5. In both cases, the burning rate shows the highest sensitivity to the surface parameters: particle temperature and γ. This result is expected, since T_s controls the consumption of O_2 and CO_2 at the particle surface, also reported by Makino [51], and helps overcoming the activation energy of the heterogeneous reactions. This dominance persists even when the far-field composition is altered. The gas Damköhler number is the least sensitive parameter, as far as the burning rate is concerned, and this lack of sensitivity can be easily explained by the dependency of the burning rate mainly on the surface reactions, causing the homogeneous reactions to have little impact on the predicted Stefan flow velocity. In addition, the gas Damköhler number is already quite large, leading to the conclusion that gas phase reactions are mixing-controlled. For smaller Da^g, this might change, since the homogeneous reaction provides thermal energy to the surface. Note that this result does not indicate that the heterogeneous and homogeneous reactions can be considered independently, the equations are in fact non-linearly coupled. However, it can lead to the conclusion that perturbations on the parameters controlling the intensity of the homogeneous reaction do not cause large variations in the burning rate. As far as the activation energy of the gas phase reaction, θ, is concerned, the sensitivities appear with opposite signs, as the far-field composition is altered. This can be explained by recognising that the selected operating condition for the air atmosphere results in a case with a flame in the gas phase, while for the oxy atmosphere, no flame is present. For cases with $\gamma \ll 1$, such as the two cases here, the char oxidation reaction (defined as reaction 2.1 in section 2.1) indeed dominates the burning rate. As a result, increasing the activation energy in the no flame region (oxy atmosphere), weakens the ignition possibility in the gas phase, and the gradient of oxygen mass fraction at the surface becomes positive, leading to a positive sign in the burning rate sensitivity. On the other hand, for air atmosphere, augmenting the activation energy of the gas phase in the presence of the flame, leads to an increase in oxygen consumption in the gas phase, causing a negative gradient of oxygen mass fraction at the surface, and consequently, a negative burning rate sensitivity. Similar behaviour can be seen for the sensitivities with respect to surface temperature, since changes in the surface temperature leads to similar behaviour in the gradient of oxygen



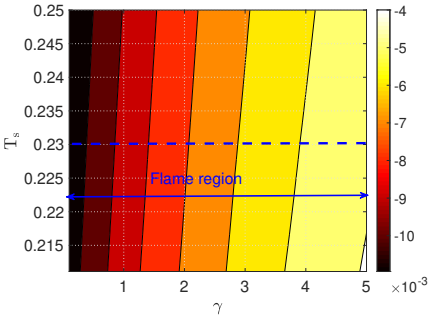
(a) Air atmosphere **(b)** Oxy atmosphere

Figure 2.5.: Burning rate sensitivity at operating values, $Da^g = 2500$, $Da_1^s = 12$, $T_s = 0.25$ and $\gamma = 0.1$.

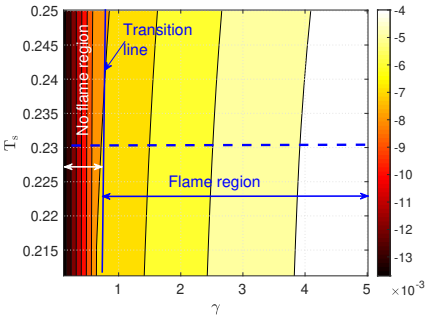
mass fraction on the surface, positive values for the air and negative values for the oxy atmosphere.

Extracted sensitivities for a spatially-distributed quantity, the total heat release (not shown here), suggest trends similar to the burning rate behavior. This quantity is of interest, since in most applications, the amount of energy extracted from the system can be easily measured. On the other hand, the total heat release also has mathematical significance, since it represents the transcendental non-linearity of the system. Based on these local results, the gradients with respect to surface parameters will be the focus the following sensitivity analysis.

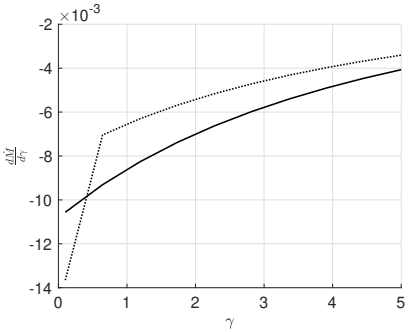
While local sensitivities, such as those presented in figure 2.5, provide valuable information on the influence of certain parameters on the selected quantity of interest, they are dependent on the local conditions of the steady state solution. Experiments and numerical simulations have shown that, various starting conditions can, for example, influence the temperature at the surface of the particle in the steady state limit, and hence alter the local conditions of the system, for which these sensitivities are extracted. Therefore, in order to provide a more comprehensive picture, these sensitivities should be extracted for all possible operating conditions rather than their local counterparts leading to the sensitivity map of the system. Here, the sensitivities are reported for varying surface temperature T_s and γ, since the local analysis of figure 2.5 highlighted these two parameters to be the most sensitive. This parameter space is sampled finely enough that the results remain unchanged with reducing the sampling plane.



(a) Air atmosphere sensitivity map



(b) Oxy atmosphere sensitivity map



(c) Sensitivity reported at $T_s = 0.23$: ——, air; $\cdots$, oxy.

Figure 2.6.: Burning rate sensitivity with respect to γ, for variable T_s and γ, in air and oxy atmospheres.

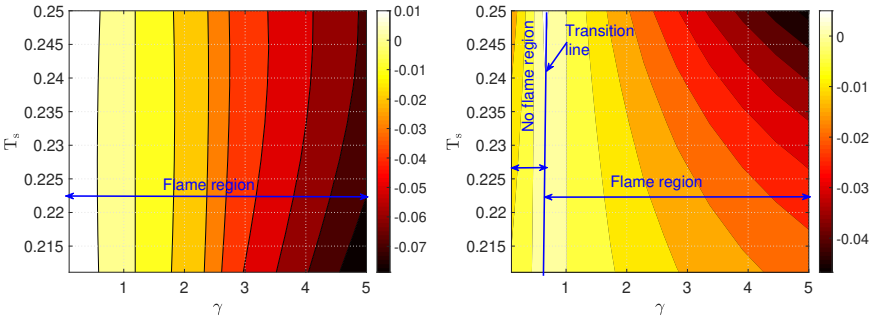
Figure 2.6 shows the sensitivity of the burning rate, $\dot{M}$, with respect to γ for varying surface temperature and γ. The range for the surface temperature T_s is chosen based on the values observed in the experiments of Schiemann *et al.* [30], whereas, the range for γ is selected such that it matches the values investigated by Matalon [29, 50]. As illustrated in the figure, the magnitude of the burning rate sensitivity with respect to γ decreases as the value of γ increases. This behaviour seems to be independent of the composition of the surrounding environment, although the level of sensitivities is generally lower (in absolute value) in the oxy atmosphere than in air. This fact can be explained by analysing the analytical relation of the burning rate gradient with respect to γ. In order to extract this expression, first, the equation governing the evolution of burning rate is formally derived, by adding all the source terms of the heterogeneous reactions, leading to the rate of consumption of char by surface reactions, leading to,

$$\dot{M} = Da_1^s \left(\frac{1 - 2\overline{\alpha}}{\overline{\alpha}} \right) Y_{\mathrm{O}_2} + Da_2^s \left(1 - 2\overline{\alpha}\right) Y_{\mathrm{CO}_2}. \tag{2.25}$$

Taking the derivative of this equation with respect to $\gamma = \frac{Da_2^s}{Da_1^s}$, gives:

$$\frac{d\dot{M}}{d\gamma} = Da_2^s \left[\left(\frac{1 - 2\overline{\alpha}}{\overline{\alpha}} \right) \left(-\frac{1}{\gamma^2} Y_{\mathrm{O}_2} + \frac{1}{\gamma} \frac{dY_{\mathrm{O}_2}}{d\gamma} \right) + (1 - 2\overline{\alpha}) \frac{dY_{\mathrm{CO}_2}}{d\gamma} \right]. \tag{2.26}$$

This equation highlights nonlinear relation of the burning rate gradient with respect to γ, which depends on the local values of oxygen mass fraction at the surface of the particle, first term on the right-hand side of the equation, as well as the gradients of oxygen and carbon dioxide mass fractions, second and third terms respectively. The overall sensitivity, reported in figure 2.6, therefore, depends on the manner in which each of these terms evolve. Further analysis of each term (not shown here) shows that throughout the chosen parameter range, the local value of oxygen mass fraction has the highest absolute value compared to the rest, and therefore dominates the behaviour of equation 2.26. As γ increases, the local value of oxygen mass fraction at the surface decreases, leading to the decrease of the overall sensitivity. From a physical stand point, since the mass fraction of oxygen on the surface governs the oxidisation of char through reaction 2.1, it is expected to have a considerable impact on the value of burning rate and its sensitivity. In addition, in the oxy atmosphere, due to the absence of the flame in the low γ region, the variation of burning rate with respect to γ is more abrupt that in the case with the surrounding air. This behaviour can be better illustrated by comparing the



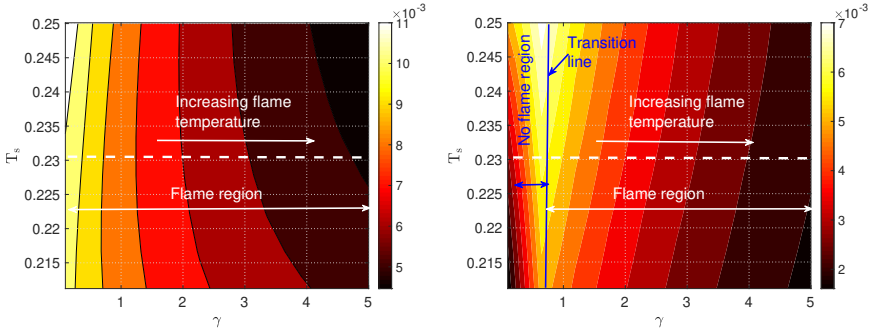
(a) Air atmosphere **(b)** Oxy atmosphere

Figure 2.7.: Burning rate sensitivity with respect to surface temperature, T_s, in air and oxy atmospheres.

sensitivities, for a variable γ, at a given surface temperature. The choice of the surface temperature will not impact the analysis, since as shown by figure 2.6, this parameter induces a minor variation in the sensitivities, also supported by equation 2.26, where T_s does not appear directly. The sensitivities are extracted at $T_s = 0.23$, marked by dashed lines in figures 2.6(a) and 2.6(b), for air and oxy atmospheres, and plotted in figure 2.6(c). This figure shows that for $\gamma \ll 1$, the sensitivities in the oxy atmosphere are larger in absolute value than in air atmosphere, due to the lack of the flame in the gas-phase in the case of the oxy environment. However, for $\gamma \gg 1$, where a flame is present in both cases, the oxy atmosphere leads to lower sensitivities overall. Figure 2.7 shows the sensitivity of the burning rate with respect to the surface temperature, T_s, in the T_s and γ plane. Differentiating equation 2.25 with respect to T_s gives:

$$\frac{d\dot{M}}{dT_s} = Da_2^s \left[\left(\frac{1-2\alpha}{\alpha} \right) \left(\frac{1}{\gamma} \right) \frac{dY_{O_2}}{dT_s} + (1-2\alpha) \frac{dY_{CO_2}}{dT_s} \right]. \tag{2.27}$$

As opposed to equation 2.26, the sensitivity depends not only on the local gradients of mass fractions, but also on the local value of γ, suggesting that variations of both γ and T_s are expected to affect the extracted sensitivity maps, a fact supported by figure 2.7. However, surface temperature seems to have a more dominant effect on the extracted sensitivities of the oxy atmosphere compared to that of the air. This is due to the fact that, the surface temperature in the oxy atmosphere affects the gradient of carbon



(a) Air atmosphere **(b)** Oxy atmosphere

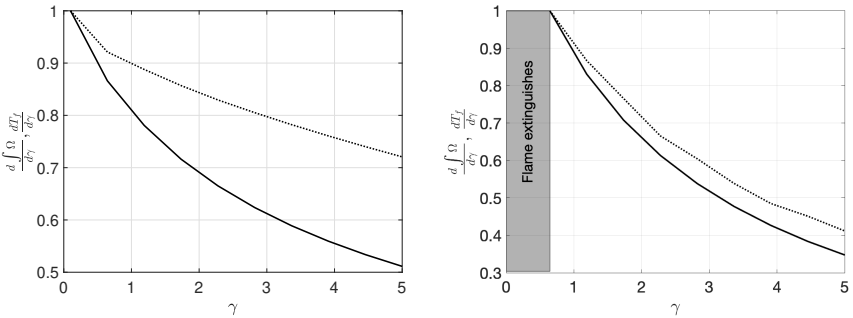
Figure 2.8.: Heat release sensitivity map with respect to γ, for variable T_s and γ, in air and oxy atmospheres.

dioxide mass fraction on the surface more drastically that in air, specifically for higher γ values. This figure also shows that, in both air and oxy environments, the sensitivities increase as γ increases. This is in contrast to the behaviour shown in figure 2.6. In addition, variations is surface temperatures (figure 2.7) seem to lead to higher sensitivities in the burning rate rather than variations in γ (figure 2.6). While figure 2.6(b) shows a monotonic decrease of sensitivities in the oxy environment through the transition from no flame zone to the region containing the flame in the gas phase, figure 2.7(b) shows a change of behaviour as the system goes through this transition line. This is mainly due to the absence of the term depending on the local mass-fraction of oxygen mass fraction in equation 2.27 compared to 2.26. In equation 2.27, the only two terms governing the behaviour of the burning rate are the gradient of the oxygen and carbon dioxide mass fractions. For $\gamma \ll 1$, the influence of the first term will dominate. However, as γ increases, this influence decreases, until finally at the transition line, the second term becomes larger than the first, leading to the change in the evolution of sensitivities, from no flame to flame regions in the oxy atmosphere. Therefore, in the presence of the flame in the gas phase, both compositions lead to negative sensitivities, whereas for $\gamma \ll 1$, the sensitivities extracted in the air are positive, in contrast to those, negative, in the oxy atmosphere. Similar behaviour was shown in figure 2.5, and the same reasoning holds.

While analysing the sensitivities of the burning rate to the surface variables is important, it is of interest to also report the sensitivities of an integrated

quantity, such as the heat release ($\int_a^b \Omega \, dr$), to the same variables, in order to examine the influence of the choice of QoI on the extracted sensitivities. In this study, the entire computational domain is included in the integral. Figure 2.8 shows a sensitivity map of the total heat release with respect to γ, for variable surface temperature and γ. Similar to figure 2.6, as γ increases the sensitivities of the total heat release decrease, while the flame temperature (T_f) increases. The comparison between the sensitivities for air and oxy atmospheres shows that the maximum sensitivities are higher for air atmosphere. However, the variation is not monotonous in oxy atmosphere, as opposed to air. While in the region where a flame is present in the gas phase, the sensitivities in both air and oxy environments decrease with the increase of γ, the behaviour of oxy atmosphere is the opposite as the flame extinguishes. This can be attributed to the fact that in char combustion, due to the presence of reactions on the surfaces, both heterogeneous and homogeneous reactions contribute to the total heat released in the system. Therefore, depending on the presence or absence of a flame in the gas phase, the behaviour of the system can change. In cases where a flame is present in the gas-phase, due to the higher enthalpy of the homogeneous reaction, and the inverse proportionality between the burning rate value and the flame temperature, the impact of the gas phase reaction on the total heat release dominates. In addition, due to the boundary conditions selected in this problem (surface temperature, T_s, being a known quantity), the contribution of surface reactions to the overall heat-release is predetermined. On the other hand, the heat release in the gas-phase is determined by the overall flame temperature, as a solution to the governing equations. Therefore, it may be expected that the gradient of the heat-release should show dependence on the gradient of the flame temperature.

Figure 2.9 shows the comparison between the sensitivity of the total heat release in the system and the gradient of the flame temperature for a given surface temperature, $T_s = 0.23$ ($T_p = 2392$ $[K]$) (shown by dashed lines in the sensitivity maps of figure 2.8). For clarity, both terms have been normalized by the maximum value of each quantity, and plotted for both air and oxy atmospheres. This figure illustrates that both quantities follow the same trend. The maximum gradient appears for the lowest value of γ in the air atmosphere. In the oxy atmosphere, however, the values are plotted only for the case where a flame is present in the gas phase. For values lower than the transition value of γ, the flame extinguishes and moves to the particle surface, where the temperature is set to $T_s = 0,23$ ($T_p = 2392$ $[K]$), and is independent of γ. In this region, the sensitivity of the total heat release is dominated by the value of oxygen mass fraction at the surface, similar to the



(a) Air atmosphere **(b)** Oxy atmosphere

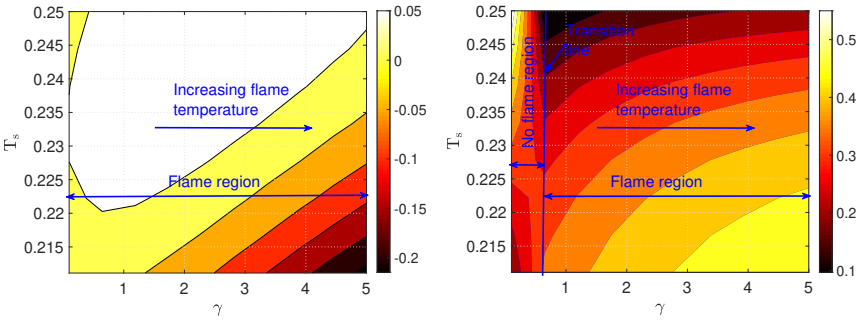
Figure 2.9.: Normalized flame temperature and total heat release sensitivities with respect to γ in air and oxy atmospheres at $T_s = 0.23$ ($T_p = 2392$ $[K]$): ——, total heat release; ....., flame temperature.

sensitivities of the burning rate with respect to γ, as was explained through equation 2.25. In contrast to the burning rate, the surface temperature seems to affect the extracted sensitivities in both cases, with a higher impact in the oxy atmosphere. Therefore, it will be of interest to also extract the sensitivities with respect to the surface temperature.

Figure 2.10 compares the sensitivities of the total heat releases with respect to surface temperature, in the T_s and γ plane for both air and oxy atmospheres. This figure shows that the maximum sensitivities for oxy atmosphere appears away from the transition line. In the region where a flame is present, the sensitivities increase as γ increases and and T_s decreases, whereas for cases where the flame is at the surface of the particle, the behaviour is the opposite for surface temperatures higher than $T_s = 0.225$ ($T_p = 2270$ $[K]$). In the air atmosphere on the other hand, the absolute value of sensitivities generally increase with increasing γ and decreasing T_s ($T_p = 2270$ $[K]$), following the same trend as the oxy atmosphere, in regions where a flame is present in the gas phase. The sensitivities of the heat release are much higher with respect to surface temperature than γ.

2.5. Summary and Conclusions

In this chapter, I introduce a framework for extracting the steady-state solution and sensitivities of different QoIs with respect to model parameters



(a) Air atmosphere **(b)** Oxy atmosphere

Figure 2.10.: Heat release sensitivity map with respect to T_s, for variable T_s and γ, in air and oxy atmospheres.

of char combustion. Both continuous and discrete adjoint approaches are introduced and compared. A two-step heterogeneous reaction mechanism and a single homogeneous reaction are used to capture the combustion process, as suggested by Matalon [29]. The results of the primal problem are then compared to the analytical results of Matalon [50] and Makino [51] in the frozen limit for verification purposes. After validating the forward solution, sensitivities extracted using customary gradient extraction techniques (forward sensitivities and finite difference) are compared to those of the continuous and discrete adjoint approaches. Examining the resulting errors suggests that the discrete adjoint is the most accurate formulation for gradient extraction, as far as steady char combustion is concerned. The comparison of sensitivity results for a single operating point (temperature, pressure, etc.) reveals that, irrespective of the atmosphere, the system is highly sensitive to parameters associated with surface reactions. This outcome is anticipated, given that the burning rate value is directly influenced by heterogeneous reactions. Since sensitivity at a specific operating point does not convey the overall gradient behavior, sensitivity maps are extracted to offer a comprehensive view of the system's sensitivities. For the parameter range examined in this study, the oxy environment exhibits two distinct behaviors: one characterized by the predominance of the flame in the gas phase, and the other observed for low values of γ, where the gas-phase flame extinguishes, and all dynamics, including the flame itself, occur on the particle surface. This leads to a more dynamic representation in the sensitivity maps. This variation is more evident in the

sensitivities derived for total heat release rather than burning rate. The heat release in char combustion stems from both heterogeneous and homogeneous reactions. In the presence of the flame, the flame temperature governs the heat release and its gradient due to the higher enthalpy of homogeneous reactions. However, when the flame shifts to the particle surface, only heterogeneous reactions dictate the heat released into the domain. Further exploration of the results under various conditions is crucial to validate the existing conclusions. Therefore, the next chapter will focus on validating sensitivity results for different operating conditions using experimental data.

3

Adjoint-based sensitivity analysis of char combustion surface reaction kinetics

In this chapter, the focus remains on studying char burnout, but with an emphasis on applying the adjoint methodology developed in Chapter 2 to actual experimental conditions, specifically in the context of heterogeneous combustion (gas-solid) over gas-phase combustion models. This study targets surface kinetics as a dominant factor in char combustion, and extracts sensitivities of various quantities of interest, such as burning rate and total heat release, with respect to different surface reaction model parameters. To achieve this, the study uses a specific single film model developed by Schiemann et al. [30], which considers the effect of oxygen stoichiometric ratio on char oxidation. The study further evaluates the variation of these sensitivities as the experimental data is varied based on the particle size and free stream composition.

3.1. Governing equations

In this section, the governing equations describing flow/chemistry, in the gas phase, and on the particle surface, along with the accompanying boundary conditions, are similar to those presented in section 2.1. The main difference is the new char combustion model developed by Schiemann *et al.* [54] which is implemented here, leading to the following heterogeneous reaction on the surface of the particle:

$$C\,[s] + \big(\frac{1+\psi}{2}\big)O_2 \rightarrow (1-\psi)\;CO + \psi\;CO_2. \tag{3.1}$$

Here, the stoichiometric ratio of oxygen depends on the value of ψ, which is determined from the relation given by Tognotti [55]. In non-dimensional form, the relation is given by,

$$\frac{\psi}{1-\psi} = 0.02P^{*s}(O_2)^{0.21}\exp\big(\frac{T_a C_p}{QT_s}\big), \tag{3.2}$$

where, $T_a = 3070\ (K)$, $P^* = \frac{P}{P_0}$ is the non-dimensional pressure, and Q is the heat of the homogeneous reaction per unit mass of CO_2, defined by equation 2.10. The oxygen partial pressure $P^s(O_2)$ is computed from the following expression,

$$P^s(O_2) = P_0\frac{Y_2^s\overline{W}}{\mathcal{W}_{O_2}}. \tag{3.3}$$

Furthermore, the total surface reaction is descried as follow,

$$\omega^s = A^s P^s(O_2)\exp\big(\frac{-E_a^s}{RT_p}\big). \tag{3.4}$$

3.2. Operating conditions and sensitivity analysis

In this section, sensitivities of multiple quantities of interest with respect to existing model/physical parameters are extracted. This study mainly focuses on the sensitivities with respect to the heterogeneous model parameters governing the reaction on the surface of the particle, as described in Section 3.1. The variation of model sensitivities is then examined as particle size, particle temperature, and free stream composition, which are varied as specified in the experiments [30].

As particle size and shape are crucial parameters for reaction kinetics determination, two measurement techniques were employed to reduce uncertainty [56]: (i) Optical thermography, based on two-color pyrometry and utilized with a stereoscopic Camera system for optical thermography (SCOT) (ii) Light microscopy (Zeiss Axiophot, image scale 1.375 μm/pixel), which allows a much easier sample handling and a higher accuracy due to the higher resolution and the stationary fixation of the particles on a flat surface. Particle surface temperature was also measured using two-color pyrometry at $\lambda_1 = 785$ and $\lambda_2 = 650$ micrometers, where similar measures were taken to reduce the uncertainty of measurements ($\approx 5\%$). Finally gas flow controllers provide accurate measurement of the reaction atmosphere.

Due to access to detailed and accurate measurement data, the adjoint-based analysis can be used to numerically provide sensitivities with respect to each measured model parameter, at each measurement location. Using the simulations to study the evolution of these sensitivities as free stream and/or particle conditions change, a trend can be extracted for the variation of sensitivities of the experimentally measured model parameters. For this purpose, eight different experimental conditions are considered and analysed as shown in table 3.1. The symbols are used to identify the measured data in all the figures of this section. Note that the particle temperature, T_s and free stream temperature (gas temperature in the experiment), T^∞, are non-dimensionalized as follows: $T_s = T_p/Q/C_p$, $T^{\infty *} = T^\infty/Q/C_p$ where $Q = 294\frac{KJ}{mol}$ and $C_p = 0.02919\frac{KJ}{molK}$, also reported in table 3.1.

Before analysing the evolution of model sensitivities, the effect of the choice of the quantity of interest (QoI) on the sensitivities, at a given measurement point (case 1 of table 3.1), is determined. For this purpose, sensitivities of representative model/physical parameters are considered. Due to linearization, the extracted sensitivity doesn't provide an actual estimation of the variation in the magnitude of the QoIs with respect to the various system parameters. However, by comparing the sensitivities of the heterogeneous

Case	$Y^{\infty}{}_{O_2}$	$Y^{\infty}{}_{CO_2}$	$Y^{\infty}{}_{H_2O}$	T_s	$T^{\infty *}$	$2 \times a$ [μm]	Da^g	Symbol
1	0.0796	0.8756	0.04477	0.1866	0.1623	121	1537	●
2	0.0851	0.8191	0.09574	0.1820	0.1570	130	1800	●
3	0.1641	0.7897	0.04615	0.2104	0.1717	125	1643	□
4	0.1758	0.7252	0.09890	0.2051	0.1646	120	1520	□
5	0.2539	0.6984	0.04761	0.2253	0.1762	123	1588	○
6	0.2727	0.6250	0.10227	0.2248	0.1654	125	1651	○
7	0.3497	0.6010	0.04918	0.2402	0.1724	107	1202	△
8	0.3764	0.5176	0.10588	0.2375	0.1659	111	1299	△

Table 3.1.: Experimental conditions, considered here for analysis [57].

model parameters to the sensitivities in free stream compositions and particle temperature, one can rank the importance of different parameters. This is important as the most sensitive parameters should be measured as accurately as possible in the experiment since they dominate the solution. Due to the large variation in their values, providing a clear comparison between the sensitivity of parameters is essential. Therefore, absolute values of the extracted sensitivities are plotted on a logarithmic scale. The selected quantities of interest are: (i) The total heat release (integrated in the spatial domain), (ii) Burning rate, and (iii) ψ, given by equation 3.2. Figure 3.1 shows the distribution of the extracted sensitivities for the identified QoIs. Comparing the sensitivities of the parameters determining the value of the heterogeneous reaction: A^s, E_a^s, and T_a, suggests that the activation energy E_a^s is generally the most sensitive parameter, as opposed to the pre-exponential factor, A^s, having the lowest sensitivities. T_a dominates the extracted sensitivities for ψ, which is also expected, as it appears directly in the expression defining this quantity (equation 3.2). While the activation energy shows high sensitivities, depending on the QoI, other physical parameters, such as the temperature at the particle surface, T_p, can contribute to comparable and sometimes larger sensitivities, suggesting that particle temperature needs to be measured extremely accurately, for the sensitivities with respect to model parameters to be meaningful.

As far as experimental observations are concerned, several studies have reported on the uncertainties in particle temperature measurements for burning char particles. Murphy Shaddix [58] use a ratio-pyrometer based on photo-multiplier tubes (PMT). The reported uncertainty in a single particle

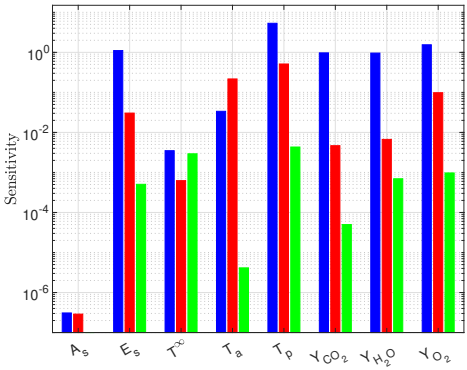
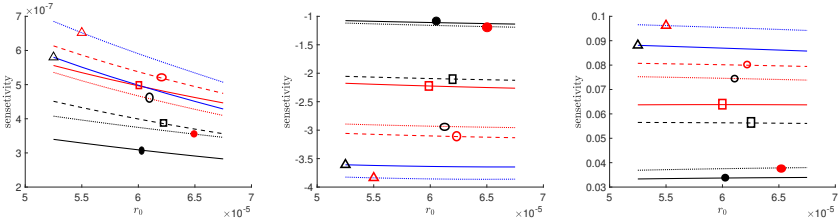


Figure 3.1.: The sensitivity of different quantities of interest with respect to existing model/physical parameters. (green), total heat release; (red), ψ; (blue) burning rate.

temperature measurement is reported to be better than 1% (approximately 20 [K]) for typical char combustion conditions. Bejarano & Levendis used another type of PMT-based three-color pyrometer and investigated glassy carbon spheres, which were supposed to be of relatively constant quality [59]. They observed a standard deviation of 70 [K] and some particle-to-particle variations, such that the systematic error in the temperature measurement is certainly smaller than this value. The technique adopted for experimental measurements in this study is based on high-speed intensified CCD cameras (a very detailed analysis of the temperature uncertainty of single particle measurements using this method is given in [56]). Although this work reports an average uncertainty of up to 4.7% for all particles accepted for further evaluation, recording several hundred particles at one residence time or conversion level reduces the error in the mean temperature. This leads to comparatively low uncertainties in the average temperature, which is used for further calculations, e.g., the determination of reaction rate parameters (a study of the influence of the measurement uncertainty is given in [30]).

Figure 3.1 also shows that the extracted sensitivities are directly dependent on the choice of QoI, similar to what has been shown in chapter 2 for total heat released and burning rate. While one QoI might lead to high sensitivities with respect to a model parameter or physical compositions of the problem, another QoI might show no sensitivities at all. Therefore, if the QoI is not

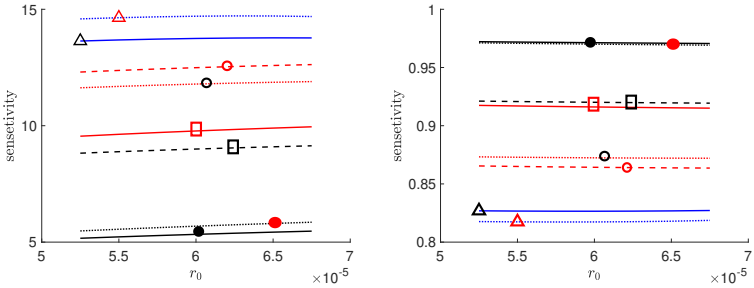


(a) A^s **(b)** E_a^s **(c)** T_a

Figure 3.2.: Evolution of model sensitivities with respect to particle size (radius), for burning rate as QoI: — & •, case 1; ··· & •, case 2; − − − & □, case 3; — & □, case 4; ··· & ○, case 5; − − − & ○, case 6; — & △, case 7; ··· & △, case 8. Lines: simulations, where the free stream and particle conditions are fixed similar as specified by the experiment, and particle size is allowed to vary; Symbols: experimental conditions.

chosen correctly, it might have misleading consequences in the interpretation of the extracted sensitivities. In case no sensitivities are reported with respect to a certain QoI for a certain parameter, it should not be concluded that the overall system is independent on the parameter, just the prediction of the selected QoI.

Since the main objective of this study is determining the sensitivities in kinetic model parameters, the evolution of the extracted sensitivities with respect to the model parameters are examined, as the conditions specified in the free stream and at the particle surface change according to the values reported by the experimental measurements. The evolution is defined such that, the parameters of each experimental configuration are fixed as specified by table 3.1, except for the particle diameter, which is allowed to vary, as shown in figure 3.2. The symbols show the corresponding measurement location of each experiment. This figure, also compares the evolution of sensitivities extracted for all heterogeneous model parameters: A_s, E_a, and T_a, although the activation energy E_a remains the most sensitive throughout. Considering the experimental conditions (symbols in the figures), independent of the model coefficient, case 8 results in the highest sensitivities, and case 1 leads to the lowest, as far as the prediction of the burning rate is concerned. The burning rate, using the heterogeneous model presented in section 3.1, is directly related to the global reaction rate, described by equation 3.4, which in turn depends on the oxygen partial pressure at the surface, $P^s(O_2)$. Increasing

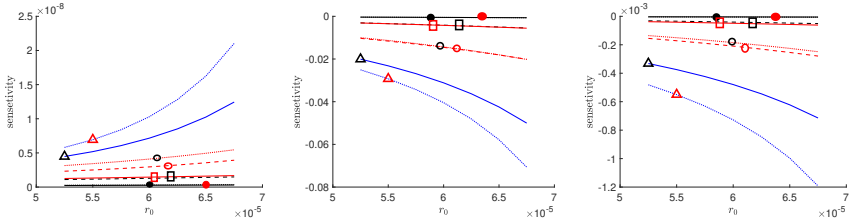


(a) T_p **(b)** Y_{CO_2}

Figure 3.3.: Evolution of sensitivities for T_p and Y_{CO_2} with respect to particle size (radius), for burning rate as QoI: — & ●, case 1; ··· & ●, case 2; − − − & □, case 3; — & □, case 4; ··· & ○, case 5; − − − & ○, case 6; — & △, case 7; ··· & △, case 8. Lines: simulations, where the free stream and particle conditions are fixed similar as specified by the experiment, and particle size is allowed to vary; Symbols: experimental conditions.

the oxygen concentration in the free stream, results in higher concentrations at the surface as well, strengthening the effect of the surface reaction, which leads to higher sensitivities in prediction of the burning rate. On the other hand, experiments have shown [56], that higher oxygen concentrations lead to higher particle temperatures, which in turn reduce uncertainties in measurements. More accurate measurements of surface temperature, may compensate the higher sensitivities reported here. Confirmation of this fact requires further research, beyond the scope of this work. When studying the evolution of sensitivities with respect to particle size (lines in figure 3.2), the experimental condition imposed through case 8, still produces the highest sensitivities of the burning rate. This figure also suggests that particle size has a weak impact on the sensitivities of the pre-exponential factor (figure 3.2(a)), with smaller particles having slightly higher sensitivities. However, the effect of particle size is negligible as far as activation energy and T_a are concerned, figures 3.2(b) and 3.2(c), respectively. Since these two parameters show higher sensitivities in prediction of the burning rate than the pre-exponential factor, A^s, it can be concluded that, the particle size has a minor effect on the extracted sensitivities of the most dominant model parameters.

Figure 3.1 shows that, as far as the burning rate is concerned, the dominant parameter regarding the prediction of its value, could indeed be the particle



(a) A^s **(b)** E_a^s **(c)** T_a

Figure 3.4.: Evolution of model sensitivities with respect to particle size (radius), for total heat release as QoI: — & ●, case 1; ··· & ●, case 2; − − − & □, case 3; — & □, case 4; ··· & ○, case 5; − − − & ○, case 6; — & △, case 7; ··· & △, case 8. Lines: simulations, where the free stream and particle conditions are fixed similar as specified by the experiment, and particle size is allowed to vary; Symbols: experimental conditions.

temperature or the free stream composition (Y_{CO_2} is selected here as a representative, other quantities such as oxygen mass fraction follow the same trend). As a result, figure 3.3 shows the evolution of sensitivities extracted with respect to these two parameters. Comparison of figure 3.3(a) and 3.2(b) shows that the sensitivities with respect to the particle temperature follow the same trend as that of the activation energy E_a^s. On the other hand, the sensitivities of Y_{CO_2} follow the opposite trend, with highest sensitivities reported for case 1. A closer inspection of this case shows higher concentrations of Y_{CO_2} in the experimental condition as well, which could explain the impact on the extracted sensitivities. The sensitivities with respect to particle temperature are higher for all the considered cases compared to the other existing model/physical parameters, with the sensitivities with respect to the activation energy of the heterogeneous reaction following closely. This results confirm the conclusion, that for all experimental conditions considered here, particle temperature should be measured accurately to allow sensitivity analysis of the model parameters.

Here, the impact of the choice of QoI on the evolution of sensitivities is examined, and instead of the burning rate, the total heat release is selected as the desired output. The evolution of sensitivities, extracted for this QoI, is shown in figure 3.4. Figure 3.1 showed that, while the activation energy E_a^s remains the most sensitive model parameter for both quantities of interest, burning rate results in higher sensitivities compared to total heat release. This

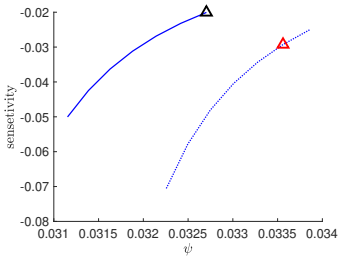
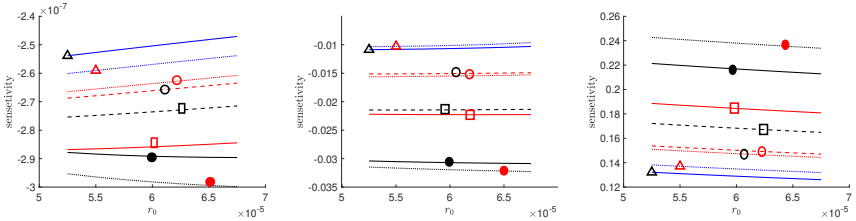


Figure 3.5.: Evolution of sensitivities in E_a^s, with respect to ψ, for heat release as QoI:— & △, case 7; ··· & △, case 8

proves to be the case for all the experimental conditions that are considered here, as comparison of figures 3.4(b) and 3.2(b) suggests. Similar to the case of the burning rate, the highest sensitivities are calculated for case 8 and the lowest for case 1. The higher oxygen concentration together with higher particle temperature in cases 7 and 8, result in higher temperatures throughout the domain, increasing the sensitivities of prediction as far as the heat release is concerned. In contrast to figure 3.2, however, the particle size has a larger effect on the extracted sensitivities, with larger particle sizes leading to higher sensitivities. For cases with highest sensitivities, cases 7 and 8, the effect of particle size is also more substantial. The pronounced dependence on particle size is due to the particular definition of Da^g (equation 2.11), used in this model, which results in quadratic dependence on the particle radius. Note that the total heat release is calculated by integrating the reaction rate in the whole spatial domain, containing the gas phase. As a result, although the sensitivities are extracted with respect to the surface parameters, the behaviour is dependent on the dynamics, prescribed by both heterogeneous and homogeneous reactions. As described in detail by Schiemann *et al.* [30], ψ is an important parameter in the calculation of rate parameters A_s and E_a^s. As a result, figure 3.5 shows the evolution of the sensitivities with respect to ψ, replacing particle size. This figure includes only the evolution of the sensitivity with respect to the most dominant parameter E_a^s, and for the experimental setup of case 8 and 7, which were the most sensitive (figure 3.4(b)). Comparing figures 3.4(b) and 3.5 shows that, plotting versus ψ rather than particle radius changes the trend in the evolution of sensitivities. Lower values of ψ result in higher sensitivities, suggesting an inverse relationship between the value of ψ and the particle size. This inverse proportionality can be explained by considering the definition of the Da^s in equation 2.20. This equation shows



(a) A^s **(b)** E_a^s **(c)** T_a

Figure 3.6.: Evolution of model sensitivities with respect to particle size (radius), for ψ as QoI: — & ●, case 1; ··· & ●, case 2; − − − & □, case 3; — & □, case 4; ··· & ○, case 5; − − − & ○, case 6; — & △, case 7; ··· & △, case 8. Lines: simulations, where the free stream and particle conditions are fixed similar as specified by the experiment, and particle size is allowed to vary; Symbols: experimental conditions.

the direct relation between the particle size and Da^s. Increasing particle size increases Da^s, resulting in faster reactions, and higher carbon dioxide production, hence reducing the oxygen mass fraction on the surface, and in turn, reducing the value of ψ, defined by equation 3.2. Therefore, all the plots reported for particle size can be interpreted similarly for ψ, considering this inverse proportionality.

Figure 3.6 shows the evolution of sensitivities extracted for ψ as the quantity of interest. As demonstrated by equation 3.2, this variable is one of the necessary parameters in determining the reaction rate of the heterogeneous reaction, and is also the solution of the equations governing the steady char combustion, explained in section 3.1. In contrast to the other quantities of interest, T_a is the most sensitive parameter as far as the prediction of ψ is concerned. Another difference to the other QoIs is that, higher sensitivities are reported for case 1 as opposed to case 8. This is expected, since T_a appears directly in the definition of ψ (equation 3.2). Considering the form of the equation, it is obvious that the sensitivity of ψ is adversely related to the partial pressure of oxygen, favoring case 1, where lower free stream oxygen concentrations are imposed by the experimental conditions. Similar to the burning rate, however, there seems to be a weak dependence on the particle size, and this could be attributed to the dominance of the heterogeneous reaction in determining the value of this parameter.

3.3. Summary and Conclusions

As a conclusion, it should be noted that, while extracted sensitivities are important in assessing and interpreting model/flow dynamics, they are, in effect, a linear local interpretation of the response of the underlying system to slight variations in model or flow parameters. For a nonlinear alternative, uncertainty quantification should be used. In experimental studies, the results are commonly reported with error bars indicating the level of uncertainties in the measurements. In order to provide similar information from simulations, the extracted sensitivities can be used to approximate such uncertainty information. Such analysis will be the considered in the following chapters of this study specially chapters 5 and 6. It should be also noted that, the extracted sensitivities are directly dependent on the choice of the kinetic model used to perform the simulations. Despite well-known weaknesses of the one-step heterogeneous model analysed here, it is commonly used in literature to give a quantitative description of different experimental or fuel-dependent parameters on the resulting reactivity, motivating its use in the experimental and numerical investigations here. However, a variety of other char combustion models exist, many of them consider more physical and chemical effects than the one-step kinetics model, which has been applied here (for example, the CBK model family [60, 61], and Senneca's model [62], to name a few). Although different in their overall structures, these models all consider multiple chemical reactions for char conversion, coupled serially and/or in parallel. Nevertheless, the model calibration to a fuel relies on a single or a few parameters of specific reactions, and the remaining parameters are defined by fixed ratios in these models. Due to the different structure of these models, the sensitivity of the model performance might not be equal to the presented case, but similar tendencies are expected. These models are far more complicated in their mathematical structure, therefore a detailed analysis of the sensitivities of the involved parameters is left to future work. Furthermore, incorporating more descriptive solid fuel combustion kinetic models such as CBK requires unsteady analysis to capture the various phenomena on different time scales. Moreover, studying devolatilization and pyrolysis processes cannot be adequately addressed in steady-state analyses, as the rapid mutual interaction between gas-phase ignition and the devolatilization processes makes it challenging to consider a single time scale. Therefore, the subsequent chapters of this study will focus on unsteady analysis.

4

Sensitivity analysis of an unsteady char particle combustion

This chapter focuses on simulations of unsteady char particle combustion, which completes the char burnout studies covered in Chapters 2 and 3. The study investigates different stages of char combustion and derives discrete adjoint equations in an unsteady limit for the algebraic differential equations governing the system. These equations are used to extract sensitivities of various time integral quantities of interest, such as particle temperature or local quantities of interest like burning rate. The sensitivities are then compared as the free stream composition changes from air to oxy atmosphere, similar to Chapter 2. The evolution of sensitivities in time is discussed and found to depend on the selected quantity of interest. The study shows that the model sensitivities with respect to heterogeneous reaction parameters, specifically oxidation of carbon, are the highest, whereas the sensitivities with respect to free stream composition are significantly lower.

4.1. Governing equations

The equations governing an axisymmetric unsteady single char particle combustion in the low Mach number limit (these assumptions eliminate the need for the momentum equation), are given below:

$$\frac{\partial \rho}{\partial t} + \frac{1}{r^\alpha}\frac{\partial}{\partial r}\left(\rho r^\alpha u\right) = 0, \tag{4.1}$$

$$\frac{\partial \rho Y_i}{\partial t} + \frac{1}{r^\alpha}\frac{\partial}{\partial r}\left[\rho r^\alpha \left(uY_i - D_i\frac{\partial Y_i}{\partial r}\right)\right] - \omega_i = 0, \tag{4.2}$$

$$\frac{\partial \rho C_p T}{\partial t} + \frac{1}{r^\alpha}\frac{\partial}{\partial r}\left[\rho r^\alpha \left(uC_pT - \lambda_g\frac{\partial T}{\partial r}\right)\right] + \sum_{i=1}^{i=n} h_i\omega_i = 0, \tag{4.3}$$

where n is the total number of species, Fick's law of diffusion and Fourier's law of heat conduction are used, t and r are independent coordinates, and α is a parameter depending on the spatial coordinate system r. For $\alpha = 0$, the above equations are written in Cartesian coordinates, $\alpha = 1$ in cylindrical coordinates, and $\alpha = 2$ in spherical coordinates. The dependent variables (Y_i), ρ, u, and T represent the mass fractions, density, radial velocity, and temperature fields, respectively. The parameters λ, C_p, and D_i are the gas thermal conductivity, the gas heat capacity at constant pressure, and species diffusivities, which are computed assuming unity Lewis number. The species are numbered as follows: $(Y_i) = (Y_{CO}, Y_{O_2}, Y_{CO_2}, Y_{N_2})$. The governing equations are transformed from the physical coordinates (r, t) to a mass-based coordinate system (χ, τ). This transformation is not necessary, but it presents

a couple of advantages. First, the velocity disappears from the transport equations, which also eliminates the need for an initial velocity profile. Second, the domain size is automatically scaled. It should be noted, however, that the applicability of the adjoint-based algorithm is independent of this choice. This transformation is achieved using the following equations:

$$\frac{\partial}{\partial r} = \rho r^{\alpha} \frac{\partial}{\partial \chi}, \tag{4.4}$$

for the spatial and

$$\frac{\partial}{\partial t} = \frac{\partial}{\partial \tau} - \rho r_0^{\alpha} u_r \frac{\partial}{\partial \chi} + \dot{m}_0^{\alpha} \frac{\partial}{\partial \chi}, \tag{4.5}$$

for the temporal derivatives. In these equations, $\dot{m}_0^{\alpha} = \dot{M}_w / C_{\alpha}$ represents the mass flux at the surface of the particle ($\dot{M}_w$) per unit surface area (C_{α}) and r_0 is the particle radius. $C_2 = 4\pi$ in the spherical case, $C_1 = 2\pi H$ (H denoting the height) in the cylindrical case, and $C_0 = HW$ (H and W denoting the height and width) in the Cartesian case. Using the identified parameters with the assumption of unity Lewis number, the equations governing the evolution of n number of species and energy are transformed as follows:

$$\frac{\partial Y_i}{\partial \tau} + \dot{m}_0^{\alpha} \frac{\partial Y_i}{\partial \chi} - \frac{\lambda_g}{C_p} \frac{\partial}{\partial \chi} \left(\rho r^{2\alpha} \frac{\partial Y_i}{\partial \chi} \right) - \frac{\omega_i}{\rho} = 0, \tag{4.6}$$

$$\frac{\partial T}{\partial \tau} + \dot{m}_0^{\alpha} \frac{\partial T}{\partial \chi} - \frac{\lambda_g}{C_p} \frac{\partial}{\partial \chi} \left(\rho r^{2\alpha} \frac{\partial T}{\partial \chi} \right) + \frac{1}{\rho C_p} \sum_{i=1}^{i=n} h_i \omega_i = 0. \tag{4.7}$$

Finally, the mass conservation equation is satisfied by the following equation,

$$\frac{\partial r}{\partial \chi} = \frac{1}{\rho r^{\alpha}}. \tag{4.8}$$

This equation is otherwise referred to as the mapping equation, used to express the original coordinate r as a function of the mass-based coordinate ψ.

4.1.1. Boundary conditions

The boundary conditions at the surface of the particle are extracted from the species conservation equation, that expresses the balance between convective and diffusive transport on the one hand, and heterogeneous reactions on

the other hand. In (ψ,τ) coordinate system, the resulting Robin boundary conditions read,

$$\dot{M}_w Y_{i,s} - C_\alpha \rho r_0^{2\alpha} \frac{\lambda_w}{C_p} \left.\frac{\partial Y_i}{\partial \chi}\right|_s - \omega_{i,s} = 0. \tag{4.9}$$

Subscript s identifies variables calculated at the surface of the particle. The particle burning rate, directly connected to the mass flow rate at the surface, can be computed as follows,

$$\dot{M}_w = \dot{m}_{c,1} + \dot{m}_{c,2}, \tag{4.10}$$

where $\dot{m}_{c,1}$ and $\dot{m}_{c,2}$ are the char reaction rate due to direct oxidation and gasification, respectively (described in detail in section 4.1.2). Assuming a homogeneous temperature profile in the particle, a Dirichlet boundary condition is used for the gas phase temperature at the particle surface, resulting in,

$$T_s^g = T_p. \tag{4.11}$$

This algebraic equation requires an initial condition for completeness, leading to,

$$\chi\left(r = r_0\right) = 0. \tag{4.12}$$

Satisfying energy conservation in a control volume surrounding the particle surface results in the evolution equation for the particle temperature, given as,

$$M_p C_c \frac{\partial T_p}{\partial \tau} - C_\alpha \rho r_0^{2\alpha} \lambda_w \frac{\partial T}{\partial \chi} - \left(\dot{m}_{c,1} h_{c,1} + \dot{m}_{c,2} h_{c,2}\right) = 0, \tag{4.13}$$

where the enthalpy of the two surface reactions are, $h_1 = \frac{117\times10^3}{W_C} J/kg_C$ and $h_2 = \frac{-172\times10^3}{W_C} J/kg_C$, respectively, as proposed by Tirado *et al.* [63]. M_p represents the particle mass, and C_c the specific heat capacity of char. λ_w is the heat conductivity, determining heat conduction at the surface of the particle. In this study, the particle is assumed to have a homogeneous temperature on the surface and inside, therefore, the only heat conduction is from the gas to the particle, resulting in $\lambda_w = \lambda_g$. Finally, the boundary conditions in the far-field are expressed explicitly as Dirichlet boundary conditions:

$$Y_i\left(\tau, \chi \to \infty\right) = Y_i^\infty, \tag{4.14}$$

$$T\left(\tau, \chi \to \infty\right) = T^\infty. \tag{4.15}$$

For the purpose of this study, the particle is considered to be spherical and α is therefore set to 2.

4.1.2. Chemical models

The above equations are finally closed by selecting a specific kinetic model describing the heterogeneous and homogeneous reactions, resulting in the respective reaction rates, defining ω_i's, $\dot{m}_{c,1}$, and $\dot{m}_{c,2}$.

Heterogeneous reactions

The combustion process on the surface of the particle is approximated by the following heterogeneous reactions (referred to as direct and indirect oxidation, respectively),

$$C\,[s] + \frac{1}{2}O_2 \rightarrow CO,$$

$$C\,[s] + CO_2 \rightarrow 2CO.$$

The reaction rates are expressed as a function of the partial pressure of the gaseous species at the surface, given by;

$$\omega_{c,1} = A_1 P_1^{n_1} \exp\left(\frac{-E_1}{RT_p}\right), \tag{4.16}$$

$$\omega_{c,2} = A_2 P_2^{n_2} \exp\left(\frac{-E_2}{RT_p}\right), \tag{4.17}$$

where $A_1 = 0.095 kg/m^2/s/Pa$, $E_1 = 108 kJ/mol_C$, $A_2 = 7.55 kg/m^2/s/Pa^{0.45}$, $E_2 = 148.5 kJ/mol_C$, $n_1 = 1$, $n_2 = 0.45$, and P_i is the partial pressure of species $i \in \{O_2, CO_2\}$. Detailed descriptions of the parameters can be found in [64]. The reaction rate of other species at the surface can be computed from the char reaction rate by,

$$\omega_{i,s} = X_i \omega_{c,1} + Z_i \omega_{c,2}, \tag{4.18}$$

where,

$$(X_i) = \left(\frac{W_{CO}}{W_C}, -\frac{W_{O_2}}{2W_C}, 0, 0\right),$$

and

$$(Z_i) = \left(\frac{2W_{CO}}{W_C}, 0, -\frac{W_{CO_2}}{W_C}, 0\right).$$

Finally, W_C denotes the molecular weight of carbon and W_{O_2} denotes the molecular weight of oxygen.

Homogeneous reaction

In this study, a single global reaction, oxidation of carbon monoxide, governs the gas phase chemistry,

$$CO + O_2 \rightarrow CO_2.$$

Therefore, the source terms appearing on the right-hand-side of species equation 4.6 are expressed using the reaction rate of the carbon monoxide oxidation reaction, given as,

$$\omega_i = \nu_i \omega_{CO}, \tag{4.19}$$

where ν_i represents the mass-based stoichiometric ratio between the species i and the carbon monoxide. The reaction rate of CO can be modelled, as proposed by Tirado *et al.* [63], by

$$\omega_{CO} = \frac{-K\rho^2 Y_{H_2O}^{0.5}}{W_{CO} W_{O_2}^{0.5} W_{H_2O}^{0.5}} Y_{CO} Y_{O_2}^{0.5} \exp\left(\frac{-E_g}{RT}\right), \tag{4.20}$$

where, $K = 1.23 \times 10^8 sec$, $E_g = 125400\ J/mole_C$, $Y_{H_2O} = 10^{-3}$, and W_i denotes the molecular weight of the ith species. In this study, following the model proposed by Matalon [29], mass fraction of water is assumed to be small, and its variation inside the domain is considered negligible. Further analysis to determine the effect of water on the overall sensitivities will be the subject of future research. Assuming constant thermodynamic parameters, the source term of the energy equation can be defined as follows,

$$\omega \sum W_i h_i^0 \left(\nu_i^{''} - \nu_i^{'}\right) = \omega_{CO_2} \frac{W_{CO}}{W_{CO_2}} H_{CO} + \omega_{CO_2} H_{CO_2}, \tag{4.21}$$

where $H_{CO} = 110.53/W_{CO}\ kJ/kg$ and $H_{CO_2} = 393.474/W_{CO_2}\ kJ/kg$. W_{CO} and W_{CO_2} denote the molecular weight of carbon monoxide and carbon dioxide respectively.

4.2. Gradient computation

Sensitivity is, in effect, the rate of change in a measured quantity of interest (QoI) with respect to a parameter or variable. It is a signed quantity that signifies whether a change in the parameter will lead to an increase or decrease in the value of the QoI and quantifies the magnitude of this change. In this study, the QoI is computed using the governing equations presented in the previous section. In order to extract the sensitivity information, a method

needs to be devised to efficiently compute the gradient (Jacobian) of these governing equations.

Several approaches exist to compute gradients from a system of equations [65]: analytical computation, numerical approximation, etc. As far as numerical techniques are concerned, the most common method is the finite difference approach. This method consists of adding a small perturbation to the parameter with respect to which the sensitivity is being computed. The nonlinear equations are then solved with the perturbed quantity, and the difference between the resulting value and the original (unperturbed) one divided by the perturbation provides a first-order approximation of the gradient. This method quickly becomes too expensive for large systems of nonlinear equations, with multiple parameters of interest, since it commands multiple (potentially unsteady) simulations. In addition, the optimal value of the selected perturbation changes from case to case and parameter to parameter, making it non-trivial and non-robust in practice, where often suboptimal values can lead to large variations in the estimated values of the gradient. An alternative method is the forward sensitivity approach, which is based on the linearization of the governing equations to provide evolution equations for the gradient with respect to a single parameter. The main advantages of the forward sensitivity method are (i) the nonlinear problem needs to be solved once and (ii) the gradient of any quantity of interest with respect to a certain parameter is computed from a linear system of equations, more easily solved than the nonlinear equations. The main disadvantage of this approach, which also renders it impractical for systems with large parameter spaces, is that for each parameter, a separate equation needs to be derived, discretized, and solved numerically. Nonetheless, the forward sensitivity approach is also presented here and will be used to validate a third method for gradient computation, namely the adjoint method. The latter indeed proves superior in the context of this study and will, therefore, be discussed subsequently.

4.2.1. Forward sensitivity

A brief description of the forward sensitivity approach is presented below for a Differential Algebraic Equation given as;

$$\begin{cases} \dfrac{d\boldsymbol{\Phi}^d}{d\tau}\left(\tau\right) = \mathbf{F}^d\left[\tau, \boldsymbol{\Phi}^a\left(\tau\right), \boldsymbol{\Phi}^d\left(\tau\right), \mathbf{p}\right], \\ 0 = \mathbf{F}^a\left[\tau, \boldsymbol{\Phi}^a\left(\tau\right), \boldsymbol{\Phi}^d\left(\tau\right), \mathbf{p}\right] \end{cases} \tag{4.22}$$

where, $\boldsymbol{\Phi} = \left(\boldsymbol{\Phi}^a, \boldsymbol{\Phi}^d\right)$ denotes the dependent variable, also known as the state vector. In the case of unsteady char burnout presented here, the state vector is composed of differential variables $\boldsymbol{\Phi}^d$ (density, species mass fraction and gas phase temperature) on the one hand, and an algebraic variable Φ^a (radial coordinate) on the other hand. $\mathbf{p}$ represents the parameters of interest. The algebraic operator $\mathbf{F}^a$ contains the discretization of the mapping equation. The differential operator $\mathbf{F}^d$ represents the semi-discretization of the transport equations that also includes Robin and Dirichlet boundary conditions, at the particle surface and in the far-field, respectively. In the literature, equation 4.22 is referred to as a Differential Algebraic Equation (DAE) of index-1. It differs from Ordinary Differential Equations (ODE) in that the rate of change of the algebraic variable $\mathbf{u}^a$ does not appear explicitly. For more information regarding the classification of such equations, the reader is referred to [66].

In the context of adjoint-based sensitivity analysis, equation 4.22 is commonly known as the primal or forward problem (in the problem of interest to this study, the forward problem is given by the governing equations described in the previous section). The forward problem can be linearized as follows,

$$\begin{cases} \dfrac{d\boldsymbol{\Phi}_p^d}{d\tau} = \left.\dfrac{\partial \mathbf{F}^d}{\partial \boldsymbol{\Phi}}\right|_{\tau,\mathbf{p}} \boldsymbol{\Phi}_p + \left.\dfrac{\partial \mathbf{F}^d}{\partial p}\right|_{\tau,\boldsymbol{\Phi}}, \\ 0 = \left.\dfrac{\partial \mathbf{F}^a}{\partial \boldsymbol{\Phi}}\right|_{\tau,\mathbf{p}} \boldsymbol{\Phi}_p + \left.\dfrac{\partial \mathbf{F}^a}{\partial \mathbf{p}}\right|_{\tau,\boldsymbol{\Phi}} \end{cases} \tag{4.23}$$

where

$$\boldsymbol{\Phi}_p = \frac{\partial \boldsymbol{\Phi}}{\partial p} \tag{4.24}$$

denotes the sensitivity with respect to p, any given component of $\mathbf{p}$. As it appears, the main drawback of the forward sensitivity approach is that it requires re-deriving the second term on the right hand side of equation 4.23 for each selected parameter p, which becomes a disadvantage for systems with large numbers of parameters. The adjoint method is then more apt to deal with this shortcoming [10], as highlighted in the following section. As the derivation of forward sensitivity equation does not depend on the quantity of interest (QoI), the sensitivity with respect to any QoI can be computed using the initial condition of the following form,

$$\boldsymbol{\Phi}_p(0) = 0. \tag{4.25}$$

Here, only time-integrated QoIs, denoted as G, are considered, leading to

$$G = \int_0^{\mathcal{T}} g\left[\tau, \boldsymbol{\Phi}\left(\tau\right), \mathbf{p}\right] d\tau, \tag{4.26}$$

where, g denotes the instantaneous value of the QoI, and $\mathcal{T}$ the final time horizon. The expression describing the sensitivity is then given, in normalised form, as

$$\frac{dG}{dp} = \frac{\|p\|}{G}\left[\int_0^{\mathcal{T}} \left(\left.\frac{\partial g}{\partial \boldsymbol{\Phi}}\right|_{\tau,\mathbf{p}} \boldsymbol{\Phi}_p + \left.\frac{\partial g}{\partial p}\right|_{\tau,\boldsymbol{\Phi}} \right) d\tau \right]. \tag{4.27}$$

Normalising the extracted sensitivity by the value of the parameter and the QoI, leads to a non-dimensionalized gradient, and allows a fair comparison between sensitivities of various QoIs with respect to different parameters.

4.2.2. Discrete adjoint

This section briefly describes the extraction of discrete adjoint equations, for a DAE of index-1, as represented by equation 4.22 (a detailed description is provided in [66]).

Considering a general QoI, G, the first step to derive the adjoint equation is to construct the Lagrange functional as follows,

$$\begin{aligned} L = G\left(\boldsymbol{\Phi}^a, \boldsymbol{\Phi}^d, \mathbf{p}\right) - \int_0^{\mathcal{T}} \boldsymbol{\eta}^d \cdot \left\{ \frac{d\boldsymbol{\Phi}^d}{d\tau} - \mathbf{F}^d\left[\tau, \boldsymbol{\Phi}^a\left(\tau\right), \boldsymbol{\Phi}^d\left(\tau\right), \mathbf{p}\right] \right\} d\tau \\ + \int_0^{\mathcal{T}} \boldsymbol{\eta}^a \cdot \mathbf{F}^a\left[\tau, \boldsymbol{\Phi}^a\left(\tau\right), \boldsymbol{\Phi}^d\left(\tau\right), \mathbf{p}\right] d\tau, \end{aligned} \tag{4.28}$$

where initial conditions have been omitted for clarity. $G\left(\boldsymbol{\Phi}^a, \boldsymbol{\Phi}^d, \mathbf{p}\right)$ is a general representation for a semi-discrete quantity of interest. $\boldsymbol{\eta}^d$ and $\boldsymbol{\eta}^d$ are the algebraic and differential adjoint variables respectively. In order to extract the adjoint equation, the variation of the Lagrange functional with respect to the state vector $\boldsymbol{\Phi} = \left(\boldsymbol{\Phi}^d, \boldsymbol{\Phi}^a\right)$ is set to zero. The resulting equations are presented in the next sections for special cases of a time-integrated QoI and a local QoI.

Time-integrated quantity of interest

Considering the case of a time-integrated quantity of interest:

$$G = \int_0^{\mathcal{T}} g\left[\tau, \boldsymbol{\Phi}^a\left(\tau\right), \boldsymbol{\Phi}^d\left(\tau\right), \mathbf{p}\right] d\tau. \tag{4.29}$$

Setting the variation of the Lagrange functional (equation 4.28) with respect to the state vector to zero, leads to the following adjoint equations,

$$\frac{d\boldsymbol{\eta}^d}{d\tau} + \left(\frac{\partial \mathbf{F}^d}{\partial \boldsymbol{\Phi}^d}\right)^\dagger \boldsymbol{\eta}^d + \left(\frac{\partial \mathbf{F}^a}{\partial \boldsymbol{\Phi}^d}\right)^\dagger \boldsymbol{\eta}^a = -\frac{\partial g}{\partial \boldsymbol{\Phi}^d}, \tag{4.30}$$

$$\left(\frac{\partial \mathbf{F}^d}{\partial \boldsymbol{\Phi}^a}\right)^\dagger \boldsymbol{\eta}^d + \left(\frac{\partial \mathbf{F}^a}{\partial \boldsymbol{\Phi}^a}\right)^\dagger \boldsymbol{\eta}^a = -\frac{\partial g}{\partial \boldsymbol{\Phi}^a} \tag{4.31}$$

where † denotes the transpose operator. In this case, the initial condition for the adjoint equation is,

$$\boldsymbol{\eta}^d\left(\mathcal{T}\right) = 0. \tag{4.32}$$

As can be deduced from the initial condition, the adjoint equation needs to be integrated backward in time. As a result, this equation is sometimes referred to as the backward problem, as opposed to the forward (primal) problem, which is integrated forward in time. The terms in equations 4.30 & 4.31 include jacobians of $\mathbf{F}^d$, $\mathbf{F}^a$ and g, evaluated using the forward solution, suggesting that the solution of the forward problem is needed at each time step of the backward integration. This solution must either be already stored in memory, or recalculated from the solution at the last stored time step. This procedure is called checkpointing, which is also employed in this study to make the forward solution available in the adjoint integration step. The sensitivity can then be computed by linearizing the discrete version of the Lagrange functional with respect to parameter $\mathbf{p}$, leading to:

$$\frac{dG}{d\mathbf{p}} = \int_0^{\mathcal{T}} \left(\frac{\partial g}{\partial \mathbf{p}} + \boldsymbol{\eta}^d \cdot \frac{\partial \mathbf{F}^d}{\partial \mathbf{p}} + \boldsymbol{\eta}^a \cdot \frac{\partial \mathbf{F}^a}{\partial \mathbf{p}}\right) d\tau. \tag{4.33}$$

The extracted gradient can then be normalised for each parameter, as is done in equation 4.27.

Local quantity of interest

A local (in time) quantity of interest can also be considered as follows:

$$g^\sigma = g\left(\sigma, \boldsymbol{\Phi}^d\left(\sigma\right), \boldsymbol{\Phi}^a\left(\sigma\right), \mathbf{p}\right). \tag{4.34}$$

In the above equation, σ denotes the time instance where the sensitivity is computed. Setting the variation of the Lagrange functional with respect to

the state variable to zero leads to,

$$\frac{d\boldsymbol{\eta}^d}{d\tau} + \left(\frac{\partial \mathbf{F}^d}{\partial \boldsymbol{\Phi}^d}\right)^\dagger \boldsymbol{\eta}^d + \left(\frac{\partial \mathbf{F}^a}{\partial \boldsymbol{\Phi}^d}\right)^\dagger \boldsymbol{\eta}^a = 0, \tag{4.35}$$

$$\left(\frac{\partial \mathbf{F}^d}{\partial \boldsymbol{\Phi}^a}\right)^\dagger \boldsymbol{\eta}^d + \left(\frac{\partial \mathbf{F}^a}{\partial \boldsymbol{\Phi}^a}\right)^\dagger \boldsymbol{\eta}^a = 0. \tag{4.36}$$

It should be noted that, the adjoint equations are not driven by the QoI (the right-hand-sides of both equations are zero). Also, in contrast to the time-integrated quantities, the general expression for the initial condition shows explicit dependence on the QoI as follows,

$$\boldsymbol{\eta}^d(\sigma) = \left.\frac{\partial g}{\partial \boldsymbol{\Phi}^d}\right|_\sigma - \left.\frac{\partial \mathbf{F}^a}{\partial \boldsymbol{\Phi}^d}\right|_\sigma \left(\left.\frac{\partial \mathbf{F}^a}{\partial \boldsymbol{\Phi}^a}\right|_\sigma\right)^{-1} \left.\frac{\partial g}{\partial \boldsymbol{\Phi}^a}\right|_\sigma. \tag{4.37}$$

In the case where the QoI is independent of the algebraic variable, the initial condition (4.37) simplifies to:

$$\boldsymbol{\eta}^d(\sigma) = \left.\frac{\partial g}{\partial \boldsymbol{\Phi}^d}\right|_\sigma. \tag{4.38}$$

Finally, the sensitivity with respect to the parameter $\mathbf{p}$ is given by,

$$\frac{dg^\sigma}{d\mathbf{p}} = \left.\frac{\partial g}{\partial \mathbf{p}}\right|_\sigma + \int_0^\sigma \left(\boldsymbol{\eta}^d \cdot \frac{\partial \mathbf{F}^d}{\partial \mathbf{p}} + \boldsymbol{\eta}^a \cdot \frac{\partial \mathbf{F}^a}{\partial \mathbf{p}}\right) d\tau. \tag{4.39}$$

4.3. Discretization and numerical solution

This section discusses the discretization and subsequent solution of the non-linear, unsteady problem and the related linear sensitivity and adjoint equations. The method of lines is used to transform the algebraic partial differential equations into algebraic ordinary differential equations by discretizing the spatial operators. In order to ensure the stability of the problem, a first-order upwind scheme is used to discretize the convective term, and a central second-order scheme is used to discretize the diffusive and conductive terms. The source terms are treated locally. The spatial dimension is discretized using a regular equidistant mesh. The variables are collocated at the center of their corresponding cell. As previously mentioned, the discretization is performed in the mass-based coordinate (χ, τ), described in equation 4.8. When a quantity needs to be evaluated in physical space, a change of coordinates is performed back into the physical coordinates (r, t). A fully implicit

time integrator (CVODE [67]) is used to advance the equations in time. Forward sensitivity and adjoint equations are discretized in a similar fashion as the equations of the non-linear problem. Due to existing unsteadiness, the linearized equations depend on the values of the unsteady state variables, and a checkpointing algorithm is required. The pseudo-spatial (mass-based) grids for forward sensitivity and adjoint problems are kept identical to the ones used for the non-linear problem. However, interpolation within the time steps of the time integrator is still required. The time steps are chosen small enough to minimize the error due to interpolation between checkpoints. In the mass-based coordinate system, the species, temperature, and density profiles are initialized as constants. The last variable, r which is the spatial coordinate in the physical space, is initialized to satisfy the mapping equation 4.8. This is achieved by the following closed-form solution

$$r_i = \sqrt[\alpha+1]{r_{i-1}^{\alpha+1} + (\alpha+1)\,\frac{\Delta\chi_{i-1}}{\rho_i}}. \tag{4.40}$$

The initial condition for the differential adjoint variables $\boldsymbol{\eta}^d$ are discussed in section 4.2.2. An initial value also needs to be prescribed for the algebraic adjoint variables $\boldsymbol{\eta}^a$, which is done as follows,

$$\boldsymbol{\eta}^a = \left(\frac{\partial g}{\partial \boldsymbol{\Phi}^a} - \boldsymbol{\eta}^d \cdot \frac{\partial \mathbf{F}^d}{\partial \boldsymbol{\Phi}^a}\right)\left(\frac{\partial \mathbf{F}^a}{\partial \boldsymbol{\Phi}^a}\right)^{-1}. \tag{4.41}$$

The resulting discretized equations are implemented using a recently developed language, Julia [68], targeted at scientific computing applications. Julia leverages state-of-the-art compiler technologies to deliver performance comparable to traditional statically-typed languages while guaranteeing the productivity expected from dynamic languages.

4.4. Results and Validation

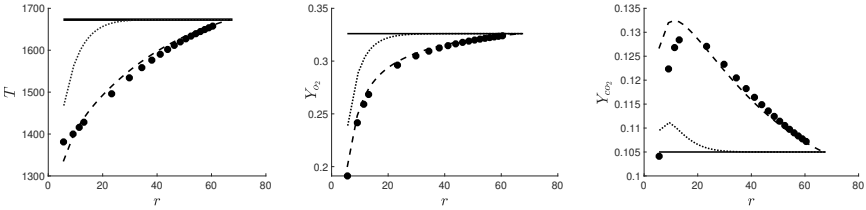
The results are presented for two different environments, as illustrated in Table 4.1. The oxy-fuel environment, particularly in oxyfuel combustion, is of interest as one of viable methods to reduce CO_2 emissions [53]. In an oxy environment, air is replaced by pure oxygen O_2 or a mixture of oxygen with recycled flue gas, generating high CO_2 concentrations and causing the combustion process to change significantly. The composition of both environments is shown in Table 4.1, which closely matches the experimental condition of the flat flame burner of Schiemann *et al.* [30], later simulated by Farazi *et al.* [4].

Test case	Diluent	$Y_{O_2}^{\infty}$	Y_{CO}^{∞}	$Y_{CO_2}^{\infty}$	$Y_{N_2}^{\infty}$
Air atmosphere	N_2	0.326	0.0	0.105	0.569
Oxy atmosphere	CO_2	0.262	0.0	0.738	0.0

Table 4.1.: Compositions defining air and oxy atmospheres in this study.

4.4.1. Forward (primal) problem

In this section, the results of the primal problem are presented and compared between air and oxy atmospheres. The pressure P is set to $10^5 Pa$, and the far-field temperature T^{∞} is 1673 K. The initial particle radius is set to $r_0 = 60 \times 10^{-6}$ m. It should be noted that devolatilisation is not accounted for in this study. As a result, the initial particle temperature is assumed to be $T_p^0 = 1200K$. Figure 4.1 shows the variation of temperature and relevant mass fractions, from their initial to final distributions, for air atmosphere. In order to better illustrate the initial variation of selected QoIs in this study (for example, burning rate, discussed later in this section), time variable t is transformed to $t^* = \ln(t/\Delta t)$, where $\Delta t = 1.25 \times 10^{-11} s$. Initially, due to the transfer of heat from the surrounding hot gas to the cooler particle, the gas temperature in the particle vicinity (r $10mm$) starts to decrease, as shown in figure 4.1a. As time evolves, the difference between particle and gas phase temperatures decreases. Finally, the heat released by the system is not completely absorbed by the particle, leading to an increase in the gas phase temperature close to the particle surface. This behaviour can be better observed by comparing the temperature distributions at $t^* = 22.14$ and $t^* = 27$. Due to the presence of heterogeneous reactions on the surface (char oxidation reaction, in particular), oxygen mass fraction reduces close to the particle surface, as illustrated in figure 4.1b. Carbon dioxide mass fraction, on the other hand, increases initially close to the particle surface, and after reaching a peak, decreases to the far-field value (figure 4.1c). The peak in carbon dioxide mass fraction, as a product of the gas phase reaction, gives and indication of the flame position in the gas phase. Carbon dioxide is consumed by the char reaction, leading to the decrease of its mass fraction value close to the particle surface. While analysing the evolution of certain quantities in the spatial domain can be informative, investigating the changes in quantities such as particle surface temperature and burning rate, measurable in both experiments and simulations, are more relevant to this study. Figure 4.2 shows



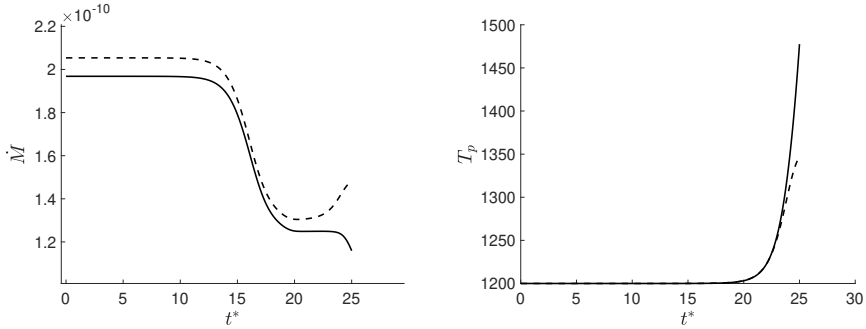
(a) Gas phase temperature **(b)** Y_{O_2} **(c)** Y_{CO_2}

Figure 4.1.: Evolution of spatial distribution of temperature, oxygen mass fraction (Y_{O_2}), and carbon dioxide mass fraction (Y_{CO_2}) in the spatial domain, for air atmosphere: —, ($t^* = 10^{-10}$); $\cdots$, ($t^* = 18.85$); $- - -$, ($t^* = 22.14$); •, ($t^* = 27$).

the evolution of the particle temperature and its burning rate $\dot{M} = \dot{M}_w r_0^3$ for air and oxy atmospheres. Since the interest of this study lies in analysing the transient behaviour of the problem, the simulations are stopped when the ratio of the burnt coal M_b/M_0 reaches 5.3%. Here, M_b is the burnt mass of the particle, and M_0 is the initial mass of the particle. This time-frame ensures that the problem does not reach a steady state. In chapter 6 the simulation run time will be longer.

Burning rate is an important QoI, since it expresses the consumption rate of the particle and sets the value of the Stefan flow velocity. In both cases, three distinct regions can be identified as far as the burning rate is concerned: (i) the short time behaviour, where the burning rate remains relatively constant, followed by (ii) the intermediate time behaviour where the burning rate reduces, reaching a plateau, and finally, (iii) the long time behaviour where the burning rate increases in the oxy atmosphere and continues to decrease in the air atmosphere. This change in the long time behaviour is similar to the trends were observed in two-dimensional unsteady simulations of Farazi *et al.* [4]. As far as the short time behaviour of the burning rate is considered, the oxy atmosphere leads to higher burning rates compared to air, a trend that persists in time. It should however be noted that these results are valid for cases where the initial devolatilisation process can be ignored.

Considering the variation in the particle surface temperature, it can be noted that, initially, due to weaker heterogeneous reactions on the particle surface (low reaction rates), particle temperature increases slightly (this variation is not visible in the profiles of figure 4.2b). At this stage, the particle is heated mainly through heat conduction between the hot gas and the cooler



(a) Burning rate **(b)** Particle temperature

Figure 4.2.: Evolution of particle temperature and burning rate in time: ——, air; − − −, oxy atmosphere.

particle. However, as the simulation advances and reaches the long time behaviour, particle temperature rapidly increases, as both heterogeneous and homogeneous reactions become stronger. Comparing the two atmospheres, the heating rate for the particle in air is higher than in oxy atmosphere.

Particle temperature and burning rate will be used in the following section as quantities of interest, and help identify sensitivities with respect to model/physical parameters.

4.4.2. Sensitivities of unsteady char combustion

In this section, the sensitivities computed with the adjoint method (section 4.2.2) are compared to those computed using the forward sensitivity method.

Cross-validation of adjoint and forward sensitivity

In this section, the sensitivities computed using the adjoint and forward sensitivity methods are compared and analyzed. Due to the unsteady nature of the problem, the objective function (quantity of interest), G, is defined as a time-integrated quantity (see section 4.2.2). Therefore, before extracting the resulting sensitivities, the time horizon for integration $\mathcal{T}$ needs to be defined. Figure 4.3 compares the sensitivities extracted using discrete adjoint and forward sensitivity techniques for $\mathcal{T} = t^* = 22.9$. Here, the particle

temperature is selected as the quantity of interest, leading to the following definition of the objective function:

$$G = \int_0^{\mathcal{T}} T_p \, dt. \tag{4.42}$$

Figure 4.2a shows that, within this time horizon, the system demonstrates an intermediate time behavior, where the burning rate is time-dependent (in the following section, the dependence of sensitivities on the selected time horizon is further analyzed). Figure 4.3 shows a good agreement between the extracted sensitivities through the forward sensitivity and the discrete adjoint techniques. The thermal conductivity λ_g exhibits a physical range of values within 0.01 to 0.12 W/mK for the given configuration, considering T_g in the interval $[350, 1600]$ K and $P = 1$ bar. To showcase the reliability and robustness of the adjoint approach, we specifically examine the sensitivity concerning $\lambda_g = 0.4$ for extrapolated values at exceptionally high temperatures. Further analysis demonstrates that this agreement holds regardless of the selected time horizon or parameter of interest. Therefore, in the following section, only the discrete adjoint method is used to compute the sensitivities.

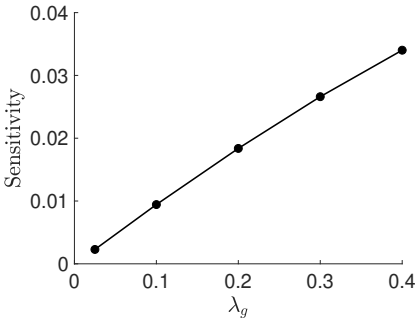


Figure 4.3.: Sensitivity of particle surface temperature, T_p, with respect to gas conductivity (λ_g):—, discrete adjoint; •, forward sensitivity.

Time variable sensitivities

Since the burning rate is the most relevant QoI to this study, the evolution of parameter sensitivities is first extracted for the burning rate. Therefore, the

QoI is formally defined as:

$$G = \int_0^{\mathcal{T}} \dot{M}_w \, dt. \tag{4.43}$$

Figure 4.4 compares the sensitivities extracted in both air and oxy atmospheres, and the burning rate has reached a plateau, as illustrated by Figure 4.2a. In Figure 4.4, the focus has been placed on the heterogeneous and homogeneous kinetic model parameters (such as activation energies and pre-exponential factors). Sensitivity with respect to the heat conductivity of the gas phase λ_g is also computed, as it governs the heat conduction from the gas to the particle and directly affects the burning rate (see section 4.1). Figure 4.4 shows that, regardless of the free-stream composition, the sensitivity of burning rate to the parameters of the homogeneous reaction is smaller than those of the heterogeneous reactions. This result can change if more complex models are considered. As far as the heterogeneous reactions are concerned, the char oxidation reaction seems to be the most dominant. In both free-stream compositions, the burning rate shows higher sensitivities with respect to the parameters of the oxidation reaction, and in particular, the activation energy, which shows the highest sensitivity in both cases. When comparing the results of the two atmospheres, air seems to result in higher sensitivities than an oxy atmosphere, due to the higher heating rate of char in air. These results are, however, extracted for a selected time horizon. Therefore, it would be of interest to investigate the evolution of these sensitivities as the time horizon is varied. In order to extract time-varying sensitivities, term $\mathcal{T}$ in Equation 4.43 is varied, and sensitivities are extracted for discrete time intervals. The results are shown in Figure 4.5, and are compared for the two free-stream compositions. Judging by the result of Figure 4.4, showing the final distribution of the overall sensitivities at $t^* = 22.9$, the burning rate is expected to show the highest sensitivities with respect to the parameters of the oxidation reaction, confirmed by the results of Figure 4.5. This figure also shows that all parameter sensitivities are initially constant, following the same behavior as the burning rate for short time horizons, as shown in Figure 4.2a. For longer time horizons, while the decrease in burning rate influences the sensitivities of some of the parameters, the sensitivities of the dominant parameters seem to be unaffected. As the time horizon does not affect the sensitivities extracted for the most dominant parameters, the short time behavior can be used as a surrogate for the overall sensitivity distribution. Comparison of Figures 4.5a and 4.5b suggests that the free-stream species composition $\{Y^\infty_{CO}, Y^\infty_{CO_2}, Y^\infty_{O_2}, Y^\infty_{N_2}\}$ does not affect model sensitivities

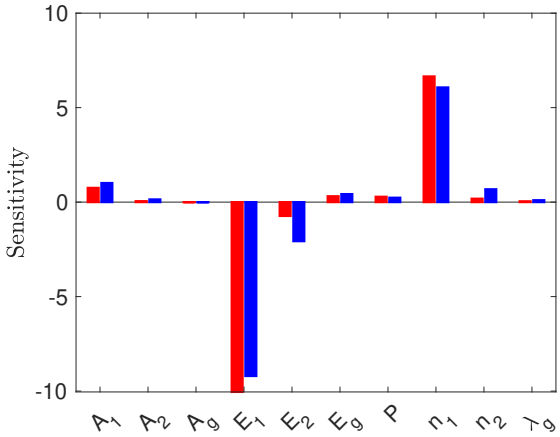
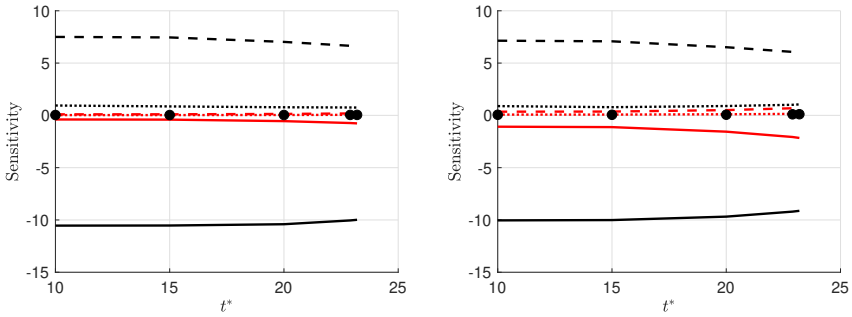


Figure 4.4.: Sensitivities extracted for burning rate with respect to kinetic model parameters at $t^* = 22.9$. (red), air; (blue), oxy atmosphere.

measured by choosing burning rate as QoI. The negligible effect of free-stream composition on burning rate sensitivities can be attributed to a slower diffusion time scale, which compared to the selected time horizon $\mathcal{T}^*$ leads to insufficient time for the effect of the free stream to propagate to the surface of the particle. To examine the effect of the choice of the QoI on the extracted sensitivities, a configuration similar to the one examined in Figure 4.4 is selected. Sensitivities are, however, extracted with respect to particle surface temperature, as presented in Equation 4.42. The results are shown in Figure 4.6. This figure demonstrates that the choice of the QoI affects the distribution of sensitivities for both free-stream compositions. While the most sensitive parameters remain the parameters of the direct oxidation reaction, as was the case for the burning rate, the most dominant parameter is now the pre-exponential factor with the activation energy following closely. The parameters of the second heterogeneous reaction show relatively higher sensitivities, as far as the prediction of the particle temperature is concerned. Comparing Figures 4.4 and 4.6 also shows overall higher sensitivities for burning rate than particle surface temperature, suggesting that uncertainties in the value of these parameters would result in higher discrepancies in the burning rate prediction, rather than particle temperature. It is important to note that, in this sensitivity analysis, the particle surface temperature (T_p) is considered



(a) Air atmosphere **(b)** Oxy atmosphere

Figure 4.5.: Evolution of sensitivities, extracted for burning rate, $\dot{M}$, as QoI, for air and oxy atmospheres: ——, E_2; − − −, n_2; $\cdots$, A_2; ——, E_1; − − −, n_1; $\cdots$, A_1; •, λ_g.

as a QoI. This is in contrast to the previous chapters [2,3], where the particle surface temperature was treated as a model parameter and not a part of the primal problem solution. In order to determine whether this behavior is independent of the selected time horizon, the evolution of sensitivities needs to be extracted as a function of time.

Figure 4.7 shows the evolution of the particle temperature sensitivities with respect to the heterogeneous reaction parameters. The evolution of sensitivities is entirely different from what was observed in Figure 4.5. This change is due to the different behaviors of the two quantities of interest, as illustrated in Figure 4.2. While the burning rate is initially constant and then decreases, the particle temperature monotonically increases, with an abrupt increase at the end of the considered time horizon. The sensitivities of the particle temperature follow a similar trend. The parameters of the direct oxidation reaction remain the most sensitive with the pre-exponential factor dominating the sensitivities of the particle temperature. Comparing the particle temperature sensitivities extracted in the two environments shows that air yields slightly higher values as far as the pre-exponential factor is concerned.

Regardless of the free-stream composition and the time horizon, selecting the burning rate as the quantity of interest leads to larger values in parameter sensitivities compared to the particle temperature, suggesting the burning rate to be the more relevant choice of QoI for this problem. This is expected,

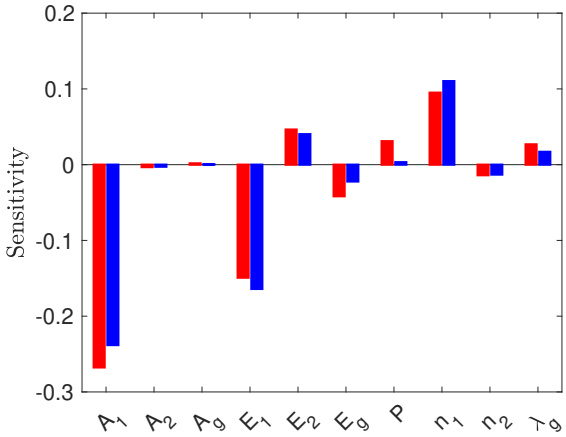
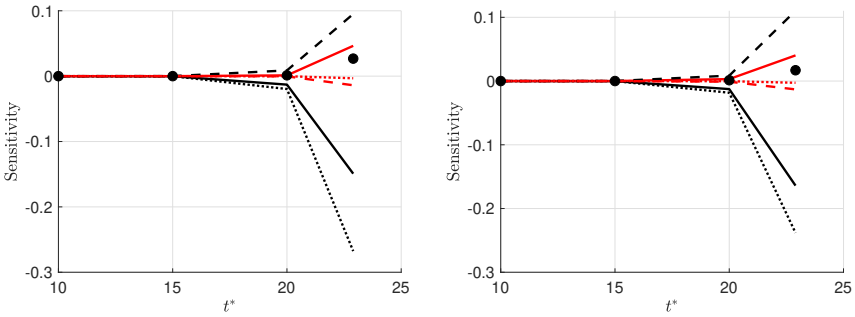


Figure 4.6.: Sensitivities extracted for particle temperature T_p with respect to kinetic model parameters at $t^* = 22.9$. (red), air; (blue) oxy atmosphere.

since the value of the Stephan flow velocity on the surface of the particle governs the dynamics of the underlying system.

Finally, sensitivities with respect to physical conditions of the system are extracted. Here, free stream mass fractions are chosen as the parameters of interest, since when determining surface model parameters experimentally, curves are fitted considering these quantities. High sensitivities with respect to free steam conditions can lead to inaccuracy in the determination of model coefficients. Earlier, the burning rate was established as the most relevant quantity of interest to this problem. As a result, these sensitivities are reported only for the burning rate. They are shown in Figure 4.8 where they are compared for the two free-stream compositions. In contrast to the sensitivities with respect to model parameters (Figure 4.5), the sensitivities with respect to free stream mass fractions show more dependence on the selected time horizon. However, the resulting non-dimensionalized sensitivities are considerably lower than those extracted with respect to kinetic model parameters. Comparing the sensitivities of the two free stream compositions shows that, since the problem is diffusion-controlled, the diluting species (N_2 for air and CO_2 for an oxy atmosphere), play an important role and results in the highest sensitivities. This is followed by sensitivities in oxygen mass fraction in both free stream compositions, as oxygen consumption is



(a) Air atmosphere **(b)** Oxy atmosphere

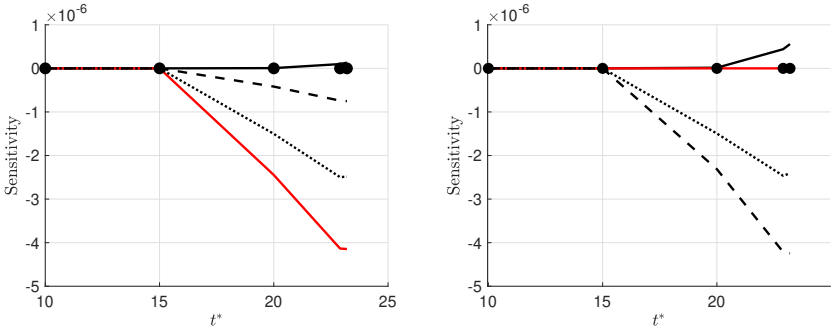
Figure 4.7.: Evolution of sensitivities, extracted for particle temperature, T_p, as QoI, for air and oxy atmospheres at $t^* = 22.9$: ——, E_2; − − −, n_2; ⋯, A_2; ——, E_1; − − −, n_1; ⋯, A_1; •, λ_g.

an exothermic reaction of char oxidation and contributes the most to the burning rate. Carbon monoxide shows a minimum sensitivity in both air and oxy atmospheres, due to the weak gasification reactions on the surface and in the gas phase.

4.5. Summary and Conclusions

In conclusion, while interpreting the results presented in this chapter, the following points need to be considered. Firstly, working within the perimeter of the kinetic models chosen in this study, the extracted sensitivities are directly dependent on the accuracy of the predicted solution, as measured and identified from the model. This does not guarantee that these sensitivities match experimental observations. The differences, however, motivate the use of more sophisticated models in their stead. Secondly, the extracted sensitivities are directly dependent on the choice of QoI. While one QoI might lead to high sensitivities with respect to a model parameter or physical composition of the problem, another QoI might show no sensitivities at all. Therefore, if the QoI is not chosen correctly, it might have misleading consequences in the interpretation of the extracted sensitivities.

To overcome these obstacles, in the next chapters of this study, I will focus on sophisticated gas-phase combustion models (Chapter 5) to address in detail the effect of the gas-phase flame on solid fuel combustion processes



(a) Air atmosphere **(b)** Oxy atmosphere

Figure 4.8.: Evolution of free stream sensitivities, extracted for burning rate, $\dot{M}$, as QoI, for air and oxy atmospheres: —, $N_2{}^{\infty}$; —, T^{∞}; − − −, $CO_2{}^{\infty}$; $\cdots$, $O_2{}^{\infty}$; •, CO^{∞}.

such as devolatilization and pyrolysis, which will be discussed in Chapter 6. Moreover, as shown in Figure 4.3, the sensitivity evolution with respect to the parameter value is not constant. Thus, it is a valid question to consider: How would the behavior of the model parameters' sensitivities change with the parameter value? To answer this question, uncertainty quantifications will be included, as they provide global sensitivity analysis for the variation in the model parameter value.

5

Uncertainty quantification of kinetic models using adjoint-driven active subspace algorithms

In this chapter, the primary focus is on gas phase kinetics rather than surface kinetics and char combustion. The aim is to improve the homogeneous combustion model in reactive solid fuel simulations, which relies on a large number of parameters. To address this issue, the active subspace method (ASM) is employed. ASM is a dimensionality reduction technique used to identify the dominant directions in the objective function space. This allows the construction of a reduced model with fewer parameters than the original model, enabling more efficient computation of the specified Quantity of Interest (QoI). An adjoint-based algorithm is also implemented to provide low-cost access to gradient information required for dimensionality reduction. Using this approach, the uncertainties of ignition delay time (IDT) with respect to reaction rate are quantified in an isobaric zero-dimensional reactor in an efficient and cost-effective manner. The global sensitivity analysis of IDT is also extracted to identify the dominant reactions pathway. Furthermore, the PDF of IDT based on the predictions of the active subspace method is compared to the PDF based on linear approximation using the adjoint model (LAAM). Depending on the case, a satisfactory estimation is achieved at a fraction of the cost. Finally, the limitations of the linear approach (LAAM) in cases with strong nonlinearities are highlighted.

5.1. Methodology

In this section, the algorithms for extracting the uncertainties and the relevant gradient information from the system of interest are briefly presented. The objective function of interest to this work is the ignition delay time (IDT), which is defined as the moment where the gradient of temperature reaches its maximal value,

$$\mathrm{IDT} = \underset{t_0 \leq t \leq t_f}{\arg\max}\, \dot{T}\left(t\right) \tag{5.1}$$

where t_0 and t_f denote the initial and final times. The system of interest is composed of an isochoric adiabatic gas inside the reactor. The composition and temperature of this gas evolve in a zero spatial-dimensional and only time-dependent system according to

$$\begin{cases} \dfrac{\partial Y_i}{\partial t} = \dfrac{1}{\rho}\dot{\omega}_i \\ \dfrac{\partial T}{\partial t} = \dfrac{1}{\rho C_v}\dot{\omega}_T \end{cases} \tag{5.2}$$

where (Y_i) $(i \in [\![1, N_s]\!])$ denote the species mass fractions, and C_v and ρ the mixture's average heat capacity at constant volume and density, respectively. The terms $(\dot{\omega}_i)$ denote the species' rates of consumption or production, which are related to the reaction rates,

$$K_j = A_j T^{b_j} \exp\left(\frac{-E_j}{\mathrm{R}T}\right), \tag{5.3}$$

where $j = [\![1, N_r]\!]$. N_r denotes the mechanism's number of reactions, and (A_j), (b_j), and (E_j) the Arrhenius coefficients parameterizing reaction j. The source term $\dot{\omega}_T$ is the heat release rate given by

$$\dot{\omega}_T = -\sum_{i=1}^{N_s} \dot{\omega}_i u_i, \tag{5.4}$$

where u_i denotes the internal energy of species i.

5.1.1. Adjoint Method

The adjoint method performs the computation of the gradient of output functionals (real-valued quantities of interest) at a cost comparable to a single function evaluation, regardless of the number of components (parameters of the model) [10]. While efficient, the adjoint method offers less flexibility than forward sensitivity methods, such as the finite difference method, to tackle implicit functions such as Eq. 5.1. As a consequence, the following alternative objective function, proposed by [25], is employed,

$$\mathcal{J} \equiv \mathrm{IDT} = \frac{1}{2t_f} \int_0^{t_f} \left(T\left(t\right) - T_s\left(t\right)\right)^2 dt. \tag{5.5}$$

where t_f is the final time, T_s the shifted temperature profile, and $t_s = -t_r \times 10^{-2}$[25] the shifting time, proportional to the reaction characteristic time t_r, defined as,

$$t_r = \left[\max\left(\frac{\partial T}{\partial t}\right)\right]^{-1} \left(T_f - T_0\right). \tag{5.6}$$

Forming the Lagrange multiplier [25], the adjoint equations can be extracted, resulting in $\forall i \in [\![1, N_s]\!]$

$$\begin{aligned} -\frac{d\xi_i}{dt} &= \frac{\partial J}{\partial Y_i} + \xi_j \frac{\partial}{\partial Y_i}\left(\frac{1}{\rho}\dot{\omega}_j\right) + \phi \frac{\partial}{\partial Y_i}\left(\frac{1}{\rho C_v}\dot{\omega}_T\right), \\ -\frac{\partial \phi}{\partial t} &= \frac{\partial J}{\partial T} + \phi \frac{\partial}{\partial T}\left(\frac{\dot{\omega}_T}{\rho C_v}\right) + \xi_i \frac{\partial}{\partial Y_i}\left(\frac{\dot{\omega}_i}{\rho}\right) \end{aligned} \tag{5.7}$$

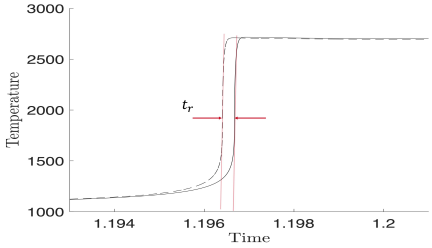


Fig. 5.1.: Comparison between reference and shifted temperature profiles: ——, reference; – – –, shifted.

where ξ_i is the adjoint variable corresponding to the Y_i equation and ϕ to the temperature equation (details regarding the extraction of the adjoint equations are provided in [25]). In the latter equations, J is the integrand already included in the definition of $\mathcal{J}$, namely

$$J \equiv \frac{1}{2t_f} \left(T - T_s\right)^2 . \tag{5.8}$$

The adjoint equations are integrated backward in time from the following conditions,

$$\begin{cases} \xi_i \left(t_f\right) = 0, & \forall i \in [\![1, N_s]\!] , \\ \phi \left(t_f\right) = 0. \end{cases} \tag{5.9}$$

The component of gradient associated with a parameter g is then given as

$$\frac{d\mathcal{J}}{dg} = \int_{t_0}^{t_f} \left[\frac{\partial J}{\partial g} + \xi_j \frac{\partial}{\partial g} \left(\frac{\dot{\omega}_j}{\rho} \right) + \phi \frac{\partial}{\partial g} \left(\frac{\dot{\omega}_T}{\rho C_v} \right) \right] dt. \tag{5.10}$$

Here, g may denote a kinetics parameter (such as a given A_i, $i \in [\![1, N_s]\!]$), a thermodynamics coefficient, or a component of the initial condition. The linearization of the primal source terms ($\dot{\omega}_i$, $\dot{\omega}_T$, etc.) and objective ($\mathcal{J}$) are performed using automatic differentiation [69]. The primal and adjoint equations are implemented in the open-source package `Apophis.jl`. The comparison of the extracted sensitivities (gradient components) using automatic differentiation (AD), and complex step differentiation (CSD), an alternative method for extracting accurate gradients (for more information regarding CSD refer to [70]), are compared in Fig. 5.2 for *GRI* 3.0 mechanism [25].

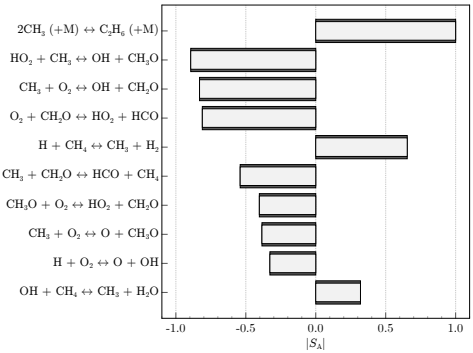


Fig. 5.2.: Sensitivity analysis of ignition delay time with respect to A for the ten most dominant reactions using AD (light gray) and CSD (dark gray) for *GRI* 3.0 mechanism.

The agreement between the two approaches validates the adjoint method in extracting sensitivities, independent of the size of the mechanism considered. The sensitivities are non-dimensionalized as,

$$S = \frac{d\mathcal{J}}{dg}\frac{g}{\mathcal{J}}, \tag{5.11}$$

and normalized by the maximum absolute value of S. For this analysis, the initial mass fractions are $Y_{CH_4} = 0.05$, $Y_{O_2} = 0.2$, and $Y_{N_2} = 0.75$. The initial temperature is set at $T = 1000\,K$ in atmospheric pressure as stated in [25]. The extracted sensitivities agree well and confirm that the reaction $2CH_3(+M) \Rightarrow C_2H_6(+M)$ dominates the ignition process, as far as the Arrhenius parameters are concerned. These results are consistent with those reported in the literature [25].

5.1.2. Active Subspace Method (ASM)

This section highlights how the aforementioned adjoint-based sensitivity computation is leveraged to perform uncertainty quantification of IDT with respect to the parameters of interest (kinetics, thermodynamics, initial conditions) using the active subspace methodology [40].

The dimension of the parameter space is denoted as $\mathbf{D}$, and the random input variables as $\mathbf{x} = (x_1, \cdots, x_D)$. The distribution of x_j $(j \in [\![1, \mathbf{D}]\!])$ is normalized and centered, which may be assumed to be lognormal, uniform, etc. for each parameter. The QoI will be denoted by f. The number of samples M is proportional to the number of dimensions of the input space $\mathbf{D}$ and a factor

η. The active subspace methodology aims to construct an R-dimensional subspace of the $\mathbf{D}$-dimensional parameter space ($\mathbf{R} \ll \mathbf{D}$) that describes most of the variation of the quantity of interest f. The low-dimensional approximation of f is

$$f(\mathbf{x}) \approx G(\mathbf{y}), \quad \mathbf{y} = \mathbf{S}^\top \mathbf{x} \tag{5.12}$$

where $G(\mathbf{y})$ is the response surface, $\mathbf{y} \in \mathbb{K}^R$, $\mathbf{x} \in \mathbb{K}^D$, and $\mathbf{S}$ is an orthogonal matrix ($\mathbb{K} = \mathbb{R}$ or $\mathbb{C}$). The active subspace is then defined as span $(\mathbf{S})$. One way to identify the active subspace is to perform an eigenvalue decomposition of the expectation matrix $\mathbf{C}$ defined as,

$$\mathbf{C} = \frac{1}{M} \sum_{i=1}^{M} \left(\frac{df}{d\mathbf{x}_i} \right) \left(\frac{df}{d\mathbf{x}_i} \right)^\top = \mathbf{W} \boldsymbol{\Lambda} \mathbf{W}^\top \tag{5.13}$$

where M denotes the number of samples, $\mathbf{W}$ and $\boldsymbol{\Lambda}$ are the eigenvalues and eigenvectors. Selecting the first $\mathbf{R}$ eigenvectors of this decomposition selects the $\mathbf{R}$ most dominant directions of the parameter space and provides an approximation of $\mathbf{S} \equiv [\mathbf{w}_1, \cdots, \mathbf{w}_R]$. The motivation for computing the gradients of f at each sample $\mathbf{x}_i$ ($i \in [\![1, M]\!]$) using the adjoint method stems from the fact that it results in the computation of $\mathbf{C}$ scaling as $\ln(\mathbf{D})$ as opposed to $\mathbf{D} \ln(\mathbf{D})$ using finite differences.

The error in the estimated eigenvalues and eigenvectors due to an insufficient number of runs can be estimated with bootstrapping. Bootstrapping is a robust statistical method for estimating the sampling distribution of a statistic without making assumptions about the population distribution. It involves repeatedly resampling with replacement from the observed data to generate multiple datasets of the same size as the original [38, 40]. Once the active subspace is identified, various methods, including polynomial fitting, Polynomial Chaos Expansion (PCE) [32, 71], and High Dimensional Model Representation (HDMR) [37], can be employed to construct the response surface. Here a multi-dimensional least-square method is used. A brief summary of the major steps is presented in Tab. 5.1.

5.1.3. Linear Approximation using the Adjoint Method (LAAM)

Linear approximation using the adjoint method (LAAM) is proposed here as a low-cost alternative to the active subspace method and is based on linearly approximating the QoI with respect to its input parameter space [72]. While very efficient, it should be noted that for functions with a high degree of

Table 5.1.: Response surface construction algorithm.

1	Choose the appropriate distribution for input variables
2	Assemble M random points of the input space, where $M = \eta \ln(\mathbf{D})$
3	Use the adjoint-based method to compute the expectation matrix $\mathbf{C}$ (Eq. 5.13)
4	Apply eigenvalue decomposition to matrix C and choose the dominant eigenvalues and eigenvectors
5	Estimate upper and lower bounds for the eigenvalues with bootstrapping (vary M and repeat 3 and 4)
6	Construct the mapping matrix $\mathbf{S}$ from the dominant eigenvectors and compute the new variable $\mathbf{y} = \mathbf{S}^\top \mathbf{x}$
7	Construct the response surface $G(\mathbf{y}) \approx f(\mathbf{x})$ based on the number of active dimensions

non-linearity with respect to the parameter space, this assumption becomes inefficient; an example of this is discussed in Sec. 5.2.3. The expansion is performed around the mean of the collected samples, denoted $\overline{\mathbf{x}}$ (the center of mass), and expressed as

$$QoI(\mathbf{x}) \equiv f_{LAAM}(\mathbf{x}) \approx QoI(\overline{\mathbf{x}}) + \left.\frac{dQoI}{d\mathbf{x}}\right|_{\overline{\mathbf{x}}} (\mathbf{x} - \overline{\mathbf{x}}). \tag{5.14}$$

Focusing on ignition delay time ($QoI = IDT$), the gradient computation is performed using

$$\forall j \in [\![1, N_r]\!], \quad \left.\frac{dIDT}{dx_j}\right|_{\overline{\mathbf{x}}} = \left.\frac{d\mathcal{J}}{dA_j}\right|_{\overline{\mathbf{x}}} A_j(\overline{x}_j) \frac{\ln(UF_j)}{3} \frac{IDT}{\mathcal{J}} \left(\frac{t_r}{IDT}\right)^3 \tag{5.15}$$

where $\mathcal{J}$ and t_r are defined in Eqs. 5.5 and 5.6, and $\left(\frac{t_r}{IDT}\right)^3$ is a normalization factor due to the difference between $\mathcal{J}$ and f. The main advantage of LAAM is that it can provide a good approximation of the uncertainties with only a single function evaluation, regardless of the size of the system. This huge reduction in computational cost allows rapid analysis of large mechanisms, which will be highlighted in Sec. 5.2.

5.2. Results

In this section, the system uncertainties are first extracted using ASM and LAAM for a range of mechanisms using a single active dimension. A case is then presented where a single dominant direction does not emerge from the eigenmode expansion, motivating the development of a surface reconstruction that relies on a higher-dimensional subspace. Finally, uncertainties with respect to initial conditions are considered to highlight the limitations of the LAAM approach.

5.2.1. One-dimensional subspace

ASM is used here to construct a response surface for kinetic model parameters. The number of dimensions represents the number of variables on which the solution of the objective functions depends. Here, the number of dimensions is equal to the number of reaction rates in the kinetic gas mechanism. The dimensions of the response surface represent the new number of variables on which the objective function depends.

Due to comparatively large available data on a hydrogen mechanism ($h2vb$), specifically uncertainty factors and distribution, this mechanism is first employed to benchmark the presented methodologies. Assuming constant temperature, the uncertainties with respect to the reaction rates are mainly attributed to the pre-exponential factors, (A_j), $j \in [\![1, N_r]\!]$ [73]. Following documented studies [45], the random variables (A_j) are assumed to follow a lognormal distribution,

$$\ln(A_j) \sim \mathcal{N}\left\{\ln\left(A_j^0\right), \left[\frac{1}{3}\ln(UF_j)\right]^2\right\}, \tag{5.16}$$

which are centered and normalized as

$$x_j = \left(\frac{1}{3}\ln(UF_j)\right)^{-1} \ln\left(\frac{A_j}{A_j^0}\right) \sim \mathcal{N}(0,1) \tag{5.17}$$

where A_j^0 is the mean value of the parameter (the value originally stated by the mechanism) and UF_j is the temperature-independent Uncertainty Factor [74]. The number of input parameters x_i is dependent on the number of elemental reactions. The initial conditions are $Y_{H_2} = 0.29$, $Y_{O_2} = 0.15$, $Y_{N_2} = 0.56$, $T_0 = 1000\,K$, and $P_0 = 1.59 \times 10^5\,Pa$. Using the normal distribution (Eq. 5.17), M samples are selected, and the value of IDT ($f(\mathbf{x})$) is computed. The gradients are evaluated using the adjoint methodology with J (Eq. 5.5) as QoI. The extracted gradients are then normalized as

$$\frac{df}{dx_j} = \frac{A_j f}{3\mathcal{J}} \frac{d\mathcal{J}}{dA_j} \ln UF_j. \tag{5.18}$$

As highlighted in Tab. 5.1, the matrix $\mathbf{C}$ is then constructed, and an eigenvalue decomposition is performed to identify the eigenvalues and vectors before performing bootstrapping to estimate the error bounds. In this particular case, $M = 65$ ($\eta = 50$ and $N_{boot} = 50$) suffices to identify the active direction. There is a difference of about four orders of magnitude between the first and

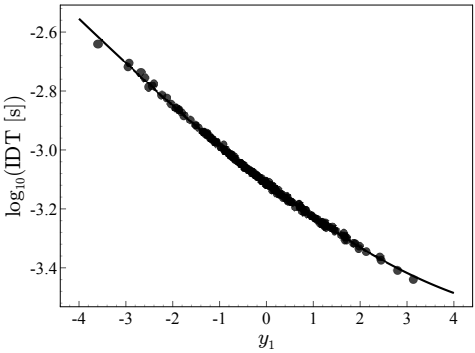


Fig. 5.3.: Comparison of the response surface fitted against a single active direction: •, samples; ——, third-degree polynomial fit.

second eigenvalue ($\lambda_1/\lambda_2 \approx 1 \times 10^4$), and a single direction is expected to adequately capture the response surface and the relation between IDT and the (A_j).

Fig. 5.3 shows a cubic fit between IDT and the reduced space variable y,

$$G(y) = \sum_{n=0}^{3} c_n y^n, \tag{5.19}$$

where $y = \mathbf{w}_1^\top \mathbf{x}$. The values of $c_0 = -3.1144$, $c_1 = -1.2182 \times 10^{-1}$, $c_2 = 6.8 \times 10^{-3}$, and $c_3 = 2.929 \times 10^{-5}$ are computed using the least-square method. The resulting probability density function (PDF) using the active subspace strategy is compared to the Monte Carlo method with $N = 20,000$ samples (Fig. 5.4). In this comparison, the Monte Carlo simulation PDF is constructed by running the primal problem simulation for each sample, and the resulting ignition delay time (IDT) from each simulation is used to build the PDF. The two PDFs match well and show the mean, μ, and the standard deviation, σ, of around-3.1 and 0.12, respectively. This comparison confirms the adequacy of the QoI used for adjoint estimation for computing the required gradients using the ASM method. In order to assess the applicability of LAAM, Fig. 5.5 compares the linear approximation of IDT to the original function, using the mean extracted from averaging $N = 200$ samples. Due to the presence of non-linearities, the linear approximation of IDT deviates from $\mu_{IDT} \pm 2 \times \sigma$. Nevertheless, in this case, due to a small variance of the PDF that clusters the samples around the mean, the linear approximation is found to be satisfactory. The resulting PDF is compared to that of the Monte Carlo and ASM for $N =$

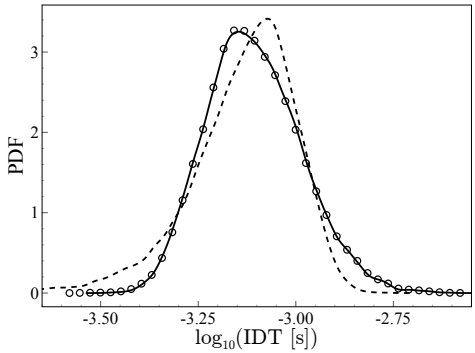


Fig. 5.4.: Comparison of the reconstructed PDF for $h2vb$ mechanism: —, ASM; ∘, Monte Carlo; – – –, LAAM.

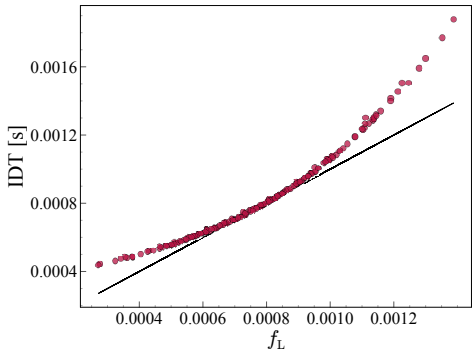


Fig. 5.5.: IDT: —, linear approximation; •, original.

20,000 samples in Fig. 5.4. The comparison between LAAM and ASM PDFs shows a deviation in the mean by $\epsilon_\mu \approx 10\,\%$ while the error in the variance is $\epsilon_\sigma \approx 2\,\%$. The departure between the peak values of the PDFs is of the order of 3 %. As a result, the overall approximation of the PDF using LAAM is satisfactory. In order to demonstrate the applicability of the approach to large mechanisms, uncertainties in the kinetic rates for the *GRI* 3.0 mechanism are extracted and investigated under the same conditions as the $h2vb$ mechanism, including the use of identical initial conditions (temperature and pressure), as shown in Fig. 5.6. The number of samples used to construct each PDF is $N = 20,000$, showing comparable results to Fig 5.4. The error in the mean between LAAM and ASM for *GRI* 3.0 is $\epsilon_\mu \approx 1\,\%$ while the error in the

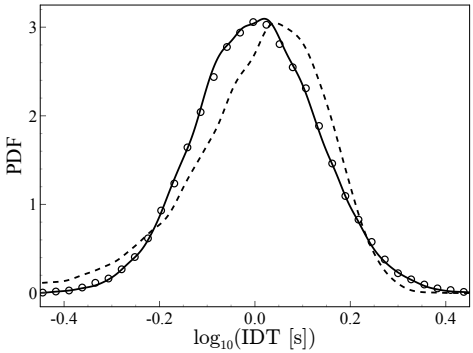


Fig. 5.6.: Comparison of the reconstructed PDF for *GRI* 3.0 mechanism: —, ASM; ∘, Monte Carlo; − − −, LAAM.

variance is $\epsilon_\sigma \approx 1\,\%$. Due to the similarity in the results produced by the two mechanisms, the imminent analysis will be carried out for *h2vb* only.

In general, the cost of LAAM is approximately two orders of magnitude lower than ASM, since all the information is gathered using a single forward-then-backward sweep. The computational expense of ASM compared to LAAM increases significantly as the size of the mechanism increases. This remarkable reduction in cost highlights LAAM's advantage, specifically as a first estimation of the uncertainties of large mechanisms. For demonstration, the cost of the two algorithms is compared in Tab. 5.2 for various mechanisms using the same number of samples, N. This table confirms that the computational cost of LAAM is negligible compared to ASM, scaling as $\mathcal{O}(N)$.

Table 5.2.: Response surface construction algorithm.

Mechanism	h2vb	GRI 1.2	GRI 2.11	GRI 3.0	ITV
Species number	10	32	49	53	490
Reaction number	21	177	297	325	2072
Time_{LAAM} [s]	161.163×10^{-3}	2.57	5.963	14.869	2267.604
Time_{ASM} [s]	50.436	1202.813	3715.522	11570.595	2.683×10^{6}

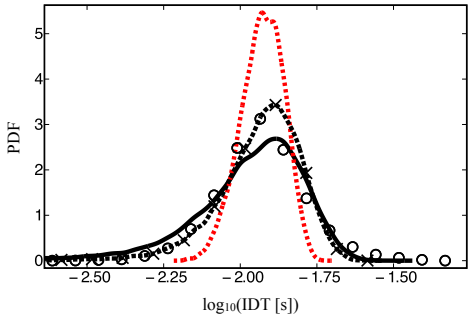


Fig. 5.7.: Comparison between different PDFs: ∘, Monte Carlo; . . . , response surface using a single eigenvector; · · · × . . . , response surface using two eigenvectors; —, LAAM.

5.2.2. Multi-dimensional subspace

The cases that are studied in applications of interest to this work [44, 45] are commonly reduced to a single dominant direction (one dominant eigenvalue), which can be fitted with a response line. However, this cannot be generalized to all the operating points, especially when considering uncertainties of IDT, for example in high-density isochoric reactors where the ignition delay time increases.

One such case is replicated here by using similar initial conditions as in [44], for $h2vb$, with a slightly lower initial temperature, $T_0 = 925\,K$ and mixture composition ($Y_{H_2} = 0.29$, $Y_{O_2} = 0.15$, $Y_{N_2} = 0.56$ and $P_0 = 1.59 \times 10^5\,Pa$). It should be noted that this case results in higher density compared to the case studied in Sec. [3.1]. As density increases so does IDT and the dispersion of the sample points, causing a polynomial fit using a single dominant direction to become inaccurate, as shown in Fig. 5.7 where the PDF using a single direction is compared to the Monte Carlo. This figure shows that using a single direction causes the peak magnitude to be overpredicted.

However, this issue can be overcome by applying a multi-dimensional subspace using the first two eigenvectors. Fig. 5.8 shows that the majority of the sample points align in a flat surface, which can be mapped using a multi-dimensional least square method fitted to a plane. Comparing the two PDFs in Fig. 5.7 plotted using 20000 samples exhibits an improvement in the accuracy using two dominant directions instead of one. Although the three PDFs have similar shapes, the standard deviation of the PDF constructed using a single eigenvector is much lower than the PDFs using Monte Carlo and two eigenvectors. However, it is important to note, that similar to the case

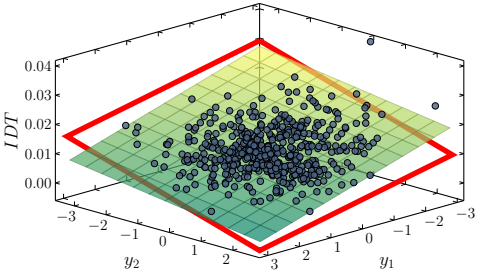


Fig. 5.8.: Response surfaces constructed in multi-dimensions : □, LAAM; □ ASM; •, samples.

considered in the previous section, the deviation in the mean value is not high, therefore I would expect LAAM to also perform satisfactorily in this context. Fig. 5.7 also compares the prediction of LAAM to the Monte Carlo, and response surfaces using one and two directions. While similar to the response surface using a single direction the peak of the PDF is not estimated correctly, LAAM is able to predict a correct shape for the distribution. The linear approximation of the QoI using LAAM (Eq. 5.14) can also be projected on the active directions (y_1, y_2) to assess how well it approximates the response surface. This projection $f_{LAAM}(\mathbf{x}) \Rightarrow f_{LAAM}(y_1, y_2)$ is shown by the plane with the highlighted borders in Fig. 5.8. This figure shows that LAAM is able to approximate this response surface closely and therefore provides a better approximation than the ASM response surface with only one direction as shown in Fig. 5.7. However, the peak of the PDF is underestimated due to the linearity of the approximation. In order to provide some insight into the manner by which the active dimensions are selected, Fig. 5.9 shows the linear combination of the rate parameters constructing these dimensions. Comparing the two dominant eigenvectors shows R1 to be the most sensitive reaction in one direction $y_1 = \mathbf{w}_1^\top \mathbf{x}$ and R5 in the other direction $y_2 = \mathbf{w}_2^\top \mathbf{x}$. Therefore, further analysis is required in order to identify the reaction with the highest overall sensitivity. In multiple directions, the linear combination alone might be misleading and the analysis of the global sensitivity is necessary to understand the reaction pathway. Here, I compute this quantity by calculating the gradient of the response surface, $\frac{dG(y)}{dx}$, and averaging the result over the entire sample, resulting in the final global gradient with respect to system parameters, as shown in Fig. 5.10. This figure shows that considering only a single active dimension overestimates the role (sensitivity) of the fifth and twelfth reaction (R5, R12) causing them to have a significant contribution to

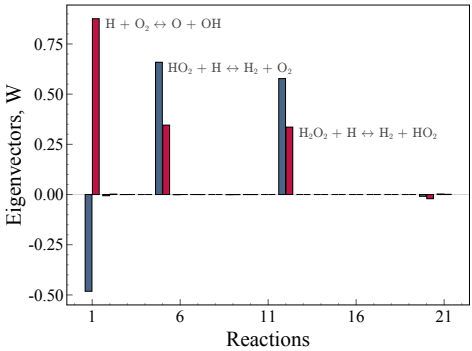


Fig. 5.9.: First two dominant eigenvectors, first; second; showing the linear combination of rate parameters.

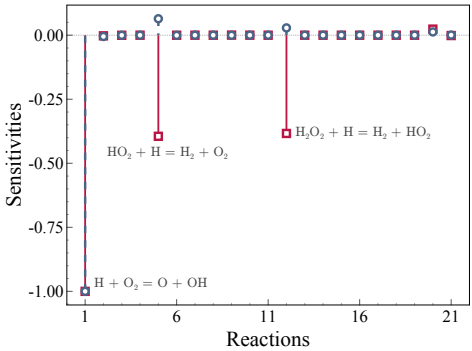


Fig. 5.10.: Global sensitivity of IDT: (red), one active dimension; (blue), two active dimensions.

the ignition process, while using two active dimensions retrieves the dominance of R1 ($H + O_2 = O + OH$), responsible for OH production, in agreement with the literature [25].

5.2.3. Initial conditions effect

The results presented in Sec. 5.2.1 and 5.2.2 compare the extracted sensitivities using ASM and LAAM for cases exhibiting weakly nonlinear dependence of the QoI with respect to the parameter space. Here, I aim to lift this constraint by extracting the uncertainties of IDT with respect to variations in the initial conditions, showing strong nonlinear behavior, and test whether the LAAM

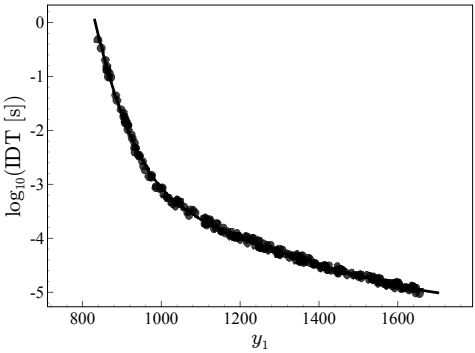


Fig. 5.11.: Comparison of the response surface fitted against a single active direction in case of a uniform distribution for initial conditions: •, samples; ——, tenth-order polynomial fit.

approach can provide acceptable predictions. For this purpose, a random combination of initial fuel mass fraction Y_{0,H_2} to air mass fraction Y_{0,O_2} ratio, and temperature T_0 are extracted from a uniform distribution defined as,

$$\Omega_i = U\big(\Omega_j \times (B+1), \Omega_j \times (B-1)\big), \tag{5.20}$$

$$\Omega_j = (Y_{H_2}, Y_{O_2}, Y_{O_2}, T_0)\,, \tag{5.21}$$

where B is the percentage of deviation from the mean value Ω_i. The test case mean value Ω_j will be similar to the studied case in Sec. 5.2.1 with twenty percent of variation $B = 0.2$ around this value.

Following the procedure for constructing the active subspace, the resulting response surface (not shown here) is divided into two regions, separating igniting and non-igniting samples. Since quantifying the uncertainties of IDT is the purpose of this work, the cases without ignition are discarded, allowing the reduction of the active dimensions to one, as shown in Fig. 5.11. The response line is calculated using a tenth-order polynomial. Examining the chosen eigenvector (identified direction) shows that the temperature T_0 has the biggest influence on the selected direction. This can be expected as the temperature affects the reaction rate nonlinearly and can cause larger gradients when constructing the expectation matrix, $\mathbf{C}$. Therefore, the uncertainties in IDT are mainly due to the variation in the initial temperature. The resulting PDFs are shown in Fig. 5.12. This figure illustrates that employing the response surface in a single direction provides an accurate approximation of the overall probability density function (PDF), serving as a reference similar

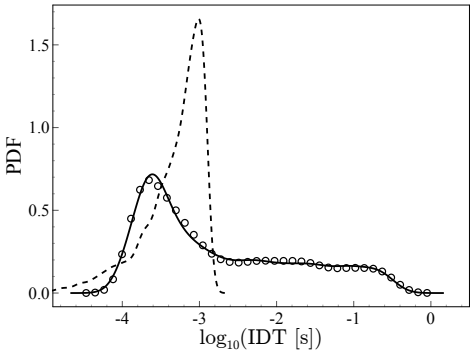


Fig. 5.12.: Comparison of the reconstructed PDF: —, ASM; ∘, Monte Carlo; – – –, LAAM.

to the Monte Carlo method. The comparison to the PDF built using the LAAM approach shows a large deviation from the rest. This case highlights the limitations of the LAAM approach. Several reasons contribute to this huge deviation between LAAM and Monte Carlo PDFs, but the main factor can be attributed to the use of the uniform distribution for the initial conditions $[Y_i, T_0]$ in the presence of a large variance, reducing the correlation between the computed gradient at the mean and the other samples. In addition, at high initial temperatures (above the mean value) the reaction time t_r is very small. As the initial temperature decreases, t_r dramatically increases, causing the deviation in IDT to also increase, resulting in a large tail in the PDF. As a result, the skewness and flatness of the PDF in Fig. 5.12 are different from the PDFs in Figs. 5.4 and 5.7. The resulting PDF is therefore hard to capture using linear approximation. This also necessitates a higher-order polynomial fit (tenth order) when using the ASM method to create the response surface.

However, this error can be reduced by using piece-wise linear approximations by splitting the domain into smaller segments and applying LAAM at the mean value of the samples at each part individually. It is important to note that the number of simulations would remain in the same order of magnitude; nevertheless, the accuracy would significantly increase [72]. Alternatively, higher-order derivatives could be used, which will be the subject of future work.

5.3. Summary and Conclusions

As a conclusion, it is found that the change of mixture initial conditions plays a key role in determining the number of dominant directions used to construct the response surface for different QoIs. Moreover, the distribution functions of the model parameters contribute to the accuracy of the constructed PDF, and this accuracy strongly varies depending on the UQ methods (LAAM, AASM, etc.). Finally, the global sensitivity analysis and uncertainty quantification will provide answers about the actual influence of any perturbation of the different model parameters on the QoI values that cannot be provided by local sensitivity analysis. This serious outcome will be used in the following chapter 6 which will be a melting bowl for all the different models involved in solid fuel combustion such as char combustion, devolitization, gas-phase ignition, along with the methods that have been discussed in this study so far, in particular sensitivity analysis and uncertainty quantifications.

6

Uncertainty quantification and sensitivity analysis of single axisymmetric particle combustion

This chapter combines various models (i.e., solid and gas phase chemical kinetics) in the simulation of solid fuel combustion with the developed methods for sensitivity analysis and uncertainty quantification introduced in the previous chapters 2, 4, and 5. The primary goal is to conduct a simulation of an unsteady single solid particle that considers detailed gas phase chemistry, devolatilization coupled with char combustion, and differentiate the role of each phenomenon in the combustion behavior of the solid particle. This simulation is compared in both conventional air and oxy-fuel atmospheres. The evolution of the particle temperature distinguishes two different stages of particle combustion: before and after gas phase ignition. The sensitivity analysis is carried out to determine the most effective parameters for particle temperature and particle burning rate. The results show that the particle diameter is the most effective parameter for particle temperature, while the devolatilization parameters are the most effective for particle burning rate. Additionally, the onset of the gas phase ignition identifies two different stages in the evolution of sensitivities of various quantities of interest with respect to gas and solid-phase parameters. The uncertainties associated with gas phase reaction rates demonstrate that the reactions involving volatile species, particularly hydrogen radicals, are the most active in the reaction pathway. Finally, the PDF based on the predictions of the active subspace method shows good agreement with the PDF based on Monte Carlo but with significantly less cost.

6.1. Governing equations

The governing equations that describe the flow around a reactive axisymmetric particle in a fluid are presented in a similar way as in Chapter 4, Section 4.1.

The main difference in the governing equation can be noticed in the burning rate of the particle, where the devolatilization effect should be included. To express the variation in the particle mass due to char combustion and volatilization, it can be computed as,

$$\frac{dM_p}{dt} = -\dot{M}_s \tag{6.1}$$

6.1.1. Chemical and thermodynamic models

Several terms introduced in the previous equations require modeling. In this section, the chemical and thermodynamic models used to close the above system are discussed.

Volatilization

A two-step reaction model [75, 76] with first-order kinetics is used to represent the mass release of volatilized species, given by

$$\dot{m}_{v,i} = \zeta_i K_{v,i} M_p, \tag{6.2}$$

where $\zeta_1 = \zeta_2 = 0.5$ are the release constants. The volatile release rate $K_{v,i}$ follows the Arrhenius law, with the rate constant values for the multiple steps given by $E_{v,1} = 74.1\,kJ\,mol^{-1}$, $A_{v,1} = 1.34 \times 10^5\,s^{-1}$, $\beta_{v,1} = 0$, $E_{v,2} = 251\,kJ\,mol^{-1}$, $A_{v,2} = 1.46 \times 10^5\,s^{-1}$ and $\beta_{v,2} = 0$. The heat release associated with volatilization is $h_{v,1} = h_{v,2} = 1 \times 10^3\,kJ\,kg^{-1}$ [75]. The species composition resulting from devolatilization processes is listed in Tab. 6.1.

Species	H	CO	CO_2	CH_4
Composition	32.6 %	0 %	10.5 %	56.9 %

Table 6.1.: Volatile species composition.

Gas-phase kinetics

The gas-phase chemistry is presented by the GRI 1.2 mechanism which includes 177 reactions between 32 species. The different thermodynamic properties for each species are computed using NASA polynomial correlations [77].

6.2. Results

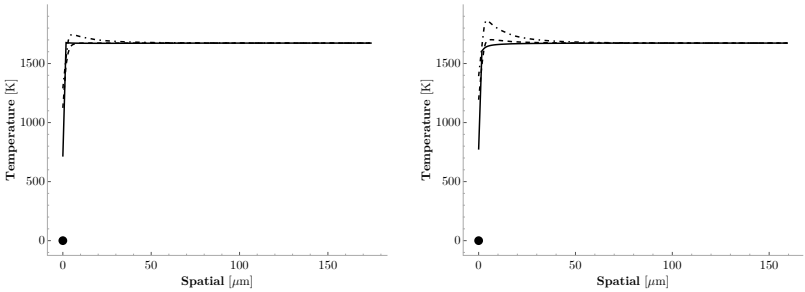
In the following, the model sensitivities and uncertainties of a single reacting particle are presented for two different freestream compositions representing air and oxy atmospheres. The initial composition of the oxy atmosphere and the air atmosphere with rich oxygen is similar to that in [4, 76], and is described in Tab. 6.2.

Test case	Diluent	$Y^\infty_{O_2}$	Y^∞_{CO}	$Y^\infty_{CO_2}$	$Y^\infty_{N_2}$	T^∞
Air	N_2	32.6 %	0 %	10.5 %	56.9 %	1673 K
Oxy	CO_2	26.2 %	0 %	73.8 %	0 %	1673 K

Table 6.2.: Compositions of air and oxy atmospheres.

6.2.1. Forward (primal) problem

The initial particle temperature is set to $T_p^o = 300\,K$, which is low enough to allow devolatilization as the particle heats up and before the char combustion takes place [4, 76]. Fig. 6.1 illustrates the spatial evolution of the temperature profile at specific times, which reveals that the gas phase temperature increases post-ignition and decreases near the particle surface. This temperature profile behavior suggests that energy is transferred from the hotter gas phase to the cooler particle surface. The evolution of temperature profiles between air and oxy atmospheres reveals that ignition occurs faster in the oxy atmosphere, which is consistent with the findings of Farazi *et al.* [4], who used the same volatilization model. The choice of volatilization model significantly impacts the ignition time, and different models can lead to conflicting results. In this study, the two-step model was used, which produces a similar rate of species release to that of the model used in the char combustion mechanism by Bradley [78]. This similarity could have an impact on the model's predictions presented in this study. The combination of volatiles that are released depends

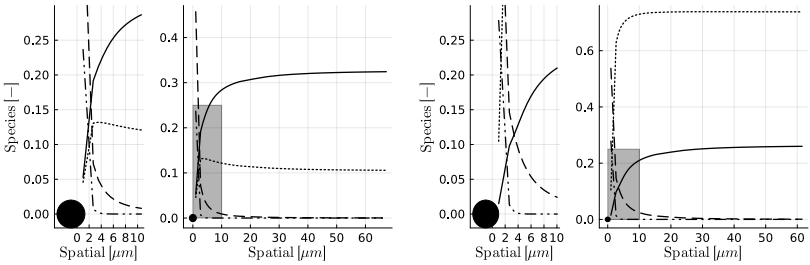


(a) Air atmosphere **(b)** Oxy atmosphere

Fig. 6.1.: Spatial evolution of the gas phase temperature for the air and oxy atmospheres. The solid (– – –), dashed (– – –), and dash-dotted (–.–) lines correspond to $t = 1\,ms$, $4\,ms$, and $6\,ms$, respectively.

on both the fuel type and the complexity of the devolatilization model used. In a study investigating particle devolatilization and combustion, where the C2SM model was utilized [79], it was observed that during the devolatilization process volatile species like CO and CH_4 accumulated at the particle surface due to their lower diffusion rate, similar to what is observed here. On the other hand, as shown in Fig. 6.2a, carbon dioxide peaks far from the particle surface. This can be attributed to the high reactivity of the reaction involving

$OH + CO = H + CO_2$, which leads to the consumption of carbon monoxide and the production of carbon dioxide. It should be emphasized that during this phase, char combustion, also known as heterogeneous ignition, is negligible due to the unavailability of oxygen at the particle surface. This is due to the fact that oxygen is consumed in gas-phase reactions during the devolatilization process. It is essential to identify different stages of the temporal evolution

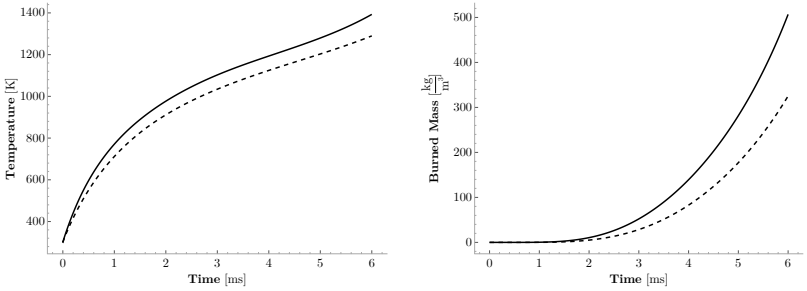


(a) Air atmosphere **(b)** Oxy atmosphere

Fig. 6.2.: Distribution of species in air and oxy atmospheres in the gas phase at a specific timestamp of $t = 4\,ms$. The dotted line (...) represents the distribution of CO_2, the solid line (– – –) represents O_2, while dashed lines (– – –) represent CO and dash-dot lines (–..) represent CH_4.

of quantities of interest such as burning rate and particle temperature [80]. These quantities will later be used to characterize parametric sensitivities. As these QoIs indicate the different stages of particle combustion (preheating, devolatilization, ignition, etc.), they help to study the mutual effects and transitions between different phenomena. Additionally, particle temperature is a major parameter measured in different experiments [54, 81], and can be used to compare and validate numerical results against experimental data [57]. In both the air and oxy environments, the particle temperature T_p increases due to the temperature gradient between the hot medium and the colder particle. During the initial heating stage ($t < 0.5\,ms$), both cases experience similar heating rates due to the significant temperature difference between the gas and solid phases, as depicted in Fig. 6.3a. However, the heating rate for the air atmosphere is lower than that of the oxy atmosphere due to the more rapid increase in the gas phase temperature for oxy relative to air. An inflection point can be observed in the T_p evolution curve in Fig. 6.3a around $t \approx 6\,\mu s$, which is related to the initiation of char ignition. Notably, the inflection point is not observed for the air atmosphere due to the lower particle heating rate. Sensitivities of char combustion have been analyzed in

a different study by Hassan *et al.* [47].



(a) Particle temperature **(b)** Particle burned mass

Fig. 6.3.: Temporal evolution of particle temperature and burning rate: – – – air atmosphere; —- oxy atmosphere.

Fig. 6.3b shows two different stages of the evolution of the particle burning rate. The first stage coincides with a region where the burning rate does not depend on the atmosphere, i.e., the early stage of particle heating. The second stage, after the ignition onset, coincides with a monotonic increase in the particle burning rate. The rate of change is higher for the oxy atmosphere.

6.2.2. Extracted sensitivities

This section aims to compute the sensitivities of various quantities of interest (QoI) with respect to different system parameters using the adjoint method. The gradients will be computed for both the air and oxy atmospheres, whose compositions are presented in Table 6.2. Additionally, the evolution of sensitivities over time will be examined. All sensitivities are normalized, which helps distinguish the dominant parameters.

Sensitivities of Particle temperature

To evaluate sensitivities over all combustion phases and to avoid the complexities of particle ignition, we examine the time-cumulative particle temperature T_p rather than its instantaneous value, resulting in,

$$\text{QoI} = \frac{1}{\mathcal{T} - \tau_0} \int_{\tau_0}^{\mathcal{T}} T_p \, d\tau. \tag{6.3}$$

The integration limits in Eq. 6.3 are $\tau_0 = 0$ and $\mathcal{T} = 5\,ms$ chosen to ensure that gas phase ignition occurs in both air and oxy atmospheres, while avoiding char combustion. The sensitivities of particle temperature with respect to different parameters are shown in Fig. 6.4. This figure shows that particle size is the most influential parameter, with increasing particle size resulting in lower temperatures, as demonstrated in [63]. Sensitivities to particle thermodynamic parameters (C_c and λ_s) are the most prominent during the heating-up phase. Sensitivities with respect to char combustion parameters E_c, β_c, and A_c are insignificant due to the absence of heterogeneous ignition: as discussed in Sec.6.2.1, oxygen is mainly consumed by gas-phase combustion. Particle temperature also shows low sensitivities with respect to various devolatization parameters. These parameters are, however, important when considering particle burning rate, as demonstrated in [4] and subsequently gas-phase ignition, and will be highlighted in the following section. Comparing sensitivities in air and oxy atmospheres reveals a similar pattern for both. Notably, the sensitivity to particle parameters r_0, C_c, and λ_s is slightly lower in an air atmosphere due to weak flammability, where the temperature gradient between gas and particle decreases as shown in Fig. 6.1a.

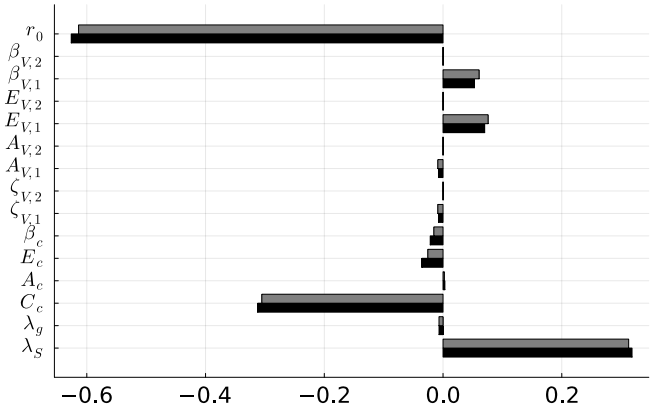
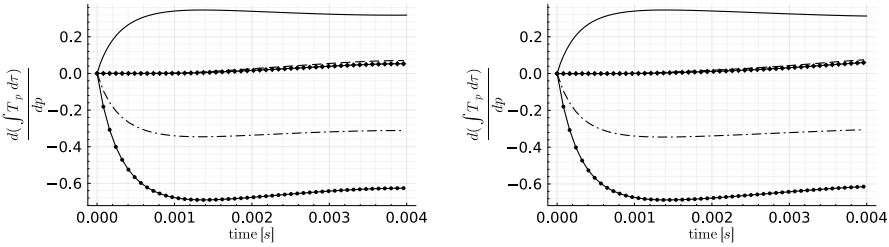


Fig. 6.4.: Sensitivity of the average particle surface temperature with respect to the system parameters in the air (■) and oxy (■) atmospheres.

Given the unsteady nature of the problem, it is important to investigate the temporal evolution of sensitivities with respect to the most influential system parameters. This is achieved by adjusting the limits of the integral in Eq. 6.3 to encompass the entire time domain of the QoI. The time domain is then discretized into several sequential segments, and the sensitivities are computed

individually for each segment and then aggregated to provide the complete time evolution. These results are shown in Fig. 6.5, which demonstrates that the sensitivity of particle temperature (T_p) with respect to surface heat conductivity (λ_s) for both air and oxy atmosphere increase until $t \approx 1.5\,ms$. This is because the gradient between the adjacent gas layer and particle temperatures decreases significantly at this stage, minimizing the effect of λ_s. Gas conductivity λ_g follows a similar trend but with a more rapid decay rate due to the propagation of the flame towards the particle surface (not shown here). Both volatiles activation energy and temperature exponent, ($E_{v,1}$ and $\beta_{v,1}$), show a similar behavior independent of the atmosphere (air/oxy). They begin to have an impact after the early non-linear heating phase, close to the gas phase ignition onset, as demonstrated in Fig. 6.3a. The sensitivities to particle radius and thermal capacity (r_0 and C_c, respectively) increase in both atmospheres as the heating rate of the particle $\frac{dT_p}{dt}$ reaches its maximum. Following the ignition onset, their sensitivities decrease slightly as the heating rate of the particle diminishes and the flame spreads towards the particle surface.

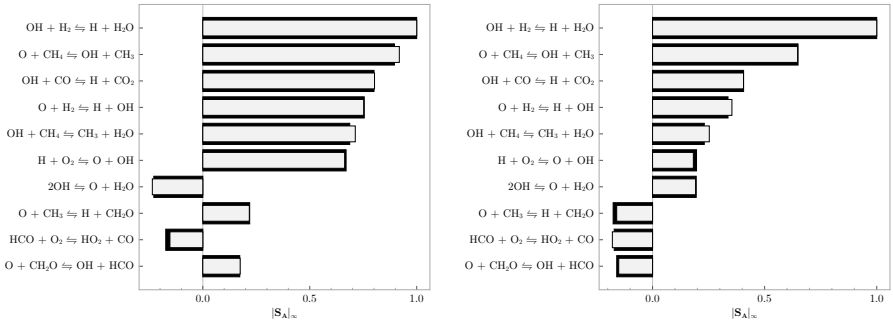


(a) Air atmosphere **(b)** Oxy atmosphere

Fig. 6.5.: Temporal evolution of the average particle temperature sensitivities with respect to the system parameters: —, λ_s; − − −, $E_{v,1}$; −•−, r_0; −.−, C_c; −♦−, $\beta_{v,1}$.

The sensitivities of particle temperature with respect to gas phase reactions rate are shown in Fig. 6.6. According to Fig. 6.6a, the reaction $OH + H_2 = H + H_2O$ $(R1)$ exhibits the highest sensitivity for T_p in an air atmosphere. In fact, the top four reactions in Fig. 6.6a involve H and OH radicals. These findings highlight the sensitivity of H and OH radicals absorption/release reactions in the predicted sensitivities of particle temperature. Fig. 6.6b shows that $H + O_2 = O + OH$ $(R2)$ reaction is in turn the most sensitive in an oxy atmosphere. However, the sensitivities of H and OH radical reactions

remain important as the atmosphere changes, which could be due to the fact that these reactions make a significant contribution to the reactions involving methane (CH_4) and methyl (CH_3) present in the gas-phase. Comparing Figs. 6.4 and 6.6 reveals that the sensitivities of the reaction rates depend strongly on the atmosphere used, which is in contrast to the system parameters that show little variations across different environments. To assess the effect



(a) Air atmosphere **(b)** Oxy atmosphere

Fig. 6.6.: Sensitivity of the average particle surface temperature with respect to the rates of gas phase reactions of different mechanisms for air and oxy atmospheres: DRM22 (■) and GRI1.3 (■).

of the mechanism used to model the gas phase chemistry on the extracted sensitivities, a simpler reduced kinetics mechanism (DRM22) [82], consisting of 104 reactions and 22 species, is implemented in the simulation. The sensitivities of the particle temperature with respect to the different gas phase reaction rates are shown in Fig. 6.6. A comparison with results from the detailed mechanism shows that the top ten most sensitive reactions are indeed the same in both cases. Furthermore, R_1 and R_2 are still the dominant reactions in air and oxy-atmosphere respectively, regardless of the mechanism used. A noticeable difference is the change in order between the two reactions $(O + CH_4 = OH + CH_3)$ and $(OH + CO = H + CO_2)$, but the sensitivity of the two reactions is still comparable.

Sensitivities of burning rate

The burning rate, denoted by $\dot{m}_t$, is a crucial QoI in particle combustion analysis. Similar to T_p, the burning rate is consistently increasing over time.

Therefore, it is reasonable to define the time-averaged value of the burning rate as the QoI. This value can be defined as follows:

$$\text{QoI} = \int_{\tau_0}^{\mathcal{T}} \dot{m}_t \, d\tau. \tag{6.4}$$

Rather than analyzing the separate effects of char combustion and devolatilization ($\dot{m}_t = \dot{m}_c + \dot{m}_v$), it is possible to construct a QoI based on the variation of the total particle mass as shown in equation 6.1,

$$\text{QoI} = \int_{\tau_0}^{\mathcal{T}} \dot{m}_t \, d\tau = -\int_{\tau_0}^{\mathcal{T}} \frac{\partial M_p}{d\tau} \, d\tau, \tag{6.5}$$

$$\text{QoI} = -\int_{\tau_0}^{\mathcal{T}} \frac{\partial M_p}{d\tau} \, d\tau = M_p|_{\tau_0} - M_p|_{\mathcal{T}}, \tag{6.6}$$

This approach allows for a more comprehensive evaluation of the overall behavior of the combustion process. Taking the derivative of the QoI with respect to the state vector (q) and incorporating it into the initial conditions of the adjoint equations, Eq. 4.32, leads to the following equations:

$$\eta^d_{q^*}(\mathcal{T}) = 0, \qquad q^* = \{T_p, Y, T, Y_s\} \tag{6.7}$$

$$\eta^d_{M_p}(\mathcal{T}) = -1. \tag{6.8}$$

The value of τ_0 and $\mathcal{T}$ are chosen to be similar to T_p in order to facilitate their comparison. Fig. 6.7 displays the sensitivity analysis results with respect to the various system parameters. The sensitivity values for r_0 are significant, similar to that of the particle temperature, owing to the strong correlation between T_p and $\dot{m}_t$. However, in contrast, the devolatilization parameters have the most dominant effect when the char combustion rate is low, as $\dot{m}_t$ is approximately equal to $\dot{m}_v$, as there is no heterogeneous ignition. In comparison to the extracted sensitivities of particle temperature (Fig. 6.4), Fig. 6.7 indicates lower sensitivities for the thermodynamic parameters.

Time evolution of particle burning rate sensitivities with respect to the top sensitive parameters is depicted in Fig. 6.8. Similar to particle temperature, the sensitives of the dominant parameters reach their maximum when ignition occurs ($t = 0.001$ *sec*). These results are expected due to the strong impact of gas phase ignition on devolatilization rate and temperature gradient between the gas and particle surface. Comparing Figs. 6.8 and 6.5 shows that the sensitivity of the temperature exponent $\beta_{v,1}$ in the devolatilization model with

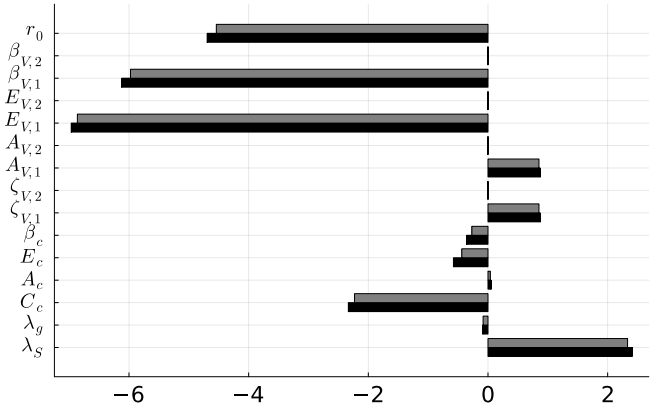
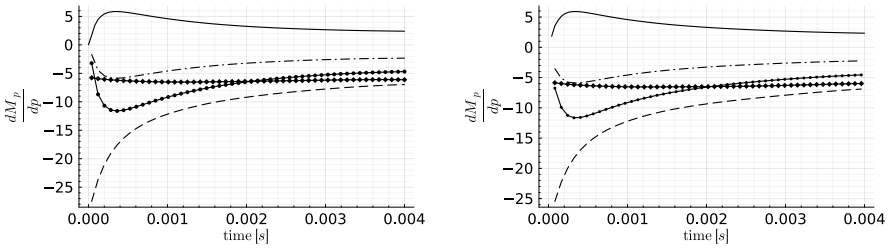


Fig. 6.7.: Sensitivity of the average particle burning rate with respect to the system parameters in the air (■) and oxy (■) atmospheres.

respect to burning rate remains nearly constant regardless of the atmosphere. However, it exhibits a higher sensitivity value when compared to particle temperature.

In both atmospheres, the particle burning rate is highly sensitive to the volatile activation energy $E_{v,1}$, especially at an early stage, where $\dot{m}_t \approx \dot{m}_v$ and char combustion is negligible. After gas phase ignition, the particle temperature T_p becomes high enough and the sensitivity of the volatile activation energy dwindles with a similar rate independent of the atmosphere. It is worth noting that the signs of the sensitivities remain consistent and align with the findings presented in Fig. 6.7. Additionally, the sensitivity of $E_{v,1}$ emerges as the most influential across all instances.

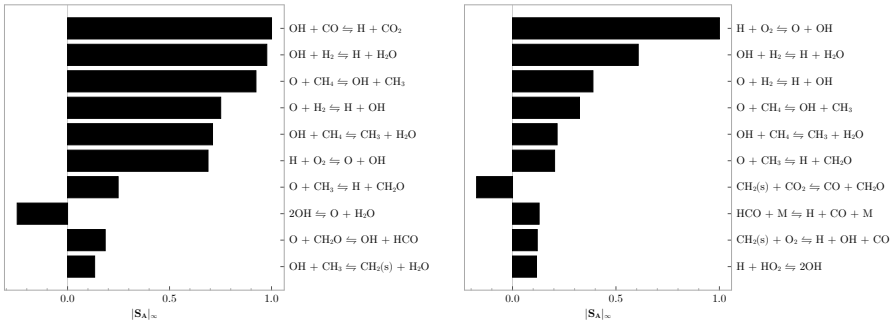
Comparison of Figs. 6.8 and 6.5 shows that while the atmosphere does not seem to influence the value and evolution of sensitivities with respect to different system parameters, the selected QoI could have a large influence. This suggests that depending on the quantity we would like to predict in such systems, different system parameters could be influential, and how influential depends on the time instance that the analysis is performed. Fig. 6.9 highlights the sensitivities of the particle burning rate with respect to the gas phase reaction rates. These results are consistent with the time-cumulative particle temperature results depicted in Fig. 6.6. The agreement is expected as the ignition process, particle temperature, and the burning rate are highly correlated in this setting. The only notable difference between Figs. 6.9a and 6.6a is that the reaction $OH + CO = H + CO_2$ is the most dominant



(a) Air atmosphere **(b)** Oxy atmosphere

Fig. 6.8.: Temporal evolution of the average particle burning rate sensitivities with respect to the system parameters: —, λ_s; − − −, $E_{v,1}$; −•−, r_0; −.−, C_c; −♦−, $\beta_{v,1}$.

for the burning rate, due to the high release rate of carbon dioxide in the air atmosphere, as shown in Fig. 6.2a. It is worth noting that, similar to the particle temperature, Figs. 6.9a and 6.9b illustrate that the reactions involving volatile species are the most sensitive.

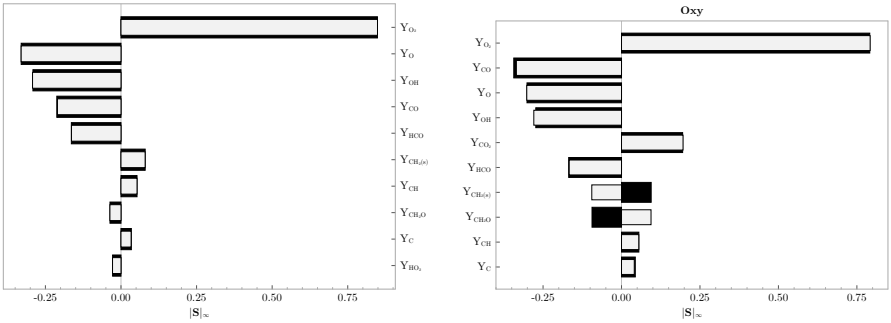


(a) Air atmosphere **(b)** Oxy atmosphere

Fig. 6.9.: Sensitivity of the average particle burning rate with respect to the rates of gas phase reactions.

In order to provide a comprehensive understanding of the sensitivity of the different parameters involved in the simulation, the sensitivities of the particle temperature and the burning rate to the initial free-stream composition are extracted and compared. Figs. 6.10a and 6.10b demonstrate that, regardless of the atmosphere or the quantity of interest, Y_{O_2} is the most dominant species, and controls the ignition process for both the gas phase and the particle. It is

noteworthy that the sensitivity of carbon monoxide is more pronounced in the oxy atmosphere than in the air atmosphere.



(a) Particle temperature **(b)** Burning rate

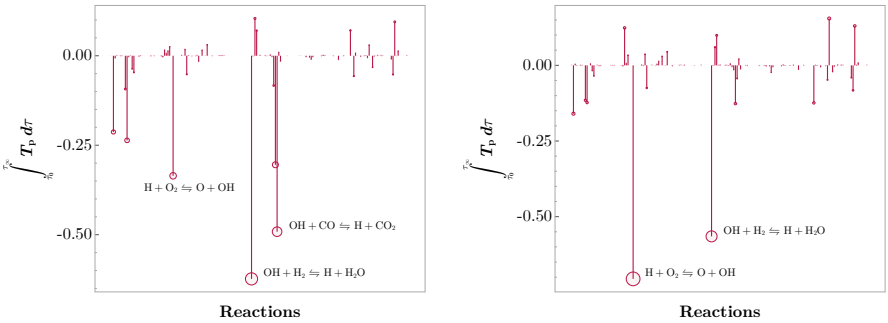
Fig. 6.10.: Sensitivity of the average particle temperature and burning rate with respect to the initial mass fraction composition in the oxy (■) and air (■) atmospheres.

The comprehensive sensitivity analysis conducted on various quantities of interest demonstrates that the sensitivities to system parameters remain constant across different atmospheres, regardless of atmospheric composition. Conversely, the combustion atmosphere significantly influences the hierarchy of the most sensitive reactions across different quantities of interest.

6.2.3. Extracted uncertainties

As shown in the previous section and due to their impact on both particle temperature (T_p) and burning rate ($\dot{m}_t$), it is crucial to quantify the impact of uncertainties in gas phase kinetics and system parameters on the prediction of these quantities of interest. The uncertainties will be extracted as explained in Tab. 5.1. Due to the cost associated with the forward problem and gradient extraction, as well as the high accuracy of AASM, a total of 100 samples ($N = 100$) are utilized to construct the covariance matrix. A single dominant direction (the eigenvector related to the first eigenvalue) is picked to build the response surface of particle temperature T_p and the particle burning rate $\dot{m}_t$. First the uncertainties with respect to the gas phase kinetic models will be investigated. In this context, the dominant eigenvector is used as a representative of the dominant reaction pathway, shown in Fig. 6.11, using the average particle temperature as the QoI. These results can be directly compared to the results of the sensitivity analysis shown in Fig. 6.6. Fig. 6.11

shows that $OH + H_2 = H + H_2O$ (R1) and $H + O_2 = O + OH$) (R2) are the most dominant reactions in air and oxy atmospheres, respectively, contributing significantly to the overall uncertainty of predictions. It is worth noting that R2 also strongly contributes (within the top three reactions) to the predicted uncertainties of the air atmosphere. This is in contrast with the sensitivity analysis shown in Fig. 6.6a, where (R2) ranks lower in the hierarchy of sensitive reactions. This highlights the limitation of a local method such as sensitivity analysis to analyse a complex system such as the one presented here. Reaction $OH + CO = H + CO_2$ remains important in the air atmosphere due to the elevated production of (CO_2). This result is in alignment with the findings of the local sensitivity analysis in Fig. 6.6.



(a) Air atmosphere **(b)** Oxy atmosphere

Fig. 6.11.: Uncertainties of reaction pathways for cumulative particle temperature.

As mentioned previously, it is essential to assess the evolution of uncertainties over time in unsteady configurations. To accomplish this, the integration limits in Eqs. 6.4 and 6.3 are sequentially changed from 0 to 5 ms. Fig. 6.12 depicts the evolution of the predicted mean value and standard deviation, amplified 50 times for better visibility, superimposed. This figure reveals that the uncertainties are negligible during the heating phase regardless of the atmosphere and the QoI, and it becomes relatively more significant after the gas phase ignition. This is because the gas phase chemistry has minimal influence before the ignition onset. In addition, the uncertainties in the oxy atmosphere is consistently higher than that in the air atmosphere for all quantities of interest. Moreover, the uncertainties in the burning rate exceeds that of the particle temperature. This is attributed to the fact that the burned mass is more sensitive to gas phase kinetics compared to the particle temperature.

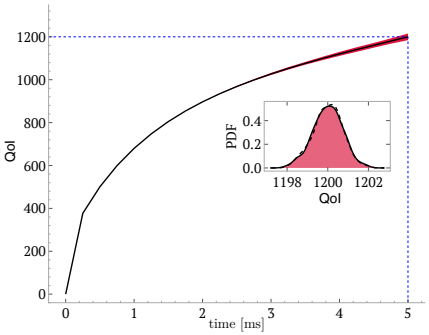
In order to examine the statistical properties of the response surface for different quantities of interest in more detail, the probability density function (PDF) of the QoIs is plotted at $t = 5\,ms$ and compared with the Monte Carlo method. The error between the PDF moments of the Monte Carlo simulations and the reduced order model is calculated using equation:

$$\epsilon^i = \frac{\mu^i_{MC} - \mu^i}{\mu^i_{MC}} \times 100, \tag{6.9}$$

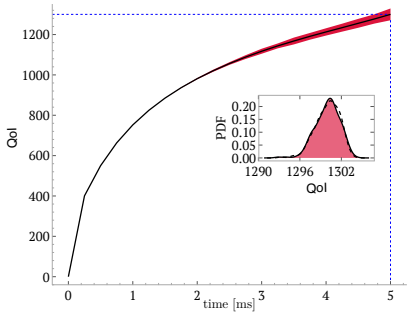
where i corresponds to the order of the moment. The mean errors of the response surface PDF are $\epsilon^1 = 1 \times 10^{-6}\,\%$, indicating an accurate approximation of the mean for both air and oxy atmospheres. However, it's worth noting that the limited number of samples used to construct the response surface ($N_r = 177$ reactions and the domain size $r_\infty = 160\,mm$) can affect the accuracy.

When comparing the PDFs of the air and oxy atmospheres, it can be observed that the oxy atmosphere exhibits a much higher skewness (ten times larger) due to its high flammability. This leads to a larger number of samples with high particle heating rates. Nevertheless the overall low standard deviations indicate the high performance of the different models, regardless of the atmosphere and the quantities of interest (QoIs).

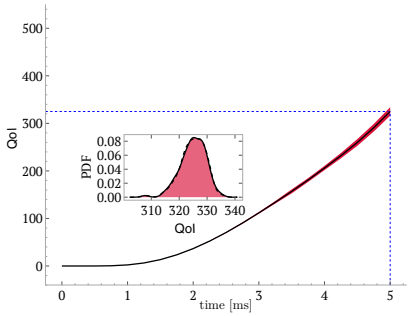
Finally, In order to examine the uncertainties of system parameters on the overall predictions of the burning rate and particle temperature, we perform a separate analysis where the kinetic parameters of gas-phase reactions are fixed and AASM method is applied only on the samples extracted from the system parameters shown in Figs 6.4 and 6.7. Since the number of selected particle parameters is smaller than the parameters of the gas-phase kinetic model, only 70 samples are used to build the response surface. The dominant eigenvectors, extracted using the AASM approach, highlighting the global sensitivity of particle temperature with respect to system parameters for each atmosphere are shown in Fig.6.13 and can be compared directly to Fig 6.4. When comparing global and local sensitivities, depicted in Fig.6.13 and Fig.6.4, respectively, it becomes evident that the particle radius r_0 emerges as the most sensitive parameter. Furthermore, the global sensitivity of particle thermal conductivity λ_s, as illustrated in Fig.6.13, exceeds the sensitivity observed in the local analysis presented in Fig.6.4. In contrast to the local sensitivity, Fig.6.13 demonstrates minimal global sensitivity for particle thermal capacity C_c. Comparing Figs. 6.13a and 6.13b reveals that the global sensitivity remains consistent, irrespective of atmospheric conditions. These results are consistent with the findings from the local sensitivity analysis.



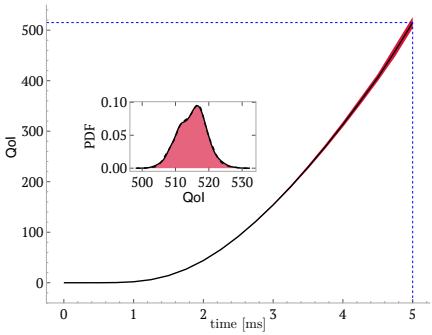
(a) Air atmosphere, particle temperature



(b) Oxy atmosphere, particle temperature



(c) Air atmosphere, burning rate

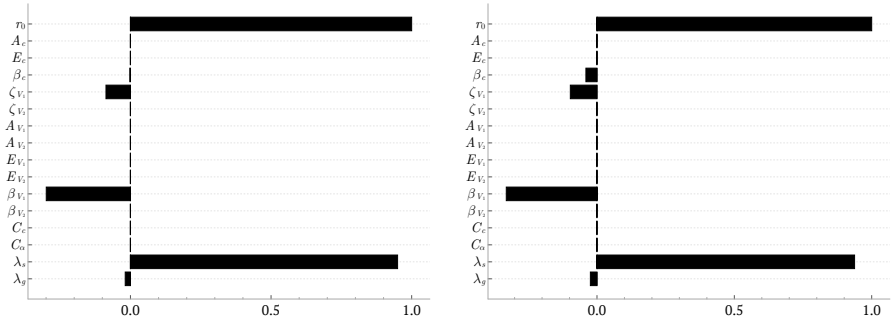


(d) Oxy atmosphere, burning rate

Fig. 6.12.: Evolution of uncertainties in particle temperature and burning rate with respect to gas-phase kinetic parameters: —, mean value (μ^0); red, standard deviation (σ).

Fig. 6.14 displays the evolution of uncertainties in particle temperature and burning rate with respect to system parameters. By comparing Figs. 6.14 and 6.12, we observe that system parameters have a much more substantial influence on uncertainties than the reactions rates. This can be attributed to the pre-ignition stage's primary role in controlling the particle's heating rate. Although the atmosphere has a negligible impact on sensitivities (Figs. 6.4 and 6.7), Fig. 6.14 demonstrates that the uncertainties in an oxy atmosphere are higher than those in an air atmosphere. Moreover, the uncertainties in the oxy atmosphere increase as ignition progresses, in line with the trends seen in reaction rate Fig. 6.12.

Uncertainties in the burning rate before ignition are almost negligible. How-

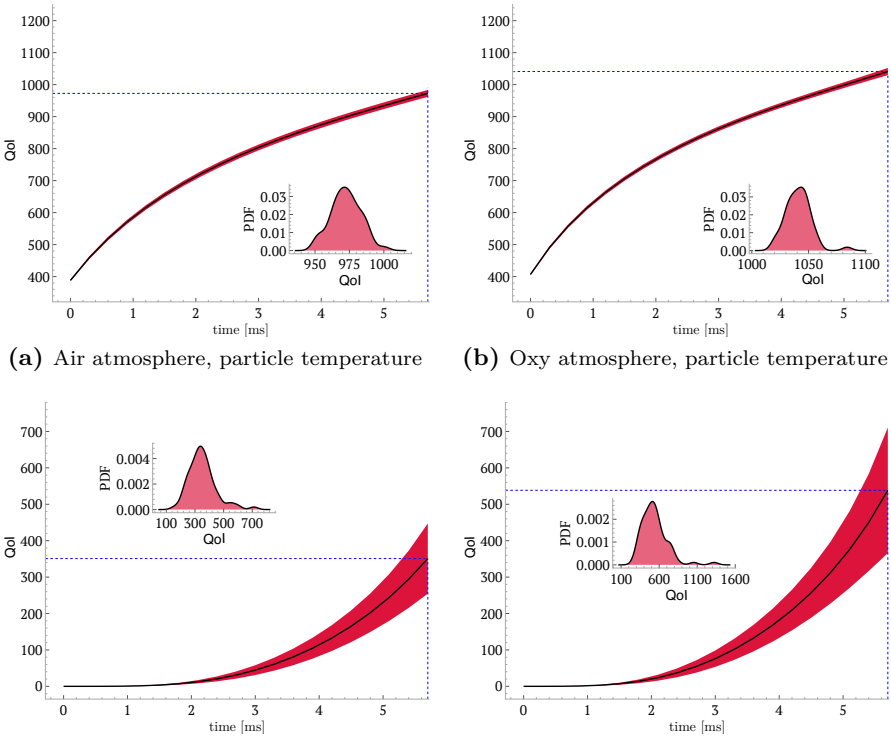


(a) Air atmosphere **(b)** Oxy atmosphere

Fig. 6.13.: Uncertainty of particle temperature with respect to the system parameters.

ever, these uncertainties become significantly more pronounced in both air and oxy atmospheres after ignition. Comparing the results of Fig.6.14 reveals that the uncertainties in burning rate are much higher than those in particle temperature. This suggests that particle burning rate is more globally sensitive to system parameters. Moreover, it is important to note that the results of the uncertainties are highly dependent on the uncertainty factor (UF). Therefore, even a small variation in the value of UF can significantly affect the evolution of uncertainties. Due to the shortage of reliable information regarding the value of the uncertainty factor for particle parameters, the chosen value is (UF=1.1), as a further increase in this value of UF could lead to unrealistic results (not show here). Comparing Figs. 6.14 and 6.8 reveals that while the sensitivities of system parameters remain unaffected by the atmosphere, the uncertainties is significantly influenced by atmospheric conditions. This underscores the importance of performing uncertainty quantification in determining the influence of system parameters on prediction of different quantities of interest.

Comparing the different probability density functions (PDFs) in Fig 6.14 for particle temperature T_p and the average burning rate $\dot{m}_t$ reveals a higher skewness value for the $\dot{m}t$ PDF compared to the T_p PDF. Furthermore, similar to PDFs in Figs 6.12 the PDFs for an oxy atmosphere exhibit higher skewness than those for an air atmosphere.



(a) Air atmosphere, particle temperature

(b) Oxy atmosphere, particle temperature

(c) Air atmosphere, burning rate

(d) Oxy atmosphere, burning rate

Fig. 6.14.: Evolution of uncertainties in particle temperature and burning rate with respect to system parameters: —, mean value (μ^0); red, standard deviation (σ).

6.3. Summary and Conclusions

This chapter concludes the development of different methods, including sensitivity analysis and uncertainty quantifications, and applies these methods to a complete model in single particle configurations. It has been found that the sensitivities of the particle burning rate and temperature are maximum in the first stage (before gas phase ignition) and tend to reach a plateau after ignition. This behavior is contrary to what was shown in Chapter 4, where only char combustion was considered.

Regarding sensitivities with respect to gas phase chemistry, it is found that the reaction $OH + H_2 = H + H_2O$ is independent of the atmosphere, highlighting the role of hydrogen in gas phase ignition. Moreover, the sensitivity

analyses show that oxygen concentration is the most important species, as its level of consumption in the gas phase determines the gas phase ignition characteristics. The high consumption of oxygen in the gas phase is also the reason for the ignition delay of the solid particle.

Finally, the uncertainty quantification shows that the uncertainty with respect to gas phase chemistry is nearly negligible, which demonstrates the robustness of the chemical kinetic model and mechanism. On the other hand, the uncertainties quantified for the particle parameters are more pronounced, especially when considering the particle burning rate. The most remarkable finding is that the evolution of the uncertainties increases with time, unlike the sensitivities, which decrease with time. As the uncertainty quantifications represent the global perspective, this could answer the actual question of the true influence of different parameter sensitivities on the objective function values, as shown in Figs 6.14 6.12.

As the burning rate shows large uncertainty propagation with respect to particle model parameters, it would be necessary for future studies to investigate the influence of burning the particle in multi-dimensional configurations, considering the different shapes of particles. Moreover, the effect of group combustion would significantly impact the burning rate for each particle in a cluster, indicating different behavior for the model uncertainties that need to be investigated. All of these important questions will be part of future studies in the Oxyflame project, of which this study is a part.

7

Concluding remarks

In this thesis, a framework for simulating solid fuel combustion and extracting the sensitivities of different quantities of interest (QoIs) with respect to various combustion model parameters is introduced. The aim is to study the performance, extract sensitivities, and quantify the uncertainties of different combustion models. Several configurations are analyzed, and the results are compared in different atmospheres (conventional air and oxy-fuel).

As a first step, both continuous and discrete adjoint are applied to char burnout for steady state configuration. Examining the resulting errors suggests discrete adjoint to be the most accurate formulation for gradient extraction, as far as steady char combustion is concerned. As the main interest lies in the configuration where a flame exists in the gas phase, the evolution of mass fractions and temperature is simulated in the presence of the flame to account for the gas-phase chemistry effect, and sensitivities of various local and spatially distributed QoIs with respect to multiple parameters are extracted and compared, using the discrete adjoint formulation. In addition, due to the importance of the oxy environment in coal combustion, the extracted sensitivities are compared for both air and oxy atmospheres. The comparison between the results for a single operating point shows that, regardless of the atmosphere, the system is highly sensitive to the parameters related to the surface reactions, which is expected, since the value of burning rate is directly dependent on the heterogeneous reactions. As the sensitivity of any QoI at a certain operating point does not give an indication about the global behaviour

of the gradients, in order to provide a global picture of the sensitivities in the system, sensitivity maps are extracted. Since local analysis shows high sensitivities with respect to the surface parameters, sensitivity maps are also extracted with respect to the parameters governing the surface reactions: surface temperature and the ratio between the surface Damköhler numbers γ. For the range of parameters chosen in chapter 2, the oxy environment shows two different characteristics: one dominated by the presence of the flame in the gas phase, and the other seen for low values of γ , where the flame in the gas-phase extinguishes, and all the dynamics, as well as the flame itself, reside on the surface of the particle, leading to a more dynamic picture in the sensitivity maps. This variation is more apparent in the sensitivities extracted for the total heat release rather than the burning rate. The two contributions to the heat release in char combustion are the heterogeneous and homogeneous reactions. In the presence of the flame, due to the higher enthalpy of the homogeneous reaction, the flame temperature dictates the value of heat release and its gradient. However, when the flame moves to the surface of the particle, only the heterogeneous reactions govern the value of heat released into the domain.

Due to the importance of the heterogenous reactions in these sonfigurations, a deeper investigation of the surface reaction kinetic models is carried out by introducing the single film model developed by Schiemann *et al.* in Chapter 3 for a steady-state configuration. The particular model of interest for this case is extracted through detailed measurement of Schiemann *et al.* [30], where model parameters are reported for various particle sizes, free stream compositions, and particle temperatures.

The variation of sensitivities are reported as the particle size, and free stream compositions are varied, as specified by the experimental measurements. The analysis shows the activation energy to be the most sensitive parameter, as far as, the burning rate and total heat release are concerned. The resulting parameter sensitivities vary slightly with particle diameter for burning rate as QoI. On the other hand, particle size shows a much higher impact in the extracted sensitivities when considering the total heat release. This is attributed to the fact that the total heat release is an integrated quantity, evaluated within the entire domain, whereas the burning rate is a local quantity determined mainly by the heterogeneous reaction rate on the surface of the particle. The analysis shows that the free stream composition has a large impact in the extracted sensitivities. Free stream conditions with higher oxygen concentrations, generally result in higher sensitivities in the model coefficients. Higher oxygen concentration leads to stronger reactions

on the surface, increasing the burning rate, leading to higher sensitivities in the model parameters as well.

It is important to note that when the surface temperature is set to a specific value based on the problem's boundary conditions, the impact of surface reactions is predetermined, which can affect the obtained sensitivities. To obtain a more comprehensive understanding, chapter 4 removes the surface temperature from the boundary conditions, resulting in a Robin-type boundary condition for temperature, and allows it to be solved as part of the problem. Additionally, the study investigates the impact of unsteadiness and non-linearity on the extracted sensitivities of char combustion models by analyzing an unsteady configuration.

In addition to the model parameters, another important factor in char combustion is the free stream composition. Due to success of oxy environments in reducing CO_2 emissions, air is commonly replaced by pure oxygen (O_2) or a mixture of oxygen with recycled flue gas, leading to variable free stream compositions. Therefore, the impact of free stream composition on the sensitivities need to be quantified as well. In chapter 4, using the adjoint method, sensitivities were extracted for variable quantities of interest in two free stream compositions corresponding to air and oxy environment. When the particle burning rate is considered as the QoI, the parameters of the first surface reaction (direct oxidation reaction) prove to be the most dominant, and in particular, the activation energy. This dominance remains independent of the selected time horizon (short or long) and the free stream composition. On the other hand, a shift of the QoI to particle temperature changes both the distribution of sensitivities at a selected time instance and their evolution in time. In the case of particle temperature, the pre-exponential factor seems to be the most sensitive parameter and its sensitivity steadily increases in time. This is due to the difference in the evolution of the particle temperature and the burning rate in time. However, regardless of the free stream composition, the burning rate shows higher sensitivities with respect to the model parameters, suggesting this quantity to be the most relevant in such sensitivity analyses. Burning rate sensitivities with respect to free stream variables show that the diluent species has the highest sensitivity, with the oxygen mass fraction following closely. However, the sensitivities with respect to free stream values are considerably lower than the sensitivities of heterogeneous model parameters, suggesting these models to be the main source of sensitivity in the system.

Chapter 5 provides a framework for investigating the uncertainties of chemical kinetic models in an isochoric adiabatic reactor configuration. The

uncertainties are extracted using active sub- space methodology (ASM) coupled with the adjoint method to minimize the cost of evaluating the necessary gradients. The results are also compared to the linear adjoint approximation method (LAAM), which provides a very quick estimation of the overall uncertainties. In a standard low-density case, where a single dominant direction can be selected, the uncertainties extracted using LAAM and ASM compare well with standard Monte Carlo. Although the accuracy of ASM is better than LAAM for this case, LAAM is able to provide a satisfactory result with a fraction of the cost. Different operating conditions, achieved by modifying the initial conditions, may lead to significant differences in the dispersion of the samples and the number of active dimensions. This is shown in a second case where a single active direction does not come out of the eigenmode expansion, motivating the use of a multi-dimensional subspace to construct the response surface. Despite the underlying locality and linearity assumptions, LAAM still gives a very good approximation for this case. This suggests that LAAM can be used as a preliminary estimation for UQ especially for large systems. Finally, the effect of strong nonlinearities on the overall uncertainties are considered. The results prove that the prediction of LAAM deteriorates in these conditions. However, this error can be reduced by using piecewise linear approximations by splitting the domain into smaller segments. This will be the subject of future research.

Chapter 6 concludes the study by summarizing various solid fuel combustion models, including char burnout, detailed gas phase kinetics, devolatilization, and others, applied in the simulation of unsteady axisymmetric particle. To identify the most sensitive parameters, a semi-discrete adjoint approach is used. The extracted sensitivities indicate that the particle size is the most dominant parameter regardless of the atmosphere (air/oxy) when considering the average particle temperature as the quantity of interest (QoI), consistent with the findings of [63]. However, when considering the average burning rate as the QoI, devolatilization parameters become more prominent due to the insignificant char combustion in the initial stage of devolatilization. Furthermore, analyzing the sensitivity of different quantities of interest concerning gas phase reaction rates reveals that volatile species are the most influential.

By analyzing the evolution of the sensitivities of the most dominant parameters over time, it is revealed that the maximum gradient occurs during the early heating phase of the particle. After that, the sensitivity values for most parameters stabilize until the onset of gas phase ignition, where the sensitivity trend changes. As the local gradient does not indicate the actual reaction path, active subspace method (ASM) is applied to evaluate global

sensitivities, as done in chapter 5. The Probability Density Function (PDF) of different quantities of interest regarding gas phase reaction rates agrees well with the Monte Carlo computed ones, with a cost reduction of up to three orders of magnitude.

Appendices

A

Adjoint derivation for boundary value problem

A.1. Derivation of the adjoint equation and gradient formula for two-point boundary value problem

The notation introduced in section 2.2 is used below. The derivation follows the original work of Servan & Petzold [49], with additional details for further clarity.

A.1.1. Forward sensitivity of the primal problem

Let the sensitivity of $\mathbf{u}(r)$ with respect to $\mathbf{p}$ be denoted as

$$\mathbf{u_p}(r) = \left.\frac{d\mathbf{u}}{d\mathbf{p}}\right|_r .$$

$\mathbf{u_p}$ is the solution of the linearized problem, referred to as the forward sensitivity problem

$$\frac{d\mathbf{u_p}}{dr} = \mathbf{F_u}\mathbf{u_p} + \mathbf{F_p},$$

subjected to the boundary conditions

$$\mathbf{A}\mathbf{u_p}(a) + \mathbf{B}\mathbf{u_p}(b) + \mathbf{h_p} = 0 \tag{A.1}$$

where $\mathbf{A}$ and $\mathbf{B}$ are defined in Eq. 2.22, $\mathbf{F_u}$ and $\mathbf{F_p}$ denote the jacobians of $\mathbf{F}$ with respect to $\mathbf{u}$ and $\mathbf{p}$, and $\mathbf{h_p}$ the jacobian of $\mathbf{h}$ with respect to $\mathbf{p}$.

A.1.2. Adjoint of the primal problem

This step focuses exclusively on the computation of the gradient of integral-form functionals (Eq. 2.24), which, is evaluated upon an integration over $[a, s]$. This suggests the use of two adjoint variables : $\boldsymbol{\lambda}_1^s$, the adjoint of the forward sensitivity equation over the interval $[a, s]$, and $\boldsymbol{\lambda}_2^s$ over $[s, b]$. The Lagrange procedure revolves around the addition of the following term to $dG^s/d\mathbf{p}$:

$$\int_a^s \boldsymbol{\lambda}_1^{s\,*}\left(\frac{d\mathbf{u_p}}{dt} - \mathbf{F_u}\mathbf{u_p} - \mathbf{F_p}\right)dr + \int_s^b \boldsymbol{\lambda}_2^{s\,*}\left(\frac{d\mathbf{u_p}}{dt} - \mathbf{F_u}\mathbf{u_p} - \mathbf{F_p}\right)dr = 0$$

where the $*$ subscript denotes the conjugate transpose. Integration by parts yields

$$\begin{aligned}&[\boldsymbol{\lambda}_1^{s\,*}\,\mathbf{u_p}]_a^s + [\boldsymbol{\lambda}_2^{s\,*}\,\mathbf{u_p}]_s^b - \int_a^s \boldsymbol{\lambda}_1^{s\,*}\,\mathbf{F_p}dr - \int_s^b \boldsymbol{\lambda}_2^{s\,*}\,\mathbf{F_p}dr \\ &- \int_a^s \mathbf{u_p^*}\left(\frac{d\boldsymbol{\lambda}_1^s}{dr} + \mathbf{F_u^*}\boldsymbol{\lambda}_1^s\right)dr - \int_s^b \mathbf{u_p^*}\left(\frac{d\boldsymbol{\lambda}_2^s}{dr} + \mathbf{F_u^*}\boldsymbol{\lambda}_2^s\right)dr = 0.\end{aligned} \tag{A.2}$$

Upon summation of Eqs. 2.24 and A.2, it emerges that provided the following three equations hold,

$$\begin{cases} -\dfrac{d\boldsymbol{\lambda}_1^s}{dr} = \mathbf{F}_{\mathbf{u}}^* \boldsymbol{\lambda}_1^s + g_{\mathbf{u}}^*, \\ -\dfrac{d\boldsymbol{\lambda}_2^s}{dr} = \mathbf{F}_{\mathbf{u}}^* \boldsymbol{\lambda}_2^s \end{cases} \tag{A.3}$$

and

$$\boldsymbol{\lambda}_1^s(s) - \boldsymbol{\lambda}_2^s(s) = 0, \tag{A.4}$$

the gradient of G^s is given by the following formula:

$$\begin{aligned} \frac{dG^s}{d\mathbf{p}} = &- \boldsymbol{\lambda}_2^{s\,*}(b)\,\mathbf{u}_{\mathbf{p}}(b) + \boldsymbol{\lambda}_1^{s\,*}(a)\,\mathbf{u}_{\mathbf{p}}(a) \\ &+ \int_a^s \left(g_{\mathbf{p}} + \boldsymbol{\lambda}_1^{s\,*}\,\mathbf{F}_{\mathbf{p}}\right) dr + \int_s^b \boldsymbol{\lambda}_2^{s\,*}\,\mathbf{F}_{\mathbf{p}} dr. \end{aligned} \tag{A.5}$$

If suitable boundary conditions relating $\boldsymbol{\lambda}_1^s(a)$ and $\boldsymbol{\lambda}_2^s(b)$ are provided, Eqs. A.3 and A.4 will form a multi-point boundary value problem for the adjoint variables $\boldsymbol{\lambda}_1^s$ and $\boldsymbol{\lambda}_2^s$. Given the linear dependence of the augmented objective function in the adjoint variables, it is legitimate to assume that the missing boundary conditions too are linear, that is there exist two square matrices $\overline{\mathbf{A}}$ and $\overline{\mathbf{B}}$ such that

$$\overline{\mathbf{A}}\boldsymbol{\lambda}_1^s(a) + \overline{\mathbf{B}}\boldsymbol{\lambda}_2^s(b) = 0 \tag{A.6}$$

and $\mathbf{P} = \left[\overline{\mathbf{A}}|\overline{\mathbf{B}}\right]$ has full rank. Note also that given the integral form of G^s, the conditions were also assumed homogeneous. Eq. A.6 states that the boundary conditions $\left(\boldsymbol{\lambda}_1^s(a), \boldsymbol{\lambda}_2^s(b)\right)$ belong to the null space of $\mathbf{P}$.

Since the adjoint methodology aims at avoiding computing forward sensitivities altogether, the aforementioned boundary condition should eliminate $\mathbf{u}_{\mathbf{p}}(a)$ and $\mathbf{u}_p(b)$ from Eq. A.5 by leveraging the forward sensitivity boundary condition (Eq. A.1). The key to elucidate the missing boundary conditions, and therefore construct $\overline{\mathbf{A}}$ and $\overline{\mathbf{B}}$, is the following theorem : given two m by $2m$ full-rank matrices $\mathbf{P}$ and $\mathbf{Q}$, then

$$\text{span}\left(\mathbf{P}^*\right) = \text{null}\left(\mathbf{Q}\right) \;\Leftrightarrow\; \text{span}\left(\mathbf{Q}^*\right) = \text{null}\left(\mathbf{P}\right).$$

In other words, posing $\mathbf{Q} = [-\mathbf{A}|\mathbf{B}]$, if $\mathbf{P}$ (and therefore, $\overline{\mathbf{A}}$ and $\overline{\mathbf{B}}$) is constructed such that its row space matches the null space of $\mathbf{Q}$, then since $\left(\boldsymbol{\lambda}_1^s(a), \boldsymbol{\lambda}_2^s(b)\right)$ belongs to the null space of $\mathbf{P}$, there exists $\boldsymbol{\alpha}$ such that

$$\begin{pmatrix} \boldsymbol{\lambda}_1^s(a) \\ \boldsymbol{\lambda}_2^s(b) \end{pmatrix} = \begin{bmatrix} -\mathbf{A}^* \\ \mathbf{B}^* \end{bmatrix} \boldsymbol{\alpha}.$$

As will be shortly seen, if the missing adjoint boundary conditions are be constructed such that

$$\text{span}\left(\left[\begin{array}{c}\overline{\mathbf{A}}^{*}\\ \overline{\mathbf{B}}^{*}\end{array}\right]\right)=\text{null}\left([-\mathbf{A}|\mathbf{B}]\right), \tag{A.7}$$

then substitution of Eq. A.1.2 in the first two terms of the right-hand side of Eq. A.5 yields

$$\boldsymbol{\lambda}_1^{s\,*}(a)\,\mathbf{u_p}(a)-\boldsymbol{\lambda}_2^{s\,*}(b)\,\mathbf{u_p}(b)=-\boldsymbol{\alpha}^{*}\left[\mathbf{A}\mathbf{u_p}(a)+\mathbf{B}\mathbf{u_p}(b)\right]$$

where the second factor in the right-hand side matches the first two terms in the sensitivity boundary condition equation A.1, which, can therefore be used to eliminate $\mathbf{u_p}(a)$ and $\mathbf{u_p}(b)$. One finally finds

$$\frac{dG^s}{d\mathbf{p}}=-\boldsymbol{\alpha}^{*}\mathbf{h_p}+\int_a^s\left(g_\mathbf{p}+\boldsymbol{\lambda}_1^{s\,*}\mathbf{F_p}\right)dr+\int_s^b\boldsymbol{\lambda}_2^{s\,*}\mathbf{F_p}dr$$

where

$$\boldsymbol{\alpha}=\left(\mathbf{A}\mathbf{A}^{*}+\mathbf{B}\mathbf{B}^{*}\right)^{-1}\left[\mathbf{B}\boldsymbol{\lambda}_2^{s}(b)-\mathbf{A}\boldsymbol{\lambda}_1^{s}(a)\right].$$

The matrices $\overline{\mathbf{A}}$ and $\overline{\mathbf{B}}$ derived for the combustion problem of interest are presented in A.2.

A.1.3. Forward sensitivity of the adjoint problem

Let $\boldsymbol{\mu}_i^s$ denote the forward sensitivity of $\boldsymbol{\lambda}_i^s$ with respect to s $(i=1,2)$.

$$\boldsymbol{\mu}_i^s=\frac{d\boldsymbol{\lambda}_i^s}{ds}.$$

From Eq. 2.23, I find

$$\left.\frac{dg}{d\mathbf{p}}\right|_s=-\boldsymbol{\beta}^{*}\mathbf{h_p}+g_\mathbf{p}(s)+\int_a^s\boldsymbol{\mu}_1^{s\,*}\mathbf{F_p}dr+\int_s^b\boldsymbol{\mu}_2^{s\,*}\mathbf{F_p}dr.$$

where $\boldsymbol{\lambda}_1^s(s)-\boldsymbol{\lambda}_2^s(s)$ was used,

$$\boldsymbol{\beta}=\left(\mathbf{A}\mathbf{A}^{*}+\mathbf{B}\mathbf{B}^{*}\right)^{-1}\left[\mathbf{B}\boldsymbol{\mu}_2^{s}(b)-\mathbf{A}\boldsymbol{\mu}_1^{s}(a)\right]$$

and $(\boldsymbol{\mu}_1^s,\boldsymbol{\mu}_2^s)$ is the solution of the following multi-point boundary value problem

$$\begin{cases}\dfrac{d\boldsymbol{\mu}_1^s}{dr}=\mathbf{F}_\mathbf{u}^{*}\boldsymbol{\mu}_1^s,\\ \dfrac{d\boldsymbol{\mu}_2^s}{dr}=\mathbf{F}_\mathbf{u}^{*}\boldsymbol{\mu}_2^s,\end{cases}$$

subject to

$$\begin{cases} \boldsymbol{\mu}_1^s(s) - \boldsymbol{\mu}_2^s(s) - g_{\mathbf{u}}^*(s) = 0, \\ \overline{\mathbf{A}}\boldsymbol{\mu}_1^s(a) + \overline{\mathbf{B}}\boldsymbol{\mu}_2^s(b) = 0. \end{cases}$$

The jump condition at $r = s$ in Eq. A.1.3 stems from the differentiation of Eq. A.4 with respect to s, which, results in

$$\boldsymbol{\mu}_1^s(s) + \left.\frac{d\boldsymbol{\lambda}_1^s}{dr}\right|_s - \boldsymbol{\mu}_2^s(s) - \left.\frac{d\boldsymbol{\lambda}_2^s}{dr}\right|_s = 0$$

that was further simplified using Eq. A.3.

A.1.4. Integration bounds

Two limit cases are of interest in the present study: $s \to b$ for integral quantities, and $s \to a$ for pointwise quantities. As highlighted below, the multi-point boundary value problems required for adjoint-based the gradient computations reduce to two-point boundary value problems.

Limit case $s = b$

In the limit $s \to b$, the adjoint problem reduces to

$$\begin{cases} -\dfrac{d\boldsymbol{\lambda}^b}{dr} = \mathbf{F}_{\mathbf{u}}^* \boldsymbol{\lambda}^b + g_{\mathbf{u}}^*, \\ \overline{\mathbf{A}}^* \boldsymbol{\lambda}^b(a) + \overline{\mathbf{B}}^* \boldsymbol{\lambda}^b(b) = 0, \end{cases}$$

and

$$\frac{dG^b}{d\mathbf{p}} = \left(\mathbf{A}\mathbf{A}^* + \mathbf{B}\mathbf{B}^*\right)^{-1} \left(\mathbf{B}\boldsymbol{\lambda}^b(b) - \mathbf{A}\boldsymbol{\lambda}^b(a)\right) \mathbf{h}_{\mathbf{p}} + \int_a^b \left(g_{\mathbf{p}} + \boldsymbol{\lambda}^{b\,*} \mathbf{F}_{\mathbf{p}}\right) dr.$$

Limit case $s = a$

In the limit $s \to a$, the forward sensitivity of the adjoint variable with respect to $s = a$ is the solution of

$$\begin{cases} -\dfrac{d\boldsymbol{\mu}^a}{dr} = \mathbf{F}_{\mathbf{u}}^* \boldsymbol{\mu}^a, \\ \overline{\mathbf{A}}\boldsymbol{\mu}^a(a) + \overline{\mathbf{B}}\boldsymbol{\mu}^a(b) + \overline{\mathbf{A}} g_{\mathbf{u}}^*(a) = 0. \end{cases}$$

The gradient of the pointwise quantity $g(a)$ is then

$$\begin{aligned}\left.\frac{dg}{d\mathbf{p}}\right|_a = &\left(\mathbf{A}\mathbf{A}^* + \mathbf{B}\mathbf{B}^*\right)^{-1}\left(\mathbf{B}\boldsymbol{\mu}^a(b) - \mathbf{A}\boldsymbol{\mu}^a(a)\right.\\ &\left. - \mathbf{A}g^*_{\mathbf{u}}(a) + g_{\mathbf{p}}(a) + \int_a^b \boldsymbol{\mu}^{a\,*}\,\mathbf{F}_{\mathbf{p}}dr.\right.\end{aligned} \tag{A.8}$$

A.2. Linearized boundary conditions

A.2.1. Forward problem

The jacobian matrices $\mathbf{A}$ and $\mathbf{B}$ of the boundary conditions, listed in the following order, are provided below. First, at the particle surface, species conservation (4 equations), temperature and saturation condition. Second, in the far field, composition (4 equations) and temperature.

$$\mathbf{A} = \begin{bmatrix}
\dot{M} & (\alpha-1)\,Da_1/\alpha & 2\,(\alpha-1)\,Da_2 & 0 & 0 & Y_{CO} & -1 & 0 & 0 & 0 & 0\\
0 & \dot{M}+Da_1 & 0 & 0 & 0 & Y_{O_2} & 0 & -1 & 0 & 0 & 0\\
0 & 0 & \dot{M}+Da_2 & 0 & 0 & Y_{CO_2} & 0 & 0 & -1 & 0 & 0\\
0 & 0 & 0 & \dot{M} & 0 & Y_{N_2} & 0 & 0 & 0 & -1 & 0\\
0 & 0 & 0 & 0 & 1 & 0 & 0 & 0 & 0 & 0 & 0\\
1 & 1 & 1 & 1 & 0 & 0 & 0 & 0 & 0 & 0 & 0\\
0 & 0 & 0 & 0 & 0 & 0 & 0 & 0 & 0 & 0 & 0\\
0 & 0 & 0 & 0 & 0 & 0 & 0 & 0 & 0 & 0 & 0\\
0 & 0 & 0 & 0 & 0 & 0 & 0 & 0 & 0 & 0 & 0\\
0 & 0 & 0 & 0 & 0 & 0 & 0 & 0 & 0 & 0 & 0\\
0 & 0 & 0 & 0 & 0 & 0 & 0 & 0 & 0 & 0 & 0
\end{bmatrix} \tag{A.9}$$

$$\mathbf{B} = \begin{bmatrix} 0 & 0 & 0 & 0 & 0 & 0 & 0 & 0 & 0 & 0 & 0 \\ 0 & 0 & 0 & 0 & 0 & 0 & 0 & 0 & 0 & 0 & 0 \\ 0 & 0 & 0 & 0 & 0 & 0 & 0 & 0 & 0 & 0 & 0 \\ 0 & 0 & 0 & 0 & 0 & 0 & 0 & 0 & 0 & 0 & 0 \\ 0 & 0 & 0 & 0 & 0 & 0 & 0 & 0 & 0 & 0 & 0 \\ 0 & 0 & 0 & 0 & 0 & 0 & 0 & 0 & 0 & 0 & 0 \\ 1 & 0 & 0 & 0 & 0 & 0 & 0 & 0 & 0 & 0 & 0 \\ 0 & 1 & 0 & 0 & 0 & 0 & 0 & 0 & 0 & 0 & 0 \\ 0 & 0 & 1 & 0 & 0 & 0 & 0 & 0 & 0 & 0 & 0 \\ 0 & 0 & 0 & 1 & 0 & 0 & 0 & 0 & 0 & 0 & 0 \\ 0 & 0 & 0 & 0 & 1 & 0 & 0 & 0 & 0 & 0 & 0 \end{bmatrix} \tag{A.10}$$

A.2.2. Adjoint problem

In order to express the boundary conditions of the adjoint problem, we define

$$\begin{aligned} Z =& Y_{CO}(a) + \frac{\alpha\dot{M} + (1-\alpha)\,Da_1^s}{\alpha\dot{M} + \alpha Da_1^s} Y_{O_2}(a) \\ &+ \frac{\dot{M} + 2(1-\alpha)\,Da_2^s}{\dot{M} + Da_2^s} Y_{CO_2}(a) + Y_{N_2}(a). \end{aligned} \tag{A.11}$$

The matrices $\overline{\mathbf{A}}$ and $\overline{\mathbf{B}}$ are constructed so as to satisfy Eq. A.7, that is a basis for the null space of $\mathbf{Q}$ is constructed and used to assemble $\overline{\mathbf{A}}$ and $\overline{\mathbf{B}}$. The choice of the basis is of course not unique, and the following matrices are but one example :

A. Adjoint derivation for boundary value problem

$$\overline{\mathbf{A}} = \begin{bmatrix}
\frac{Y_{O_2}}{\dot{M}+Da_1^s} + \frac{Y_{CO_2}}{\dot{M}+Da_2^s} + \frac{Y_{N_2}}{\dot{M}} & -\frac{Y_{O_2}}{\dot{M}+Da_1^s} & -\frac{Y_{CO_2}}{\dot{M}+Da_2^s} & -\frac{Y_{N_2}}{\dot{M}} & 0 & 1 & Z & 0 & 0 & 0 & 0 \\
\frac{Y_{O_2}-Z}{\dot{M}+Da_1^s} + \frac{Y_{CO_2}}{\dot{M}+Da_2^s} + \frac{Y_{N_2}}{\dot{M}} & \frac{Z-Y_{O_2}}{\dot{M}+Da_1^s} & -\frac{Y_{CO_2}}{\dot{M}+Da_2^s} & -\frac{Y_{N_2}}{\dot{M}} & 0 & 1 & 0 & Z & 0 & 0 & 0 \\
\frac{Y_{O_2}}{\dot{M}+Da_1^s} + \frac{Y_{CO_2}-Z}{\dot{M}+Da_2^s} + \frac{Y_{N_2}}{\dot{M}} & -\frac{Y_{O_2}}{\dot{M}+Da_1^s} & \frac{Z-Y_{CO_2}}{\dot{M}+Da_2^s} & -\frac{Y_{N_2}}{\dot{M}} & 0 & 1 & 0 & 0 & Z & 0 & 0 \\
\frac{Y_{O_2}}{\dot{M}+Da_1^s} + \frac{Y_{CO_2}}{\dot{M}+Da_2^s} + \frac{Y_{N_2}-Z}{\dot{M}} & -\frac{Y_{O_2}}{\dot{M}+Da_1^s} & -\frac{Y_{CO_2}}{\dot{M}+Da_2^s} & \frac{Z-Y_{N_2}}{\dot{M}} & 0 & 1 & 0 & 0 & 0 & Z & 0 \\
0 & 0 & 0 & 0 & 0 & 0 & 0 & 0 & 0 & 0 & 1 \\
0 & 0 & 0 & 0 & 0 & 0 & 0 & 0 & 0 & 0 & 0 \\
0 & 0 & 0 & 0 & 0 & 0 & 0 & 0 & 0 & 0 & 0 \\
0 & 0 & 0 & 0 & 0 & 0 & 0 & 0 & 0 & 0 & 0 \\
0 & 0 & 0 & 0 & 0 & 0 & 0 & 0 & 0 & 0 & 0 \\
0 & 0 & 0 & 0 & 0 & 0 & 0 & 0 & 0 & 0 & 0 \\
0 & 0 & 0 & 0 & 0 & 0 & 0 & 0 & 0 & 0 & 0
\end{bmatrix} \tag{.12}$$

and

$$\overline{\mathbf{B}} = \begin{bmatrix}
0 & 0 & 0 & 0 & 0 & 0 & 0 & 0 & 0 & 0 & 0 \\
0 & 0 & 0 & 0 & 0 & 0 & 0 & 0 & 0 & 0 & 0 \\
0 & 0 & 0 & 0 & 0 & 0 & 0 & 0 & 0 & 0 & 0 \\
0 & 0 & 0 & 0 & 0 & 0 & 0 & 0 & 0 & 0 & 0 \\
0 & 0 & 0 & 0 & 0 & 0 & 0 & 0 & 0 & 0 & 0 \\
0 & 0 & 0 & 0 & 0 & 1 & 0 & 0 & 0 & 0 & 0 \\
0 & 0 & 0 & 0 & 0 & 0 & 1 & 0 & 0 & 0 & 0 \\
0 & 0 & 0 & 0 & 0 & 0 & 0 & 1 & 0 & 0 & 0 \\
0 & 0 & 0 & 0 & 0 & 0 & 0 & 0 & 1 & 0 & 0 \\
0 & 0 & 0 & 0 & 0 & 0 & 0 & 0 & 0 & 1 & 0 \\
0 & 0 & 0 & 0 & 0 & 0 & 0 & 0 & 0 & 0 & 1
\end{bmatrix}. \tag{.13}$$

With this choice, the adjoint problem is therefore subjected to homogeneous boundary conditions of the following types :

- At $r = a$, four Robin conditions (one per adjoint species mass fraction) and one Neumann condition (for the adjoint temperature),
- At $r = b$, one Dirichlet condition (for the adjoint burning rate) and five Neumann conditions (one per adjoint species mass fraction, plus one for the adjoint temperature).

References

[1] W. E. O. . International Energy Agency. https://www.iea.org/reports/world-energy-outlook-2019/, 2019.

[2] J. Emmert, H. Schneider, C. Meißner, E. Sidiropoulos, J. I. Hölzer, T. Seeger, B. Böhm, A. Dreizler, and S. Wagner. Characterization of temperature distributions in a swirled oxy-fuel coal combustor using tomographic absorption spectroscopy with fluctuation modelling. *Applications in Energy and Combustion Science*, 6:100025, 2021.

[3] C. S.A. A. P. Farmand and H. Pitsch. Direct numerical simulation of solid fuel ignition and combustion in laminar and turbulent conditions. Oxyflame International Workshop, 2020.

[4] S. Farazi, M. Sadr, S. Kang, M. Schiemann, N. Vorobiev, V. Scherer, and H. Pitsch. Resolved simulations of single char particle combustion in a laminar flow field. *Fuel*, 201:15–28, 2017.

[5] J. Lee, A. Tomboulides, S. Orszag, R. Yetter, and F. Dryer. A transient two-dimensional chemically reactive flow model: fuel particle combustion in a nonquiescent environment. In *Symposium (international) on combustion*, volume 26, pages 3059–3065. Elsevier, 1996.

[6] S. Iavarone, J. Oreluk, S. T. Smith, A. Hegde, W. Li, A. Packard, M. Frenklach, P. J. Smith, F. Contino, and A. Parente. Application of bound-to-bound data collaboration approach for development and uncertainty quantification of a reduced char combustion model. *Fuel*, 232:769–779, 2018.

[7] H. Rabitz, M. Kramer, and D. Dacol. Sensitivity analysis in chemical kinetics. *Annual review of physical chemistry*, 34:419–461, 1983.

[8] A. Saltelli, M. Ratto, S. Tarantola, and F. Campolongo. Sensitivity analysis for chemical models. *Chemical reviews*, 105:2811–2828, 2005.

[9] L. Cai, Y. Uygun, C. Togbé, H. Pitsch, H. Olivier, P. Dagaut, and S. M. Sarathy. An experimental and modeling study of n-octanol combustion. *Proceedings of the Combustion Institute*, 35:419–427, 2015.

[10] M. B. Giles and N. A. Pierce. An introduction to the adjoint approach to design. *Flow, Turbulence and Combustion*, 65:393–415, 2000.

[11] A. Jameson. Aerodynamic shape optimization using the adjoint method. *Lectures at the Von Karman Institute, Brussels*, 2003.

[12] T. R. Bewley, P. Moin, and R. Temam. Dns-based predictive control of turbulence: an optimal benchmark for feedback algorithms. *Journal of Fluid Mechanics*, 447:179–225, 2001.

[13] M. Wei and J. B. Freund. A noise-controlled free shear flow. *Journal of Fluid Mechanics*, 546:123–152, 2006.

[14] O. Pironneau. On optimum design in fluid mechanics. *Journal of Fluid Mechanics*, 64:97–110, 1974.
[15] A. Jameson. Aerodynamic design via control theory. *Journal of Scientific Computing*, 3:233–260, 1988.
[16] A. Jameson, L. Martinelli, and N. A. Pierce. Optimum aerodynamic design using the navier–stokes equations. *Theoretical and Computational Fluid Dynamics*, 10:213–237, 1998.
[17] J. J. Reuther, A. Jameson, J. J. Alonso, M. J. Rimllnger, and D. Saunders. Constrained multipoint aerodynamic shape optimization using an adjoint formulation and parallel computers, part 2. *Journal of aircraft*, 36:61–74, 1999.
[18] M. P. Juniper. Triggering in the horizontal rijke tube: non-normality, transient growth and bypass transition. *Journal of Fluid Mechanics*, 667:272–308, 2011.
[19] M. Lemke, J. Reiss, and J. Sesterhenn. Adjoint-based analysis of thermoacoustic coupling. In *AIP Conference Proceedings*, volume 1558, pages 2163–2166. American Institute of Physics, 2013.
[20] S. Schmidt, C. Ilic, V. Schulz, and N. R. Gauger. Three-dimensional large-scale aerodynamic shape optimization based on shape calculus. *AIAA journal*, 51:2615–2627, 2013.
[21] S. Rabin, C. Caulfield, and R. Kerswell. Designing a more nonlinearly stable laminar flow via boundary manipulation. *Journal of Fluid Mechanics*, 738:R1, 2014.
[22] D. Foures, C. Caulfield, and P. Schmid. Optimal mixing in two-dimensional plane poiseuille flow at finite péclet number. *Journal of Fluid Mechanics*, 748:241–277, 2014.
[23] K. Duraisamy and J. Alonso. Adjoint based techniques for uncertainty quantification in turbulent flows with combustion. In *42nd AIAA Fluid Dynamics Conference and Exhibit*, page 2711, 2012.
[24] K. Braman, T. A. Oliver, and V. Raman. Adjoint-based sensitivity analysis of flames. *Combustion Theory and Modelling*, 19:29–56, 2015.
[25] M. Lemke, L. Cai, J. Reiss, H. Pitsch, and J. Sesterhenn. Adjoint-based sensitivity analysis of quantities of interest of complex combustion models. *Combustion Theory and Modelling*, 23:180–196, 2019.
[26] P. Sashittal, T. Sayadi, P. Schmid, I. Jang, and L. Magri. Adjoint-based sensitivity analysis for a reacting jet in crossflow. In *Proceedings of the Summer Program*, page 375, 2016.
[27] C. S. Skene and P. J. Schmid. Adjoint-based parametric sensitivity analysis for swirling m-flames. *Journal of Fluid Mechanics*, 859:516–542,

2019.

[28] J. Capecelatro, D. J. Bodony, and J. Freund. Adjoint-based sensitivity analysis of ignition in a turbulent reactive shear layer. In *55th AIAA Aerospace Sciences Meeting*, page 0846, 2017.

[29] M. Matalon. Complete burning and extinction of a carbon particle in an oxidizing atmosphere. *Combustion Science and Technology*, 24:115–127, 1980.

[30] M. Schiemann, M. Geier, C. R. Shaddix, N. Vorobiev, and V. Scherer. Determination of char combustion kinetics parameters: Comparison of point detector and imaging-based particle-sizing pyrometry. *Review of Scientific Instruments*, 85:075114, 2014.

[31] N. Safiran, J. Lotz, and U. Naumann. Algorithmic differentiation of numerical methods: Second-order adjoint solvers for parameterized systems of nonlinear equations. *Procedia Computer Science*, 80:2231–2235, 2016.

[32] M. Hantouche, S. M. Sarathy, and O. M. Knio. Global sensitivity analysis of n-butanol reaction kinetics using rate rules. *Combust. Flame*, 196:452–465, 2018.

[33] A. Doostan and H. Owhadi. A non-adapted sparse approximation of pdes with stochastic inputs. *J. Comput. Phys.*, 230:3015–3034, 2011.

[34] E. Savin, A. Resmini, and J. E. Peter. Sparse polynomial surrogates for aerodynamic computations with random inputs. *AIAA conference*, 18, 2016.

[35] C. E. Rasmussen and C. K. I. Williams. *Gaussian processes for machine learning.* Adaptive computation and machine learning. MIT Press, 2006.

[36] S. G. Davis, A. B. Mhadeshwar, D. G. Vlachos, and H. Wang. A new approach to response surface development for detailed gas-phase and surface reaction kinetic model optimization. *Int. J. Chem. Kinet.*, 36:94–106, 2004.

[37] A. S. Tomlin, E. Agbro, V. Nevrlý, J. Dlabka, and M. Vašinek. Evaluation of combustion mechanisms using global uncertainty and sensitivity analyses: a case study for low-temperature dimethylether oxidation. *Int. J. Chem. Kinet*, 46:662–682, 2014.

[38] S. Li, B. Yang, and F. Qi. Accelerate global sensitivity analysis using artificial neural network algorithm: Case studies for combustion kinetic model. *Combust. Flame*, 168:53–64, 2016.

[39] H. Wang and D. A. Sheen. Combustion kinetic model uncertainty quantification, propagation and minimization. *Progress in Energy and Combustion Science*, 47:1–31, 2015.

[40] P. G. Constantine, E. Dow, and Q. Wang. Active subspace methods in theory and practice: Applications to kriging surfaces. *SIAM J. Sci. Comput.*, 36(4):A1500–A1524, 2014.

[41] A. Saltelli, M. Ratto, T. Andres, F. Campolongo, J. Cariboni, D. Gatelli, M. Saisana, and S. Tarantola. Global sensitivity analysis: the primer. *Wiley-Interscience*, 2008.

[42] M. Eldred and J. Burkardt. Comparison of non-intrusive polynomial chaos and stochastic collocation methods for uncertainty quantification. *AIAA J.*, 2009:976, 2009.

[43] D. Xiu and J. S. Hesthaven. High-order collocation methods for differential equations with random inputs. *SIAM J. Sci. Comput.*, 27(3):1118–1139, 2005.

[44] W. Ji, Z. Ren, Y. Marzouk, and C. K. Law. Quantifying kinetic uncertainty in turbulent combustion simulations using active subspaces. *P. Combust. Inst.*, 37(2):2175–2182, 2019.

[45] W. Ji, J. Wang, O. Zahm, Y. M. Marzouk, B. Yang, Z. Ren, and C. K. Law. Shared low-dimensional subspaces for propagating kinetic uncertainty to multiple outputs. *Combust. Flame*, 190:146–157, 2018.

[46] X. Su, W. Ji, and Z. Ren. Uncertainty analysis in mechanism reduction via active subspace and transition state analyses. *Combust. Flame*, 227:135–146, 2021.

[47] T. S.V. L. C. H. P. Ahmed Hassan and A. Attili. Adjoint-based sensitivity analysis of steady char burnout. *Combustion Theory and Modelling*, 25:96–120, 2021.

[48] J. Howard, G. Williams, and D. Fine. Kinetics of carbon monoxide oxidation in postflame gases. *Symposium (International) on Combustion*, 14:975–986, 1973.

[49] R. Serban and L. R. Petzold. Efficient computation of sensitivities for ordinary differential equation boundary value problems. *SIAM journal on numerical analysis*, 40:220–232, 2002.

[50] M. MATALON. Weak burning and gas-phase ignition about a carbon particle in an oxidizing atmosphere. *Combustion Science and Technology*, 25:43–48, 1981.

[51] A. Makino. An approximate explicit expression for the combustion rate of a small carbon particle. *Combustion and Flame*, 90:143–154, 1992.

[52] M. H. Hekmat and M. Mirzaei. A comparison of the continuous and discrete adjoint approach extended based on the standard lattice boltzmann method in flow field inverse optimization problems. *Acta Mechanica*, 227:1025–1050, 2016.

[53] L. Chen, S. Z. Yong, and A. F. Ghoniem. Oxy-fuel combustion of pulverized coal: Characterization, fundamentals, stabilization and cfd modeling. *Progress in energy and combustion science*, 38:156–214, 2012.

[54] M. Schiemann, M. Geier, C. Shaddix, N. Vorobiev, and V. Scherer. Determination of char combustion kinetics parameters: Comparison of point detector and imaging-based particle-sizing pyrometry. *Rev. Sci. Instruments*, 85, 2014.

[55] L. Tognotti, J. Longwell, and A. Sarofim. The products of the high temperature oxidation of a single char particle in an electrodynamic balance. *Proc. Combust. Inst*, 24:1207–1213, 1991.

[56] N. Vorobiev, S. Valentiner, M. Schiemann, and V. Scherer. Comprehensive data set of single particle combustion under oxy-fuel conditions, part i: Measurement technique. *Combus. Sci. Tech.*, pages 1–22, 2020.

[57] A. Hassan, T. Sayadi, M. Schiemann, and V. Scherer. Adjoint-based sensitivity analysis of char combustion surface reaction kinetics. *Fuel*, 287:119–503, 2021.

[58] J. Murphy and C. Shaddix. Combustion kinetics of coal chars in oxygen-enriched environments. *Combust. Flame*, 144:710–729, 2006.

[59] P. Bejarano and Y. Levendis. Combustion of Coal Chars in Oxygen-Enriched Atmospheres. *Combust. Sci. Technol.*, 179:1569–1587, 2007.

[60] T. Holland and T. Fletcher. Comprehensive model of single particle pulverized coal combustion extended to oxy-coal conditions. *Energy Fuels*, 31:2722–2739, 2017.

[61] S. Niksa, G. Liu, and R. Hurt. Coal conversion submodels for design applications at elevated pressures. Part I. Devolatilization and char oxidation. *Prog. Energy Combust. Sci.*, 29:425–477, 2003.

[62] O. Senneca and P. Salatino. A semi-detailed kinetic model of char combustion with consideration of thermal annealing. *Proc. Combust. Inst.*, 33:1763–1770, 2011.

[63] C. Tirado, S. Jiménez, R. Johansson, and J. Ballester. Comparative study of four alternative models for CO oxidation around a burning coal char particles. *Combust. Flame*, 161:1085–1095, 2014.

[64] C. Tirado, S. Jiménez, and J. Ballester. Gasification of a pulverized sub-bituminous coal in CO2 at atmospheric pressure in an entrained flow reactor. *Combust. Flame*, 159:385–395, 2012.

[65] H. Zhang and A. Sandu. Fatode: A library for forward, adjoint, and tangent linear integration of odes. *SIAM J Sci. Comput.*, 36, 2014.

[66] Y. Cao, S. Li, L. Petzold, and R. Serban. Adjoint sensitivity analysis for differential-algebraic equations: the adjoint DAE system and its

numerical solution. *SIAM J. Sci. Comput*, 24:1076–1089, 2003.

[67] A. Hindmarsh, P. Brown, K. Grant, S. Lee, R. Serban, D. Shumaker, and C. Woodward. SUNDIALS: suite of nonlinear and differential/algebraic equation solvers. *ACM Transactions on Mathematical Software*, 31:363–396, 2005.

[68] J. B. A. Edelman and S. Karpinski. Julia: A fresh approach to numerical computing. *SIAM*, 59:65–98, 2020.

[69] F. Schäfer, M. Tarek, L. White, and C. Rackauckas. AbstractDifferentiation.jl: Backend-agnostic differentiable programming in julia, 2022.

[70] P. S.J. J. A. J.J Martins. The complex-step derivative approximation. *ACM Transactions on Mathematical Software*, 29:245, 2003.

[71] P. R. Conrad and Y. M. Marzouk. Adaptive smolyak pseudospectral approximations. *SIAM J. Sci. Comput*, 35:A2643–A2670, 2013.

[72] Q. Wang, K. Duraisamy, J. J. Alonso, and G. Iaccarino. Risk assessment of scramjet unstart using adjoint-based sampling methods. *AIAA J.*, 50:581–592, 2012.

[73] B. D. Phenix, J. L. Dinaro, M. A. Tatang, J. W. Tester, J. B. Howard, and G. J. McRae. Incorporation of parametric uncertainty into complex kinetic mechanisms: application to hydrogen oxidation in super-critical water. *Combust. Flame*, 112:132–146, 1998.

[74] A. A. Konnov. Remaining uncertainties in the kinetic mechanism of hydrogen combustion. *Combust. Flame*, 152:507–528, 2008.

[75] X. Du and K. Annamalai. The transient ignition of isolated coal particle. *combustion and Flame*, 97, 1994.

[76] P. Farmand, H. Nicolai, C. Schumann, A. Attili, L. Berger, T. Li, C. Geschwindner, F. di Mare, C. Hasse, B. Böhm, J. Janicka, and H. Pitsch. Numerical investigation and assessment of flamelet-based models for the prediction of pulverized solid fuel homogeneous ignition and combustion. *Combustion and Flame*, 235:111693, 2022.

[77] B. J. McBride, S. Gordon, and M. A. Reno. Coefficients for calculating thermodynamic and transport properties of individual species. *NASA Lewis Research Center*, 1993.

[78] D. Bradley, G. Dixon-Lewis, S. El-din Habik, and E. Mushi. The oxidation of graphite powder in flame reaction zones. *Symp. (Int.) Combust.*, 20:931–940, 1985.

[79] H. Kobayashi, J. B. Howard, and A. F. Sarofim. Coal devolatilization at high temperatures. *Symp. (Int.) Combust.*, 16:411–425, 1977.

[80] A. Hassan, T. Sayadi, V. Le Chenadec, and A. Attili. Sensitivity analysis of an unsteady char particle combustion. *Fuel*, 287:119–738, 2021.

[81] M. Schiemann, N. Vorobiev, and V. Scherer. Stereoscopic pyrometer for char combustion characterization. *Appl. Opt.*, 54:1097–108, 2015.

[82] A. Kazakov and M. Frenklach. Reduced reaction sets based on gri-mech 1.2 (drm22). *Available online: http://combustion.berkeley.edu/drm/*, 2018.